Thermal Behavior of Cuprous Oxide: A Comprehensive Study of Three-Body Phonon Effects and Beyond

Thesis by
Claire Nicole Saunders

In Partial Fulfillment of the Requirements for the
Degree of
Doctor of Philosophy

CALIFORNIA INSTITUTE OF TECHNOLOGY
Pasadena, California

2022
Defended May 19, 2022

To Dr. Stratos Christianakis,
Dr. Shijun (Cindy) Xi,
Dr. Ayman Saad,
and all the other healthcare professionals at Keck Medicine of the University of
Southern California, Verdugo Hills Hospital, and Huntington Memorial Hospital
who, amidst a pandemic, made this work possible.

ACKNOWLEDGEMENTS

I received funding from the Department of Energy (DOE) Office of Energy Science program Basic Energy Sciences (BES) throughout my graduate studies. I used computing resources from the National Energy Research Scientific Computing Center (NERSC), a DOE Office of Science User Facility. The neutron scattering data in this thesis was made possible by resources at the Spallation Neutron Source (SNS), yet another DOE Office of Science User Facility operated by the Oak Ridge National Laboratory (ORNL).

None of this work would have been possible without my advisor, Brent Fultz. He provided me with the tools and resources to become the scientist I am today. He never gave up on me, and I am so grateful for that. In addition to my advisor, I extend my gratitude to my thesis committee members: Keith Schwab, Austin Minnich, William Goddard, and Garrett Granroth.

I want to thank all the incredible mentors I had on this journey: Thomas Proffen, who introduced me to neutron scattering, Doug Abernathy and Garrett, who both spent countless hours helping me with experiments and post-processing data; Simonetta Frittelli, who was always willing to give career advice, and Anthony Fleury, who fostered my passion for science and showed me nothing is out of reach.

I would also like to acknowledge my colleagues and mentors at Caltech who made this work possible including: Hillary Smith, Jane Herriman, Dennis Kim, Fred Yang, Yang Shen, Olle Hellman, and all the current members of the Fultz group, with special thanks to Vladimir for his contributions to this work, and Camille Bernal-Choban and Stefan Lohaus for their incomparable editing skills.

I am incredibly grateful for all the love and support from my Caltech family: Camille, Stefan, Rebecca Gallivan, and Sydney Corona. I also want to thank my Pittsburgh family: Austin Pilz, Justin Chilleo, and Allison Domhoff.

None of this would have been possible without my family. I am deeply indebted to my Mom and Dad, Susan and Keith Saunders. I will never be able to repay the sacrifices they made for my education. This work is just as much theirs as it is mine. I would also like to thank them for giving me my best friends, Julia and Evan.

My Ph.D. was atypical. However, I'm not sure if a typical Ph.D. even exists. I got sick at the end of my first year of graduate school. My search for scientific answers at Caltech paralleled my journey to find a diagnosis and treatment. None of it was easy, and I would not have made it this far without a great support system and the care and effort of my physicians. Their passion for helping others enabled me to pursue my passions. For that reason, I dedicate this thesis to them.

I still don't have a diagnosis, and I can't say that I got my scientific answers either. But, if anything, I learned that being a good scientist and person is pursuing those answers despite the knowledge that you might never get them. So, at the end of this journey at Caltech, I can finally say that I am at peace with that.

ABSTRACT

Phonons, or quantized normal modes of crystal vibrations, are responsible for much of the thermophysical behavior in solid-state systems. This behavior includes properties like thermal expansion, defined as the change in material volume in response to temperature. Typically, materials expand upon heating and contract upon cooling; however, some undergo anomalous or negative thermal expansion (NTE). This study focuses on a material with NTE, cuprous oxide (Cu_2O), commonly known as cuprite. Using computational and experimental methods, we identify the underlying mechanisms of the NTE and how these mechanisms relate to temperature-dependent phonon behavior with temperature, using both computational and experimental methods.

Computationally, we interpret temperature-dependent changes in phonon energies with perturbation theory. Assuming that the bonds between atoms behave like simple harmonic oscillators, we model the observed random motion of the atoms around their equilibrium positions with quasi-harmonic (QH) and anharmonic (AH) approximations. Furthermore, the perturbations in the atom position allow us to model phonon energy changes in response to temperatures.

While these models, particularly AH models, have proven accurate in predicting the phonon behavior, experimental methods, like inelastic neutron scattering (INS), remain the gold standard for validation. This study presents INS data from single-crystal cuprite measured on the Wide-Angular Range Chopper Spectrometer (ARCS) at the Oak Ridge National Laboratory (ORNL) Spallation Neutron Source (SNS). We present INS data collected at 10 K, 300 K, 700 K, and 900 K. The post-processing workflow included: (1) binning with the software package Mantid, (2) reducing with a multiphonon background correction for polyatomic crystals, and (3) condensing into a single irreducible wedge in the first Brillouin zone (BZ). From this, we obtain a four-dimensional scattering function $S(\mathbf{Q}, E)$. Our AH calculations use the stochastic-Temperature Dependent Effective Potential (sTDEP) and the Machine Learning Interatomic Potential (MLIP) methods. The former method uses perturbation theory to include cubic and quartic AH contributions. The latter uses machine learning (ML), which in principle, includes all orders of AH terms.

This investigation of the NTE of cuprite demonstrates that QH and AH models successfully predict anomalous NTE behavior. However, only AH calculations show the temperature-dependent phonon behavior seen in INS results. This discrepancy likely stems from a fortuitous cancellation of cubic and quartic AH terms giving an apparent success of QH models for the NTE. Ultimately, a correct prediction of thermal expansion with incorrect phonons reinforces the need to look at the role of higher-order terms in the temperature-dependent behavior of this material.

Despite the success of sTDEP at predicting phonon frequency shifts, it could not account for the newly observed diffuse inelastic intensity (DII) in the INS phonon spectra. For this, MLIP was more effective.

This work provides complementary models to explain the origins of the DII, which is likely an emerging category of AH feature best described as a local nonlinear many-body process. We investigate phonon dissipation, the dynamics of systems coupled to their environments, Brownian motion, and discontinuities due to impulse transfer effects. We conclude by addressing the potential applications of the results and their role in future work on thermal lattice dynamics.

PUBLISHED CONTENT AND CONTRIBUTIONS

[1] C. N. Saunders, D. S. Kim, O. Hellman, H. L. Smith, N. J. Weadock, S. T. Omelchenko, G. E. Granroth, C. M. Bernal-Choban, S. H. Lohaus, D. L. Abernathy, and B. Fultz, Phys. Rev. B (in press),
C. N. S. performed the calculations, processed the experimental data, and wrote the manuscript.

[2] C. M. Bernal-Choban, H. Smith, C. N. Saunders, D. S. Kim, L. Mauger, D. L. Abernathy, and B. Fultz, "Nonharmonic contributions to the high-temperature phonon thermodynamics of Cr", Manuscript submitted for publication,
C. N. S. assisted with the calculations, wrote several scripts for experimental data processing, and discussed the manuscript.

[3] S. H. Lohaus, M. Heine, P. Guzman, C. Bernal-Choban, C. N. Saunders, G. Shen, E. E. Alp, O. Hellman, D. Broido, and B. Fultz, "Thermodynamic explanation of the Invar effect by experiment and computation", Manuscript submitted for publication,
C. N. S. assisted with experimental data analysis and discussed manuscript.

[4] C. N. Saunders, V. Ladygin, D. S. Kim, O. Hellman, H. L. Smith, N. J. Weadock, S. T. Omelchenko, G. E. Granroth, C. M. Bernal-Choban, S. H. Lohaus, D. L. Abernathy, and B. Fultz, "Diffuse impulse intensity in anharmonic materials", Manuscript in preparation,
C.N.S performed calculations, processed experimental data, and wrote the manuscript.

[5] H. L. Smith, C. N. Saunders, C. M. Bernal-Choban, L. K. Decker, D. L. Abernathy, J. Y. Y. Lin, M. D. Demetriou, and B. Fultz, "Vibrational contributions to the excess entropy in ultra-fragile metallic glasses", Manuscript in preparation,
C. N. S. participated in neutron data collection, wrote scripts for data post-processing, and discussed mansucript.

[6] P. Gehring, M. Helgeson, D. Louca, B. Olsen, K. A. Ross, N. Ross, C. Saunders, and Y. Xi, Neutron News **32**, `10.1080/10448632.2021.1875767` (2021),
C. N. S. attended and summarized a conference session for the manuscript.

[7] Y. Shen, C. N. Saunders, C. M. Bernal, D. L. Abernathy, T. J. Williams, M. E. Manley, and B. Fultz, Phys. Rev. B **103**, `10.1103/PhysRevB.103.134302` (2021),
C. N. S. participated in the neutron scattering experiment, wrote code for data post-processing, and commented on the manuscript.

[8] D. S. Kim, O. Hellman, N. Shulumba, C. N. Saunders, J. Y. Y. Lin, H. L. Smith, J. E. Herriman, J. L. Niedziela, D. L. Abernathy, C. W. Li, and B. Fultz, Phys. Rev. B **102**, 10.1103/PhysRevB.102.174311 (2020),
C. N. S. contributed code for for the neutron scattering data and assisted with writing the manuscript.

[9] S. H. Lohaus, M. B. Johnson, P. F. Ahnn, C. N. Saunders, H. L. Smith, M. A. White, and B. Fultz, Phys. Rev. Mater. **4**, 10.1103/PhysRevMaterials.4.086002 (2020),
C. N. S. provided the code and analyzed the neutron scattering data.

[10] Y. Shen, C. N. Saunders, C. M. Bernal, D. L. Abernathy, M. E. Manley, and B. Fultz, Phys. Rev. Lett. **125**, 10.1103/PhysRevLett.125.085504 (2020),
C. N. S. participated in the neutron scattering experiment, wrote code for data post-processing, and commented on manuscript.

[11] F. C. Yang, O. Hellman, M. S. Lucas, H. L. Smith, C. N. Saunders, Y. Xiao, P. Chow, and B. Fultz, Phys. Rev. B **98**, 10.1103/PhysRevB.98.024301 (2018),
C. N. S. participated in the experiment, assisted in data analysis, and commented on the manuscript.

TABLE OF CONTENTS

LIST OF ILLUSTRATIONS

Number *Page*

LIST OF TABLES

NOMENCLATURE

AH. Anharmonic.

AIMD. *Ab Initio* Molecular Dynamics.

ARCS. Wide-Angular Range Chopper Spectrometer.

BES. Basic Energy Sciences.

BZ. Brillouin zone.

Cu$_2$O. Cuprous Oxide (Cuprite).

DFT. Density Functional Theory.

DII. Diffuse Inelastic Intensity.

DOE. Department of Energy.

HPC. High-performance Computing.

ILM. Intrinsic Localized Mode.

INS. Inelastic Neutron Scattering.

IPS. Intermodulation Phonon Sideband.

LAMMPS. Large-scale Atomic/Molecular Massively Parallel Simulator.

MD. Molecular Dynamics.

ML. Machine learning.

MLIP. Machine Learning Interatomic Potential.

MTP. Moment Tensor Potential.

NERSC. National Energy Research Scientific Computing Center.

NTE. Negative thermal expansion.

ORNL. Oak Ridge National Laboratory.

QH. Quasi-harmonic.

SNS. Spallation Neutron Source.

sTDEP. stochastic Temperature Dependent Effective Potential.

VASP. Vienna *Ab initio* Simulation Package.

Chapter 1

INTRODUCTION

I did not understand what materials science was until college. The small high school I attended nestled in the uppermost corner of Pennsylvania Appalachia had the basics. Materials science was considered fancy. However, it was an area rich in materials. My fourth-grade class field trip took us underground into the anthracite coal mines, where many of our great grandparents spent their days. By the time I came around, the mines were closed, some consumed by floodwaters. Others were structurally unstable after years of unsustainable mining practices. A shift to cleaner energy sources like a steam nuclear power plant built along the same river that witnessed the Three Mile Island Disaster made the mines obsolete.

No matter where you are, materials are everywhere. And unless you live inside a vacuum, you see the dynamic properties of these materials. This work focuses on some of these fundamental properties and behavior, specifically the role of temperature.

This thesis looks at the material cuprous oxide, commonly called cuprite. Cuprite is a mineral that consists of the elements copper (Cu) and oxygen (O) in a 2:1 ratio in a cubic arrangement. It has interesting temperature-dependent behavior, particularly the thermal expansion behavior. Unlike most materials, cuprite contracts with an increase in temperature for a limited temperature range. This goes against our intuition that materials expand upon heating, a property known as thermal expansion.

Whether you realize it or not, we all have experience with thermal expansion. For example, imagine you want to open a glass jar with a metal lid, but it will not budge. One trick is to run the top of the jar under hot water. The heat causes the metal lid to expand, making it easier to open. But what happens if we run the entire jar under the hot water? The answer is that the jar and lid increase in volume at different rates. This difference in the increase in volume is because they have different coefficients of thermal expansion. Since the metal has a larger coefficient of thermal expansion, it undergoes a more substantial change in volume in response to the change in temperature. At the end of the day, heat and the resulting thermal expansion help you open the jar.

The primary experimental method in this thesis is neutron scattering. Neutron scattering fires neutrons at a material of interest and measures how those neutrons interact with it. The nature of these interactions provides us with valuable information about the structure and dynamics of materials. Throughout my thesis, I've participated in many neutron scattering experiments. We collect data for these experiments at government-funded user facilities with specialized instruments. We then compare the data from these experiments with calculations.

The theoretical portion of this thesis is computational thermodynamics which is part of a larger field in materials science called computational materials. In computational materials, the goal is to use computer code and theory to describe the behavior of atoms in a chemical system. For example, suppose we know the atom position and velocity in a solid. In that case, we can use this information to determine properties like stability. The field of computational materials continues to grow with advances in computing on high-performance computers (HPC), also known as supercomputers. I performed all the calculations shown in this work on HPC.

Chapter 1 of the work provides much of the background information needed to understand the techniques and methods used throughout. Chapter 2 focuses on thermal expansion in cuprite. Using computation and experiment, we try to figure out the underlying mechanisms in cuprite that explain how this material changes in volume in response to temperature. We also look at problems with the theory used to understand temperature-dependent behavior. Finally, we tackle the question of model fidelity, or how well a model reproduces the actual behavior of the real world. Chapter 3 addresses a new feature in our neutron scattering data through existing theories and calculations. Last but not least, Chapter 4 talks about the future. Here we outline future experiments and ideas to explore the new phenomenon in this work.

Chapter 2

BACKGROUND

The *phonon* is the elementary unit of vibration in atoms or molecules, much like the photon is the elementary unit of electromagnetic radiation or light. The word phonon comes from the Greek word phonē — sound or voice. A thorough comprehension of phonon behavior in a material is imperative to understanding the bulk thermophysical properties and attributes.

We classify phonons as longitudinal or transverse depending on the direction of their motion relative to their wave propagation. In longitudinal phonons, the atoms vibrate parallel to the direction of the wave propagation, whereas, in transverse phonons, the atoms vibrate perpendicular to the direction of wave propagation.

Another classification of phonons is acoustic or optic. Acoustic phonons have lower frequencies that correspond to long-wavelength vibrations. These phonons typically vibrate in phase with their neighbors. Optical phonons are found at higher energies and oscillate out of phase with their neighbors.

To gather information on all phonons in a material, we rely on experiments, theories, and computations. Alone, each methods may not provide sufficient information to fully describe the microscopic phonon behavior. However, when used in conjunction, they provide ample details to assemble a model.

2.1 The Fundamentals of Neutron Scattering

In the past ten years, we have seen orders of magnitude improvement in computation and theory. However, experiments remain the gold standard for understanding phonon behavior. Experimentally, one of the best ways to examine phonons in a material is through coherent inelastic neutron scattering (INS). Scattering experiments involve observing and measuring the deviation in motion of an incoming particle upon impact with material or medium. In inelastic scattering, neutron energy is not conserved, meaning the final energy of the neutron is different from its initial, as shown in Fig. 2.1, leaving us with $\mathbf{Q} = \mathbf{k_i} - \mathbf{k_f}$. This definition of $\mathbf{Q}$ in terms of $\mathbf{k_i}$ and $\mathbf{k_f}$ is standard practice in diffraction and other scattering sciences. Therefore, we refer to $\mathbf{Q}$ as a scattering vector and $\hbar\mathbf{Q}$ as the momentum transfer, which comes from the well-known Planck relation. The Planck relation tells us

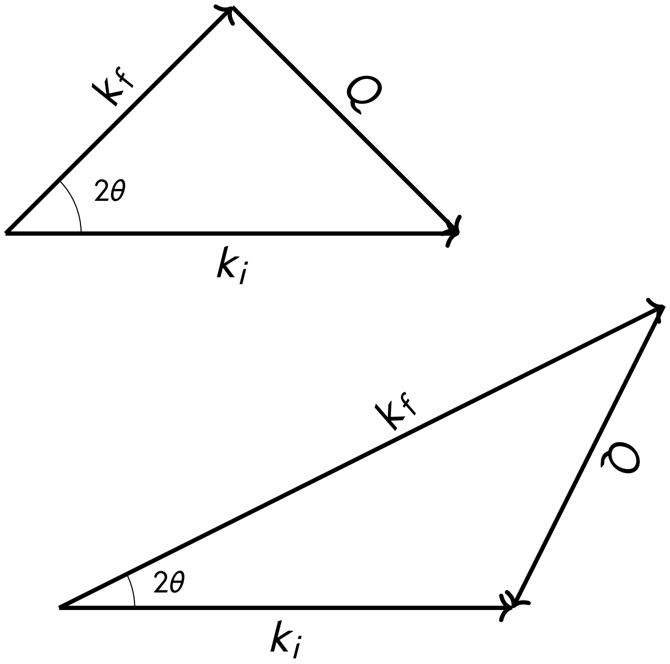

Figure 2.1: A diagram showing the energy transfer in INS for an incoming neutron with energy $\hbar\mathbf{k_i}$, where $\hbar$ is the reduced Planck constant $(6.5821 \times 10^{-16} eV \cdot s)$ and k_i is the incoming neutron wavevector, colliding with a sample resulting in an outgoing wavevector, $\mathbf{k_f}$. The vectors on the top show the scenario where the neutron loses energy from the collision and the lower image shows the scenario where the neutron gains energy. To conserve energy and momentum in the system, this collision results in a momentum transfer, $\hbar\mathbf{Q}$, which can be the energy of a phonon.

that the energy of a phonon is proportional to its frequency and, consequently, its wavevector. The variables $\mathbf{k_i}$ and $\mathbf{k_f}$ are the initial and final scattering wave vectors of the neutron shown in Fig. 2.2, whereas, Fig. 2.1 shows the vector relationship between them. The use of $\mathbf{Q}$ and $\mathbf{k_{i/f}}$ allows us to specify the components of the system. For example, we use $\mathbf{Q}$ to talk about the dynamics of the nucleus and $\mathbf{k}$ to talk about the neutron. Later on in this work, we will use $\vec{q}$ to refer to a spatial point in reciprocal space in a crystal sample, and it is distinct from the variables $\mathbf{Q}$ and $\mathbf{k}$. We use thermal neutrons to study the dynamics or vibrations in materials. Thermal neutrons have energy on the order of $k_B T$, Boltzmann's constant ($8.617x10^{-5}$ eV/K) multiplied by the temperature, and an average wavelength of 1.8 Å. This energy and wavelength are in the same order of magnitude as the interatomic spacing in most materials. For these reasons, they are ideal for probing collective excitation, like phonons. Further, neutrons are suitable for

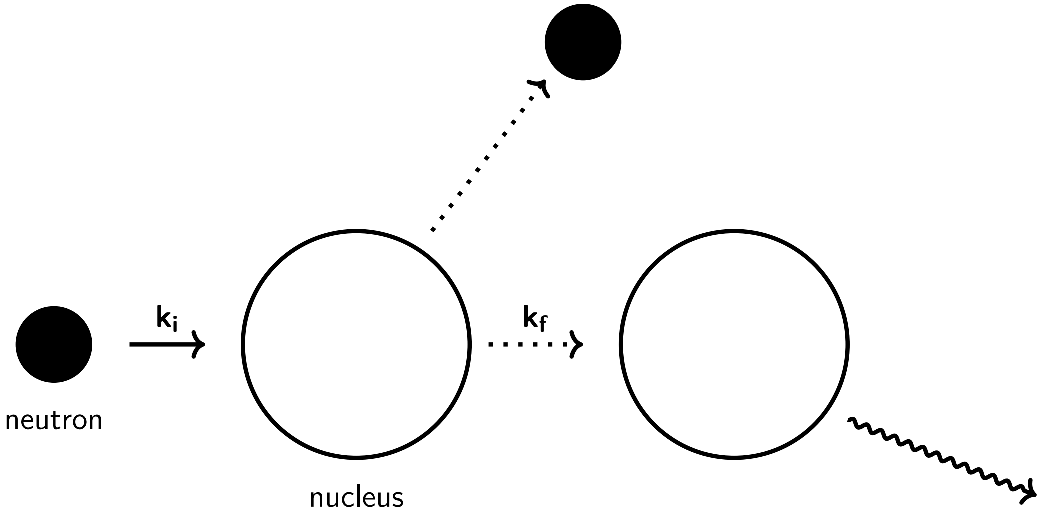

Figure 2.2: A pictorial representation of inelastic neutron scattering. The incoming neutron (black circle) strikes the atomic nucleus (large white circle with black outline) and rebounds. The nucleus undergoes a change in energy from the neutron impact, denoted by the squiggle line.

measuring phonons because they have zero net charge, allowing them to interact with atomic nuclei rather than an atom's electron shell.

We classify the type of scattering based on coherent versus incoherent and elastic versus inelastic characteristics. Coherent scattering preserves the phase of the scattered neutrons. A more intuitive way to think of coherence is to think of constructive and destructive interference in sound waves. For example, imagine attending a concert. Depending on the seat or location in the venue, the music will sound different. A specific section of the concert venue might be louder due to the constructive interference of the sound waves. With this in mind, when two sound waves are "in phase" with one another, their amplitudes add together, resulting in a louder sound. Two waves out of phase have the opposite effect and cancel one another out. Regarding neutrons, for a coherent scattering process, we know the incoming and outgoing phase of the neutron or wave, whereas, for incoherent scattering, this relationship is unknown. This unknown relationship can be due to a coupling of the oscillators in the system.

Each combination of scattering: incoherent elastic, incoherent inelastic, coherent elastic, and incoherent inelastic provides different information about material dynamics [1]. Figure 2.3 summarizes this information and lists general behavior for the total scattering function, S, which is the sum of the component from the neutrons scattering off the sample along with phonon-phonon interactions, and the

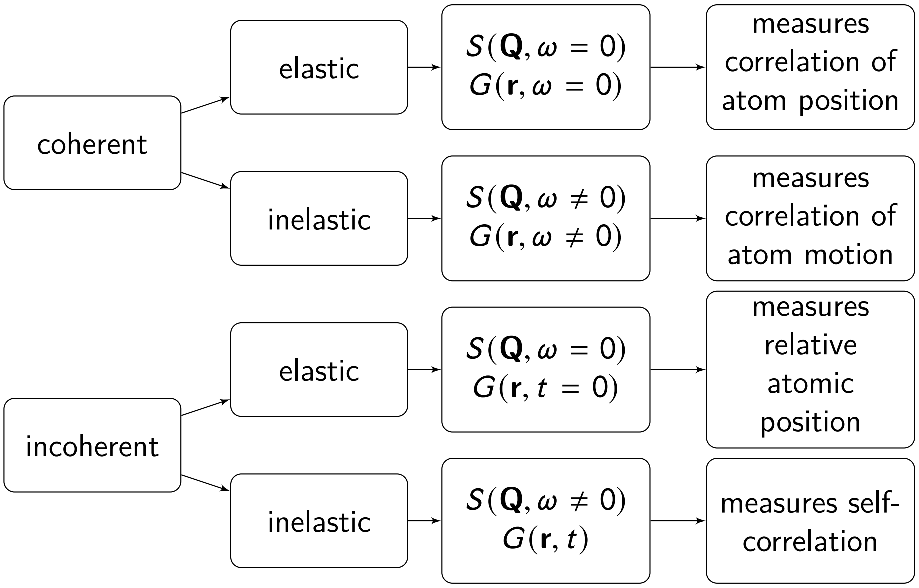

Figure 2.3: A flow chart showing the types of neutron scattering along with the total scattering factor, S, the pair distribution function, G, and what each type measures.

pair distribution function, G, the probability of finding an element in the sample at a given radial distance. This figure also describes the type of phenomenon each type of scattering examines.

INS experiments typically require expensive, high-precision instrumentation and power sources. Consequently, we usually perform these experiments at centralized government user facilities. At the time of publication, the largest neutron facility in North America was the Spallation Neutron Source (SNS), located at Oak Ridge National Laboratory (ORNL) in Oak Ridge, Tennessee, USA [2].

The SNS houses many instruments, each designed for different types of scattering experiments, sample environments, and various energy ranges. While there are several instruments at the SNS capable of studying phonons, the premiere instrument is the Wide Angular-Range Chopper Spectrometer (ARCS) [3]. ARCS achieves unique energy and spatial resolution optimization, ideal for studying high-energy phonons in materials. ARCS uses Fermi choppers, which regulate the opening of a pathway for the neutrons with a specific velocity to pass through. This results in a monochromatic pulse of neutrons at the desired specifications [4]. In contrast to triple-axis neutron scattering measurements, INS measurements with ARCS are not limited to individual energy scans at a single point in a sample.

We record individual neutron “events“ during INS experiments. This type of data collection is called event-based data collection. In this setup, we find the wavelength or energy of each neutron from its velocity. ARCS measures momentum transfer from neutron events with a two-dimensional detector bank array spanning -30°to +60°. Detectors like these record each neutron event by the pixel and time the detector registers the neutron, as shown in Fig. 2.4. Finally, we bin the neutron into a histogram and convert it to the spatial reference frame of the sample.

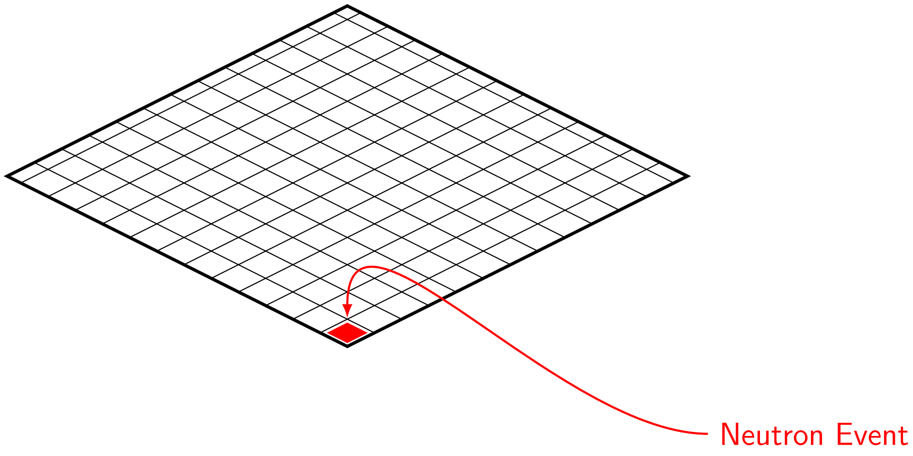

Figure 2.4: A pictorial representation of a detector with pixels recording neutron events. The red shaded pixel records the neutron event. The distance from the sample to the detector is known to be L. With this information, we can indirectly obtain a value for **Q**. This form of data collection histograms the data.

We can study several high-to-low periodic samples including: single crystals, polycrystals, and powders. The focus of this study is single-crystal measurements. A single crystal or monocrystalline sample is a solid material with a continuous and unbroken crystal lattice, much like toy blocks arranged in a repeating orientation. A perfect single crystal does not have grain boundaries or defects. Polycrystals consist of smaller subsets of single crystals, called crystallites or grains. Grain boundaries separate the crystallites or grains. As the name suggests, powder samples are small particulates of a chemical species or compound. While one can transform a single crystal or polycrystal into a powder by grinding up a single crystal or polycrystal, the reverse is not so simple. As a result, growing single crystals remain cost and time prohibitive.

Each sample type helps look at different components of phonon behavior. For example, with powder and crystallite, we obtain a phonon density of state (DOS), as shown in Fig. 2.5. The phonon DOS contains information about the phonon states in a material, typically displayed as a function of frequency or energy. The

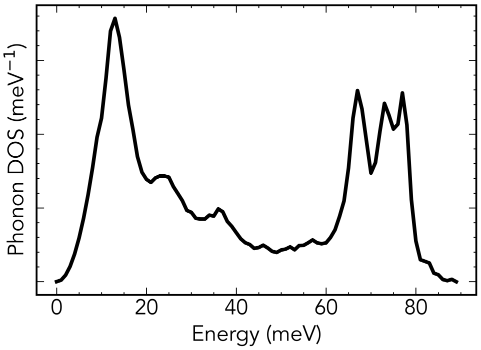

Figure 2.5: An example phonon DOS measured with INS.

phonon DOS is incredibly useful for examining phonon occupancy changes with temperature. We see that phonons occupy the higher energy or frequency modes for virtually all materials at high temperatures.

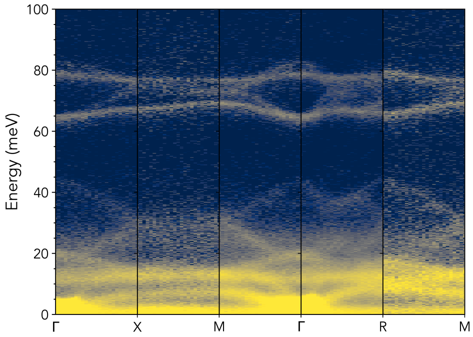

Figure 2.6: An example of phonon dispersions measured with INS.

With single crystals, we obtain complete phonon dispersions like the one shown in Fig. 2.6. A phonon dispersion provides the spatial/directional dependence of the phonon frequencies in a crystal typically viewed along the path of the high-symmetry directions in reciprocal space. Reciprocal space is the Fourier transform of real space. Real-space is what we know as Cartesian coordinates, whereas reciprocal space serves as a tool to work with frequency in the crystal lattice with ease. The Fourier transform provides a spatial variable that relates directly to a frequency, which is incredibly convenient for phonon frequencies. When referring to points in reciprocal space, we use the variable $\vec{q}$. A significant difference between phonon DOS and dispersions is that we visualize the latter with an explicit $\vec{q}$-dependence as shown in Fig 2.6 where the x-axis shows the $\vec{q}$-dependence with the high-symmetry points. The high symmetry points in reciprocal space are particular points that are invariant under certain transformations. It allows one to look at a smaller subset of the crystal while maximizing the amount of information obtained. Examples of high symmetry points in cuprite, a cubic structure, are shown in Table 2.1. To relate high-symmetry points to a concept we see in our everyday lives, we can think of them in terms of navigation. The high-symmetry points are like specific landmarks on an extended road trip. By seeing specific landmarks, we can get the vibe of a specific region.

Symbol	**Symmetry Points**	**Description**
Γ	$(0, 0, 0)$	center of BZ
X	$\left(0, \frac{1}{2}, 0\right)$	center of face
M	$\left(\frac{1}{2}, \frac{1}{2}, 0\right)$	center of edge
R	$\left(\frac{1}{2}, \frac{1}{2}, \frac{1}{2}\right)$	corner

Table 2.1: This table shows the high-symmetry points for the cuprite structure and describes where they are located on the unit cell lattice.

2.2 Computational Thermodynamics

Calculations complement experimental measurements of phonons. There exist a variety of software packages available to model phonons. For this work, we focus on perturbation theory calculations with effective potentials like the stochastic-Temperature Effective Potential (sTDEP) method and machine learning interatomic potentials (MLIP) with moment tensor potentials (MTP).

Perturbation theory is an approximation technique that relies on small variations from a ground state solution like the harmonic Hamiltonian, $\hat{H}_H$. We can write this as:

$$\hat{H} = \hat{H}_H + \lambda^3 \hat{H}_3 + \lambda^4 \hat{H}_4 + \lambda^5 \hat{H}_5 + \dots \tag{2.1}$$

where the harmonic Hamiltonian, an energy operator that contains all the potential and kinetic energy for the ground or base state, is:

$$\hat{H}_H = U_0 + \sum_i \frac{\mathbf{p}_i^2}{2m} + \frac{1}{2} \sum_{ij\alpha\beta} \Phi_{ij}^{\alpha\beta} u_i^\alpha u_j^\beta . \tag{2.2}$$

In the harmonic Hamiltonian, we ignore all terms above the second order. The harmonic approximation has the advantage of being the most computationally feasible. However, the omission of high-order terms results in a model that fails to predict fundamental thermal properties like thermal expansion, defined as the volume change in response to temperature.

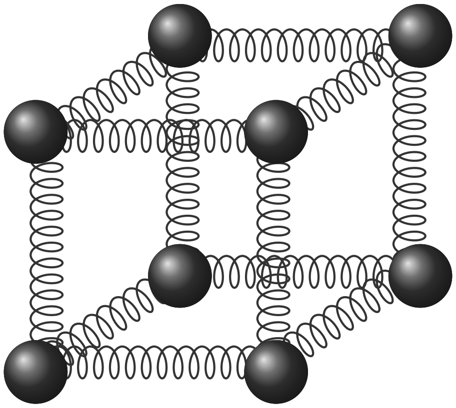

Figure 2.7: A drawing of a cubic crystal structure with atomic interactions shown as springs.

We need a more complex model like the quasiharmonic (QH) approximation to account for properties like thermal expansion. The QH model does not explicitly depend on temperature. The harmonic and QH Hamiltonians are the same. The difference is that the QH model accounts for thermal expansion through a renormalization of the Hamiltonian at each volume. While the QH approximation can obtain accurate values, it lacks fidelity. We know that temperature changes directly affect the crystal lattice volume. Therefore, we ought to use an explicit temperature dependence model. The anharmonic approximation (AH) contains the desired temperature dependence. It also includes higher-order perturbative terms, as shown in the equation:

$$\begin{aligned}\hat{H}_{AH} = U_0 + \sum_i \frac{\mathbf{p}_i^2}{2m} + \frac{1}{2}\sum_{ij\alpha\beta} \Phi_{ij}^{\alpha\beta} u_i^\alpha u_j^\beta \\ + \frac{1}{3!}\sum_{ijk\alpha\beta\gamma} \Phi_{ijk}^{\alpha\beta\gamma} u_i^\alpha u_j^\beta u_k^\gamma + \frac{1}{4!}\sum_{ijkl\alpha\beta\gamma\delta} \Phi_{ijkl}^{\alpha\beta\gamma\delta} u_i^\alpha u_j^\beta u_k^\gamma u_l^\delta .\end{aligned} \tag{2.3}$$

In the above equation, $\mathbf{p}$ is the momentum; m is the mass; u_i, u_j, u_k, u_l are atomic displacements; and Φ is the interatomic force constant corresponding to the one, two, three, and four phonon processes. The higher-order AH terms better describe the underlying physics; however, it comes at a much higher computational cost than the harmonic and QH approximations. Figure 2.7 shows a cubic crystal lattice with springs as bonds.

The unifying concept is the free energy, F, regardless of the computational method. At finite temperatures, we can write an expression for F as a sum of individual contributions:

$$F = U_{el} - TS_{vib}. \tag{2.4}$$

In this equation, U_{el} is the elastic energy of the system; T is the temperature; and S_{vib} is the vibrational energy. This equation is defined under constant volume, V, whereas the Gibbs free energy, G, is defined under constant pressure, P,

$$G = F + PV = U_{el} - TS_{vib} + PV. \tag{2.5}$$

To understand the origin of these components, we can look at the various approximations we employ. The Born-Oppenheimer approximation states that the wavefunctions or mathematical expressions that describe the state of a system, from atomic nuclei (comprised of neutrons and protons) and electrons are separable since there is a substantial difference in mass and subsequently timescales between these two entities. Consequentially, we can express the Hamiltonian in the Born-Oppenheimer approximation as

$$\hat{H} = \hat{H}_n + \hat{H}_e \tag{2.6}$$

where $\hat{H}_e$ is the Hamiltonian for the electrons and $\hat{H}_n$ is the Hamiltonian for the nucleus. The majority of the mass of an atom is from the nucleus. Therefore, we focus on $\hat{H}_n$.

We can obtain an expression for the system's free energy from the Hamiltonian. One way of doing this is with a canonical ensemble. In this statistical setup, the atoms or components of a system interact with a heat reservoir or bath at a set temperature. In a canonical approach, the probability, $\hat{P}$, of finding system A in the state α with corresponding energy E_α while in equilibrium with the thermal bath is:

$$\mathcal{P}_\alpha = \frac{e^{-E_\alpha/k_B T}}{\sum_\alpha e^{-E_\alpha/k_B T}}. \tag{2.7}$$

The factor $k_B T$ provides an explicit temperature dependence in the above equation. Looking at a specific case where the trace of the density matrix equals one, we replace E_α with $\hat{H}_\alpha$.

From these expressions, we turn to the basic thermodynamic definitions and equations. The vibrational entropy, S_{vib}, is the measurable disorder of a given system from the vibrations of the atoms about their ideal positions. Another way to think about vibrational entropy in lattice dynamics is the phase space that the atoms can traverse or explore. We show a visualization of this phase space in Fig. 2.8.

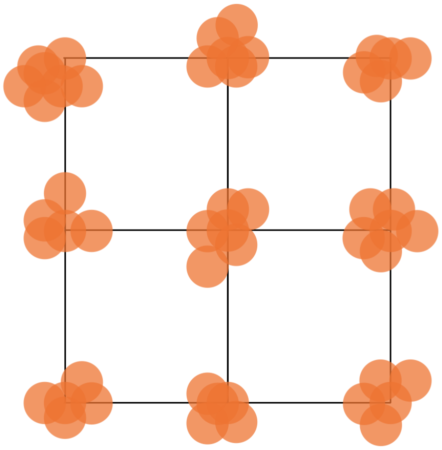

Figure 2.8: A visualization of phase space with overlaid snapshots of atomic displacements. The region around the atomic equilibrium position is analogous to the phase space.

An expression for the Gibbs entropy, named after its discoverer Josiah Willard Gibbs, is

$$S_{vib} = k_B \sum_i \mathcal{P}_\alpha \ln \mathcal{P}_\alpha . \tag{2.8}$$

Phonon behavior described with a canonical ensemble is often written using the Planck occupancy factor, which provides information on the number of phonons in the system. Looking at the case of a single phonon mode with energy and corresponding frequency, $\varepsilon_1 = \hbar\omega_1$, we can write an expression for the partition function

$$Z = \sum_n e^{-n\varepsilon_n/k_B T} \tag{2.9}$$

which for n=1 is

$$Z = 1 + e^{-\varepsilon_1/k_B T} = 1 + e^{-\hbar\omega_1/k_B T} . \tag{2.10}$$

The above expression is the partition function for the one-phonon case. To obtain the probability for the one-phonon occupancy, we follow the same procedure as we did for Eq. 2.7.

$$\mathcal{P} = \frac{e^{-\hbar\omega_1/k_B T}}{\sum_0^\alpha e^{-\hbar\omega_\alpha/k_B T}} \tag{2.11}$$

The above expression is called the Planck distribution, $n(T)$ and depends directly on the temperature of the system.

This direct dependence on temperature carries over to the free energy expressions. With Eq. 2.3, we obtain the vibrational entropy in the AH approximation, which is the only approximation that reflects this direct dependence. Then we can plug this expression into Eq. 2.4 or Eq. 2.5, giving us the Helmholtz or Gibbs free energy.

We find the other values in Eq.2.4 using density functional theory (DFT) or molecular dynamics (MD) simulations. DFT allows us to perform ground-state electronic structure calculations. We can obtain interatomic forces to calculate the phonon behavior of a system. When using DFT with the lattice dynamics package sTDEP, we set up a workflow shown in Fig. 2.9.

Phonon calculations typically require large supercells rather than unit cells. In crystallography, unit cells are the smallest repeating unit. They come in conventional or primitive. Supercells are the same structure as unit cells, except they are transformed, resulting in a larger volume. It is essential to use supercells in phonon calculations to avoid self-interactions and boundary issues from periodicity in small volumes.

Our workflow needs configurations to simulate the system's behavior at non-zero temperatures. When working with sTDEP, we use a finite number of displaced configurations generated from a canonical distribution. These configurations look like the individual configurations shown in Fig. 2.10.

Performing calculations this way is more computationally feasible than large-scale ab initio molecular dynamics (AIMD). A more detailed explanation of how we applied these methods appears later in this work.

The other way we obtain computational results is using MLIP. The workflow for this method involves training the potential, performing classical MD calculations, and then taking the velocity-autocorrelation.

These theories and approaches are part of a larger concept called many-body theory, which involves the interaction of three or more particles. Figure 2.11 provides an example of interactions in anharmonic many-body systems. In the case of the 3-phonon process, we see phonon creation and annihilation. Annihilation occurs when two phonons come together and result in a single phonon. Creation is the opposite of annihilation: one phonon splits into two new phonons. While the terminology makes it sound like energy is not conserved, that is not the case. The perturbation theory calculations in this work include AH terms up to cubic. Beyond this point, we turn to MLIP.

There is a shift toward formalism like many-body theory, nonlinear dynamics, and

Green's functions. These methods would allow us to capture the potential energy landscape better. The following work compares perturbation theory approaches, machine-learned potentials, and the beginnings of work with many-body theory and Brownian motion.

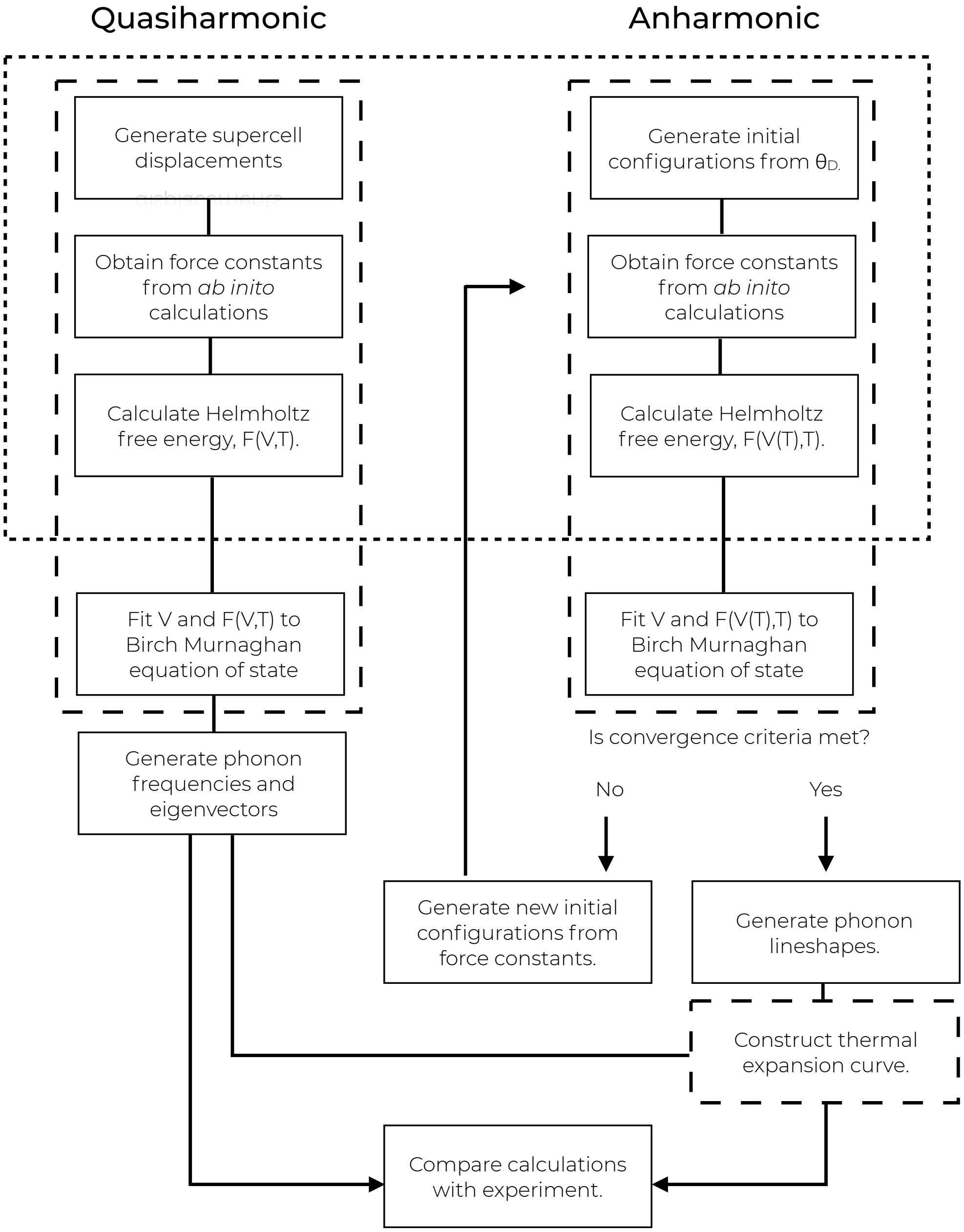

Figure 2.9: A flowchart showing the computational workflows (QH and AH) in parallel. The dotted frame around the first three steps of the QH and AH workflows specifies components of the workflow repeated for volumes at each temperature. Dashed lines designate workflow for each temperature to obtain thermal expansion curves.

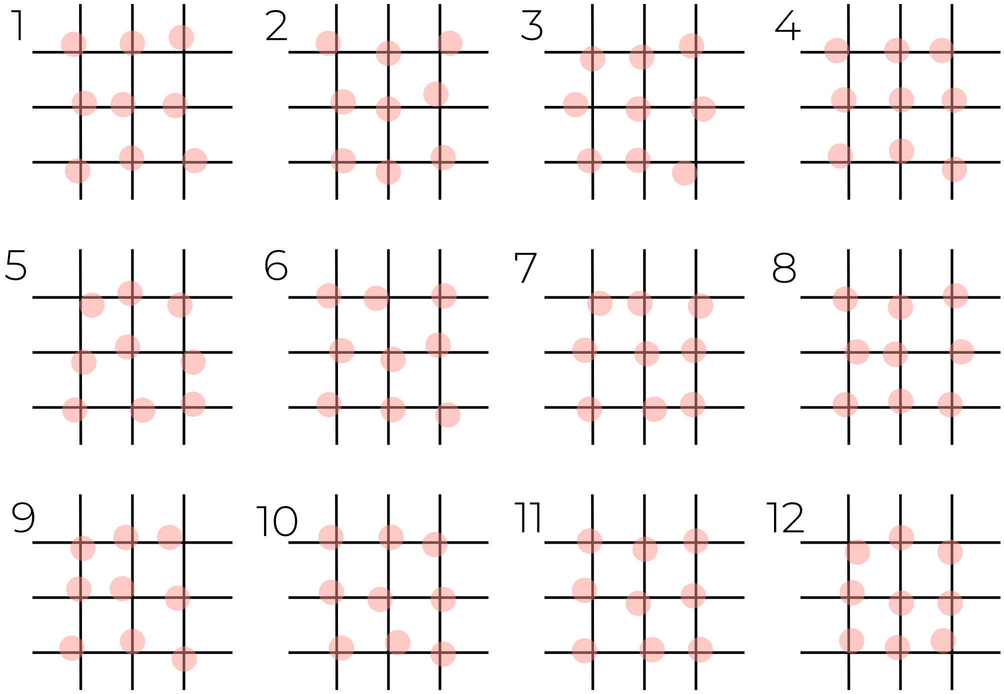

Figure 2.10: A visualization of the snapshots of the atomic canonical configurations generated by sTDEP. The grey lines in each configurations show the ideal crystal lattice equilibrium points.

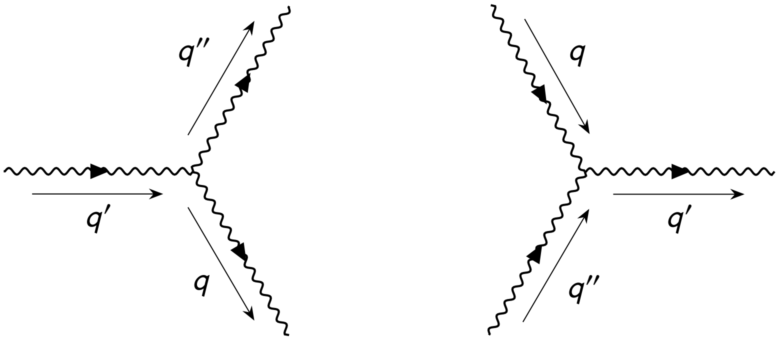

Figure 2.11: Feynman diagrams for the three-phonon processes showing the creation or annihilation of a phonon with wavevector **q**.

References

[1] B. Fultz, JOM **58**, 58 (2006).

[2] T. E. Mason, D. Abernathy, J. Ankner, A. Ekkebus, G. Granroth, M. Hagen, K. Herwig, C. Hoffmann, C. Horak, F. Klose, S. Miller, J. Neuefeind, C. Tulk, and X.-L. Wang, AIP Conf. Proc **773**, 21 (2005).

[3] D. L. Abernathy, M. B. Stone, M. J. Loguillo, M. S. Lucas, O. Delaire, X. Tang, J. Y. Y. Lin, and B. Fultz, Rev. Sci. Instrum **83**, `10.1063/1.3680104` (2012).

[4] E. Fermi, J. Marshall, and L. Marshall, Phys. Rev **72**, `10.1103/PhysRev.72.193` (1947).

Chapter 3

ORIGINS OF THERMAL EXPANSION OF CUPRITE

Adapted from "Thermal expansion and phonon anharmonicity of cuprite studied by inelastic neutron scattering and *ab initio* calculations" [1].

3.1 Introduction

Cuprite, Cu_2O, (Fig. 3.1) is one of the first known semiconductors [2, 3]. It has applications in photovoltaics [4, 5], nanoelectronics [6], thermoelectrics [7], spintronics [8], and catalysis [9, 10]. Below room temperature, cuprite has a small negative thermal expansion (NTE) coefficient that becomes positive at temperatures above 300 K. The coefficient of volumetric thermal expansion,

$$\beta = \frac{1}{V}\frac{\partial V}{\partial T}, \tag{3.1}$$

where V is volume and T is temperature, is explained by a balance between the internal energy, U, and the entropy, S. At finite temperatures, the primary contributions to U and S are the elastic energy, U_{el}, and the vibrational entropy of phonons, S_{vib}, respectively. Using this approximation, the total free energy,

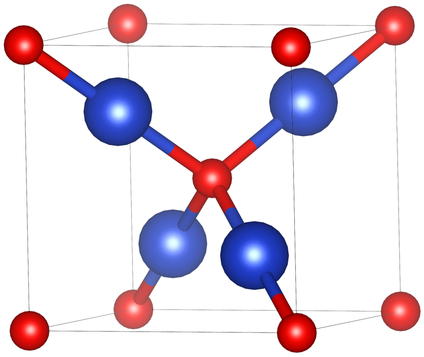

Figure 3.1: Unit cell of Cu_2O. Copper atoms are shown in blue and oxygen atoms in red. There is a linear arrangement of O-Cu-O as the $3z^2 - r^2$ orbitals of copper make chemical bonds with the sp^3 orbitals of oxygen [11].

$$F = U_{el} - TS_{vib}, \tag{3.2}$$

is minimized when reductions in the phonon frequencies with volume (and temperature) cause a larger S_{vib}. These changes counteract the energy penalty from U_{el}

during thermal expansion. Spectroscopies to study phonons include inelastic neutron, inelastic X-ray, and Raman methods. All of these methods have been used to study phonon behavior in cuprite [12–31]. Inelastic neutron scattering (INS) experiments with triple-axis spectrometers measure energy spectra of phonons at single points in crystal momentum, $\vec{q}$. Thermophysical properties such as thermal expansion and the temperature dependence of elastic constants depend on the phonon frequencies at all $\vec{q}$-points in the first Brillouin zone. New methods of INS on single crystals at pulsed neutron sources can provide such detailed information [32, 33]. Measurements of all phonons in a crystal allow testing the basic physics behind microscopic models of thermophysical properties.

Computationally, phonons in materials can be modeled or interpreted with QH or AH theories [34]. The QH vibrational Helmholtz free energy contribution, F_{vib}, depends explicitly on V, and effects of T are only through thermal expansion, i.e., $V(T)$. The F_{vib} in the AH theory used here is:

$$F_{\text{vib}}(V,T) = U_0(V,T) + \sum_{\vec{q},s} \left[\frac{\hbar\omega_{\vec{q},s}(V,T)}{2} + k_B T \ln\left(1 - e^{-\frac{\hbar\omega_{\vec{q},s}(V,T)}{k_B T}}\right)\right] , \quad (3.3)$$

where the phonon frequencies, $\omega_{\vec{q},s}$ (s is a branch index) depend on both V and T. An explicit dependence on T is essential for AH models. Some classify the thermal expansion of materials by magnitude: small, conventional, or giant and sign: positive or negative [35]. In materials with very small NTE, temperature-dependent changes in individual phonon frequencies may be small. Another possibility is that positive and negative contributions to phonon frequency shifts of different phonons cancel one another. This results in an overall small net change in F_{vib}. Further, effective forces between atoms directly depend on V. However, T drives the amplitude of the atomic vibrations about their crystal sites. This effect of T alters how the phonon frequencies change with V. A QH model accounts for the V dependence of the interatomic forces without including the direct effects of thermal displacements of atoms. Materials with small thermal expansions still have thermal displacements, so these materials offer compelling tests of the roles of T and V on thermophysical properties. However, properties averaged over phonon modes, like thermal expansion, do not capture the detailed physics from the relationship between phonon frequencies and the variables T and V.

The present study identifies the microscopic physics of the individual phonon modes that contribute to the macroscopic thermal expansion. We do this by calculating individual phonon contributions to F_{vib} with both QH and AH theory and comparing the thermal trends of the calculated phonons to new phonon measurements by INS on cuprite at 10 K and 300 K.

Previous studies of cuprite showed the success of QH theory for predicting thermal expansion [36–40], and some studies included results on phonon dynamics [36, 37, 41]. We find similar success with the QH theory for thermal expansion but find similar success with an AH theory. Our comparisons of thermal expansion draw on a previous study on the thermal expansion of silicon, another small NTE material. In silicon, the AH effects dominate over the QH effects for thermal phonon shifts at low temperatures even though effects from both theories are small [33, 42].

The net volume change of cuprite from thermal expansion between 10 K and 300 K is small, so QH calculations predict phonon shifts that are nearly zero. Experiment and AH calculations give thermal shifts and broadenings of phonons, especially optical modes. However, the low-frequency acoustic modes are likely more pertinent to the NTE at low temperatures. There are small measurable changes in the acoustic phonons between 10 K and 300 K. Closer examination shows that QH theory predicts changes in both magnitude and sign of the thermal shifts of the lowest acoustic branch that varies with $\vec{q}$.

Nevertheless, AH theory and experiment show that this entire branch undergoes a thermal shift that is nearly the same at all $\vec{q}$. Ultimately, QH theory successfully predicts the small NTE behavior in cuprite. However, the success of QH theory is less compelling when it fails to accurately predict the underlying phonon physics.

3.2 Experiment

Powder

We performed INS measurements on a 20 g powder sample of Cu_2O with the time of flight (TOF) Wide Angular-Range Chopper Spectrometer (ARCS) [32] at the Spallation Neutron Source (SNS) at Oak Ridge National Laboratory (ORNL) [43]. The incident energy was 120 meV, and sample temperatures were 5 K and 300 K. We reduced the data to phonon density of states (DOS) curves. The reduction process included background subtraction of an empty aluminum can and the subtraction of multiphonon correction with Mantid and the Multiphonon package [44, 45].

Single Crystal

Further INS measurements used ARCS to perform measurements on single-crystal cuprite. The [100] oriented single crystal was grown at the Joint Center for Artificial Photosynthesis at Caltech in an optical furnace with the float zone method [46] with 99.999% Cu rods from Alfa Aesar. The crystal was a cylinder of 50 mm in height and 7 mm in diameter, suspended in a platinum holder for all measurements. Images of the crystal and mount are available in Appendix B.

For 10 K measurements, the crystal was in an aluminum canister within a closed-cycle helium refrigerator. TOF neutron spectra were acquired at 152 individual angles of the crystal in increments of 0.5°, about the vertical axis. For 300 K measurements, the crystal was in a low-background electrical resistance vacuum furnace [47]. The measurements at 300 K used 201 angles in increments of 0.5°. The incident energy for all single-crystal measurements was 110 meV. An oscillating radial collimator suppressed multiple scattering and background.

We reduce the single crystal data to obtain the four-dimensional $S(\vec{Q},\varepsilon)$ with the Mantid package. An additional analysis assessed the data statistics and crystal alignment. Then we folded the data from high-$\vec{Q}$ into the irreducible wedge in the first BZ following crystal symmetry. Finally, we subtracted an averaged multiphonon scattering correction from the $S(\vec{Q},\varepsilon)$ and thermally weighted the spectral weights. Figure 3.2 shows the results. Appendix E includes further details of the data post-processing,

3.3 Computation

The Vienna Ab Initio Simulation Package (VASP) was used for all *ab initio* DFT calculations [48–51] with plane wave basis sets, projector augmented wave (PAW) pseudopotentials [52] and the scan meta-GGA exchange correlation functional [53]. All calculations used 3×3×3 supercells containing 162 atoms, a 2×2×2 *k*-grid, and a kinetic energy cutoff of 600 eV. The supercell configurations for calculations were generated with the stochastic Temperature Dependent Effective Potential (sTDEP) method or PHONOPY [54]. For further details on calculation parameters see Appendix C.

Thermal Expansion

Thermal expansion calculations used five supercell volumes centered around the 0 K equilibrium volume. The minimization of the Helmholtz free energy, which consisted of the electronic and phononic contributions, provided an equilibrium volume. The five volumes included were ±1.5% and ±3.0% and the 0 K equilibrium volume. We used PHONOPY for QH calculations at each volume. All QH calculations used the finite displacement method. AH calculations used the sTDEP package [55–57].

Calculating the free energy for each volume is crucial for obtaining thermal expansion curves. We use the following conventions for defining QH and AH free energy. In the QH approximation, Eq. 3.3 reduces to:

$$F_{\mathrm{vib}}^{\mathrm{QH}}(V,T) = U_0(V) + \sum_{\vec{q},s}\left[\frac{\hbar\omega_{\vec{q},s}(V)}{2} + k_B T \ln\left(1 - e^{-\frac{\hbar\omega_{\vec{q},s}(V)}{k_B T}}\right)\right]. \tag{3.4}$$

In the QH approximation, phonon frequencies and ground state energy do not have explicit temperature dependence, but $V = V(T)$ with thermal expansion.

For thermal expansion calculations, AH components are accounted for in $\mathrm{U}_0(T,V)$ and $\omega_{\vec{q},s}(T,V)$. The expression for $\mathrm{U}_0(T,V)$ in our AH thermal expansion calculations is:

$$U_0(V,T) = \left\langle U_{\mathrm{BO}}(V,T) - \frac{1}{2}\sum_{ij}\sum_{\alpha\beta}\Phi_{ij}^{\alpha\beta}u_i^{\alpha}u_j^{\beta}\right\rangle \tag{3.5}$$

where $U_{\mathrm{BO}}(T,V)$ is the Born-Oppenheimer potential energy from sampling the surface and $\Phi_{ij}^{\alpha\beta}$ are forces that are matched between the actual system and with our model Hamiltonian, and $\langle\rangle$ denotes the thermal average. The u_i^{α} and u_j^{β} are Cartesian components of the displacements of atoms i and j. Accounting for third-order terms for phonon self-energies, Eqn. 3.5 becomes:

$$U_0(V,T) = \left\langle U_{\mathrm{BO}}(V,T) - \frac{1}{2!}\sum_{ij}\sum_{\alpha\beta}\Phi_{ij}^{\alpha\beta}u_i^{\alpha}u_j^{\beta} - \frac{1}{3!}\sum_{ijk}\sum_{\alpha\beta\gamma}\Phi_{ijk}^{\alpha\beta\gamma}u_i^{\alpha}u_j^{\beta}u_k^{\gamma}\right\rangle. \tag{3.6}$$

In all the above expressions, the partial derivatives of U_0 and in $\omega_{\vec{q},s}(T,V)$ account for the AH components. After the lattice parameter was found by minimizing the free energy at a given temperature, phonon dispersions and self-energy are calculated for this temperature.

Mode Grüneisen Parameters

Previous studies of lattice dynamics and the NTE of cuprite employed the QH approximation. In QH theory, each phonon mode s with corresponding angular frequency $\omega_{\vec{q},s}$ depends directly on the volume through the mode Grüneisen parameter, $\gamma_{\vec{q},s}$, at a given wave vector $\vec{q}$,

$$\gamma_{\vec{q},s}(V) = -\frac{V}{\omega_{\vec{q},s}(V)} \frac{\partial \omega_{\vec{q},s}(V)}{\partial V}. \tag{3.7}$$

Equation 3.7 predicts thermal shifts of individual phonon frequencies. An average γ, where each $\gamma_{\vec{q},s}$, is weighted by the contribution of phonon s to the heat capacity, predicts the macroscopic thermal expansion. Average phonon frequencies decrease for positive values of γ as volume increases. This decrease in $\omega_{\vec{q},s}$ positively contributes to the vibrational entropy, S_{vib}, and lowers the QH vibrational Helmholtz free energy, F^{QH}.

For AH computations, where third-order force constants are available [58], the mode Grüneisen parameters for a mode with frequency $\omega_{\vec{q},s}$ is:

$$\gamma_{\vec{q},s}(V,T) = -\frac{V}{6\omega_{\vec{q},s}(V,T)^2} \sum_{ijk\alpha\beta\gamma} \frac{\epsilon^{i\alpha\dagger}_{\vec{q},s} \epsilon^{j\beta}_{\vec{q},s}}{\sqrt{m_i m_j}} r^{\gamma}_{k} \Phi^{\alpha\beta\gamma}_{ijk} e^{\vec{q}\cdot\vec{r}_j}. \tag{3.8}$$

In this equation, $\Phi^{\alpha\beta\gamma}_{ijk}$ is the cubic anharmonicity tensor with Cartesian indices α, β, γ. ϵ is the polarization eigenvector, and atomic position and mass are designed by $\vec{r}$ and m, respectively. Equation 3.8 offers an advantage over Eq. 3.7 because it is not divergent when the thermal expansion is zero. The mode Grüneisen parameters were calculated using Eq. 3.8. All calculations were performed in sTDEP using the third order force constants.

Phonon Self-Energy

The calculated phonon self-energy gives phonon spectra with thermal shifts and finite linewidths. Calculations of this include terms to the third power of atom displacements (cubic anharmonicity) [59, 60]. The AH calculations of the self-energy were performed in sTDEP. The solution of the dynamical matrix provided frequencies. For a given third-order force constant,$\Phi_{ss's''}$ the phonon self-energy was calculated and adjusted with the real Δ and imaginary Γ corrections to the phonon self-energy. The imaginary correction to the phonon self-energy is:

$$\begin{aligned}\Gamma^{\vec{q}\vec{q}'\vec{q}''}_{ss's''}(V,T) = \frac{\hbar\pi}{16} \sum_{ss's''} \left|\Phi^{\vec{q}\vec{q}'\vec{q}''}_{ss's''}\right|^2 & \left(n_{\vec{q}',s'} + n_{\vec{q}'',s''} + 1\right) \times \delta\left(\Omega - \omega_{\vec{q}',s'} - \omega_{\vec{q}'',s''}\right) \\ & + \left(n_{\vec{q}',s'} - n_{\vec{q}'',s''}\right)\left[\delta\left(\Omega - \omega_{\vec{q}',s'} + \omega_{\vec{q}'',s''}\right)\right. \\ & \left. - \delta\left(\Omega + \omega_{\vec{q}',s'} - \omega_{\vec{q}'',s''}\right)\right],\end{aligned} \tag{3.9}$$

where $\hbar\Omega$ is a probing energy, $\omega^2_{\vec{q},s}$ are the eigenvalues of the dynamical matrix, and n are the occupancy factors. The three-phonon matrix component can be written as:

$$\Phi^{\vec{q}\vec{q}'\vec{q}''}_{ss's''} = \sum_{ijk} \sum_{\alpha\beta\gamma} \frac{\epsilon^{i\alpha}_{s} \epsilon^{j\beta}_{s'} \epsilon^{k\gamma}_{s''}}{\sqrt{m_i m_j m_k} \sqrt{\omega_{\vec{q},s} \omega_{\vec{q}',s'} \omega_{\vec{q}'',s''}}} \Phi^{\alpha\beta\gamma}_{ijk} e^{i\left(\vec{q}\cdot\vec{r}_i + \vec{q}'\cdot\vec{r}_j + \vec{q}''\cdot\vec{r}_k\right)}, \tag{3.10}$$

where the primes help identify the three-phonon interactions. Remaining indices are defined in Eq. 3.8.

The real component of the phonon self-energy is obtained from the Kramers–Kronig transform:

$$\Delta_{\vec{q},s}(\Omega_{\vec{q},s}) = \frac{1}{\pi} \int \frac{\Gamma(\omega_{\vec{q},s})}{\omega_{\vec{q},s} - \Omega} d\omega_{\vec{q},s} \tag{3.11}$$

Large deviations of $\Delta_{\vec{q},s}(\Omega_{\vec{q},s})$ from a Lorentzian function suggests a high degree of anharmonicity.

3.4 Results

Figure 3.3 shows the percentage change in lattice parameter of cuprite versus temperature, referenced to a nominal 0 K. Panel A compares the sTDEP lattice parameter to experimental results. Panel B corresponds to our QH calculations and other QH calculations in the literature. Both QH and AH calculations below 250 K reproduce the measured negative thermal expansion. However, the thermal expansion coefficient in this region is small, less than -2.4×10^{-6}/K, and is zero near 250 K.

Figure 3.4b shows the calculated sTDEP phonon partial DOS curves for Cu and O atoms in cuprite. The O atoms dominate the spectral weight in the high-energy modes between 65 and 80 meV, and Cu atoms dominate below 45 meV. Their sum agrees with the experimental spectra from INS measurements shown in Fig. 3.4a, without neutron-weight corrections.

Grüneisen parameters from sTDEP with Eq. 3.8 are shown in Figs. 3.5a,c at different temperatures. These Grüneisen parameters are in good agreement with prior QH calculations and experimental results [40]. The plotted mode Grüneisen parameters correspond to the same color mode in the dispersions in Fig. 3.5 b,d. Many of the low-energy dispersions have negative Grüneisen parameters. This includes the low-energy transverse acoustic (TA) modes that are useful for explaining the negative thermal expansion in QH theory. The high-energy optical modes have positive Grüneisen parameters. Still, these are similar to the Grüneisen parameters of other phonon branches. Modes with similar Grüneisen parameters are predicted by QH theory to have similar thermal shifts.

The real and imaginary parts of the phonon self-energy at the point $\vec{Q} = (0.25, 0.25, 0.00)$ are shown in Fig. 3.6, colored in correspondence with their phonon branches in Fig. 3.5. There are large deviations from the harmonic self-energy for the optical modes with energies above 70 meV, showing that these modes are more anharmonic than the others. There are significant cubic AH effects for the optical modes around 40 meV. A comparison of the partial phonon DOS to the phonon self-energies shows that the displacements of oxygen atoms dominate these AH modes.

Figure 3.2 shows phonon spectra from INS measurements and AH calculations along high-symmetry crystallographic directions. Figures 3.2a) and b) show the folded experimental data from the single crystal at 10 and 300 K, respectively, and Figs. 3.2 c) and d) show the corresponding AH sTDEP calculations. The main features and energies of the calculated and measured intensities agree. Both calculated and measured data show softening of the high-energy optical modes. However, the calculated softening of these modes is larger than the experimental results. Below 45 meV, small changes in the calculated and measured dispersions follow the same thermal trends.

Figure 3.7 compares experimental cuts taken at single points along the high symmetry path with cuts from sTDEP lineshape calculations with QH dispersion results from PHONOPY. The AH results show thermal shifts, but the QH calculations display no noticeable changes with the temperature on the scale of Fig. 3.7.

3.5 Discussion

Without magnetism, the coefficient of thermal expansion, β, in thermodynamic equilibrium from the Gibbs free energy, G, is:

$$\begin{aligned} G(T,P,N) &= U - TS + PV \,, && (3.12) \\ \frac{\partial^2 G}{\partial T \partial P} &= \frac{\partial V}{\partial T} = V\beta \,. && (3.13) \end{aligned}$$

The average nuclear spacing increases with increasing increasing V. This results in an increase in the internal energy, U, of the system as the electronic energy increases from the ground state value. (This U is different from the U_0 in Eq. 3.3.) The contribution from phonons appears primarily in the entropy term, S. For cuprite, the phonon entropy, S_{vib}, dominates the entropy. The S_{vib} directly depends on the phonon frequencies $\omega_{\vec{q},s}$. With anharmonicity, we assume $\omega_{\vec{q},s}$ depends independently on both T and V. In quasiharmonicity, we assume $\omega_{\vec{q},s}(V(T))$ so all effects from T originate solely with $\Delta V = \beta T$.

The AH sTDEP calculations better predict the measured effects of temperature on phonons than QH PHONOPY calculations. We see this in the energy cuts of Fig. 3.7. For cuprite, Grüneisen parameters from sTDEP and QH calculations are essentially the same [40]. In the QH approximation, phonon shifts follow the $\vec{q}$-dependence of the Grüneisen parameters shown in Eq. 3.13. This QH trend is not the thermal trend of the phonon branches; there are two differences. First, the phonon frequencies depend solely on volume in QH theory, so it predicts a negligible difference between calculated dispersions at 10 K and 300 K. While the thermal shifts are small, they are measurable and larger than predicted by QH calculations. Figure 3.5shows a second problem. For the low TA branch at the X point, the Grüneisen parameter is –4, whereas it is approximately $+5$ at the R point. However, in Fig. 3.2 the entire low TA branch in the experimental results shifts upwards in energy with increasing temperature. This also appears in Fig. 3.7.

There are no observable differences in the behavior at the X or R points. The Grüneisen parameters for the low-energy optical branches also change signs at different $\vec{q}$. However, branches from sTDEP have simple behavior. The modes below 11 meV shift upwards and above 11 meV shift downwards with temperature.

The thermal expansion of Eq. 3.13 depends only on the temperature dependence of U through the electronic energy, and the temperature dependence of S through the phonon frequencies, $\mathrm{d}\omega_{\vec{q},s}/\mathrm{d}T$. Since the QH approximation does not reliably predict the $\mathrm{d}\omega_{\vec{q},s}/\mathrm{d}T$, it cannot be reliable for predicting the thermal expansion. Nevertheless, the QH approximation gives generally good results, as shown in Fig. 3.3. With its prediction of very small shifts in phonon frequencies between 10 K and 300 K, it is difficult to pinpoint why the QH approximation might be successful in predicting the thermal expansion. We attribute the success to a cancellation of errors because for many phonons, the $\mathrm{d}\omega_{\vec{q},s}/\mathrm{d}T$ has the wrong sign.

Three-phonon processes are subject to kinematic constraints. The energy constraint requires pairs of lower energy phonons can add their energy to create a higher-energy phonon. This process alters the self energies, and Fig. **??** shows peaks at some energies where the self-energy corrections are significant. For example, at 10 K, most of the 3-phonon processes involve down-conversion and dominate the high energy optical modes at 300 K (the self-energy corrections above 40 meV are similar at 10 and 300 K). Figure **??** shows that other self-energy corrections are becoming more significant at 300 K than at 10 K. An examination of the self-energy corrections and the phonon partial DOS curves of Fig. 3.4 shows that a large cubic anharmonicity is associated with optical modes (oxygen). A modest cubic anharmonicity is from acoustic modes dominated by copper atoms.

The calculated broadenings of phonon dispersions at energies below 50 meV are not as large as the experimental phonon dispersions in Fig. 3.2. A previous study attributed some of the thermal behavior of cuprite to quartic anharmonicity [39]. Quartic anharmonicity can account for further shifts of phonon energies. However, it cannot account for phonon lineshapes. This is because the loop diagram for the quartic term does not have an imaginary part. Higher-order AH processes may be needed to account for the measured thermal broadening and shifts of phonons in cuprite. Therefore, it seems challenging for perturbation theory to predict the thermal shifts of phonons in cuprite at higher temperatures.

3.6 Conclusions

INS with a pulsed neutron source and area detector measured all phonons in a cuprite single-crystal at 10 K and 300 K. The phonons from QH and AH calculations and experiments were compared directly. The AH theory better described the temperature-dependent phonon behavior than the QH theory. The temperature dependence of the low-energy transverse acoustic and high-energy optical modes did not follow the experimental change in volume predicted by QH theory. This QH change in volume was nearly zero because the volumes at 10 K and 300 K are almost the same. Calculations with AH theory predicted these shifts better than the QH theory. Nevertheless, the self-energy calculated with the AH theory failed to capture the full thermal broadening of the measured optical modes. For cuprite, details of the measured phonon dispersions may require higher-order anharmonicity.

Both QH and AH models successfully calculated the small NTE in cuprite. Thermophysical properties such as thermal expansion are averages over numerous microscopic contributions to the Gibbs free energy. The reliability of a model that predicts thermal expansion should be tested against its predictions of the underlying microscopic processes, such as the thermal softening of individual phonons.

With this criterion, the QH theory is less compelling than the AH theory because it predicts incorrect phonon behavior.

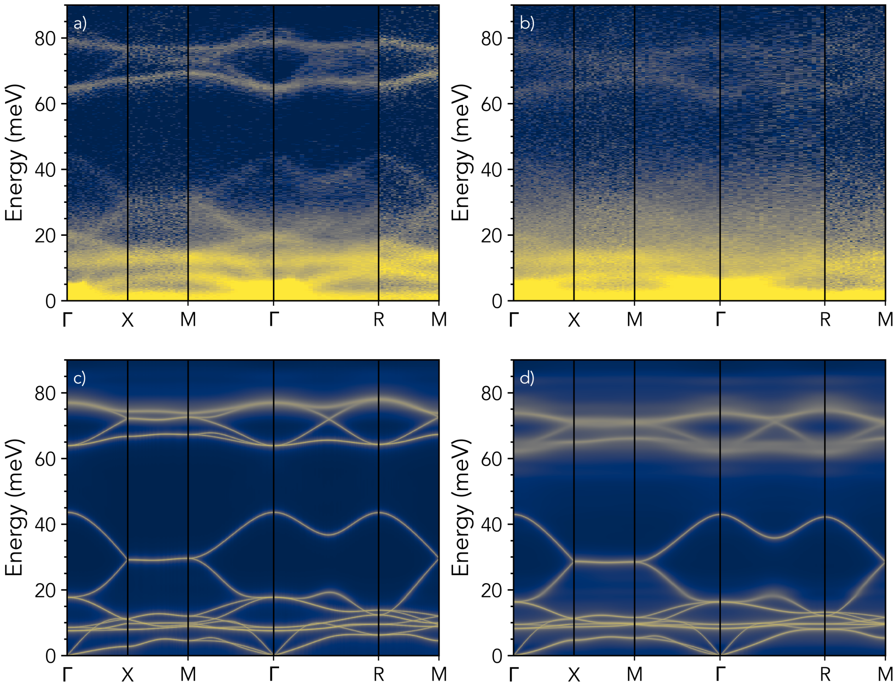

Figure 3.2: Experimental and calculated phonon dispersions along high-symmetry directions of cuprite. Experimental phonon dispersions measured by INS are shown at (a) 10 K and (b) 300 K. Computational phonon dispersions calculated by sTDEP are shown at (c) 10 K and (d) 300 K.

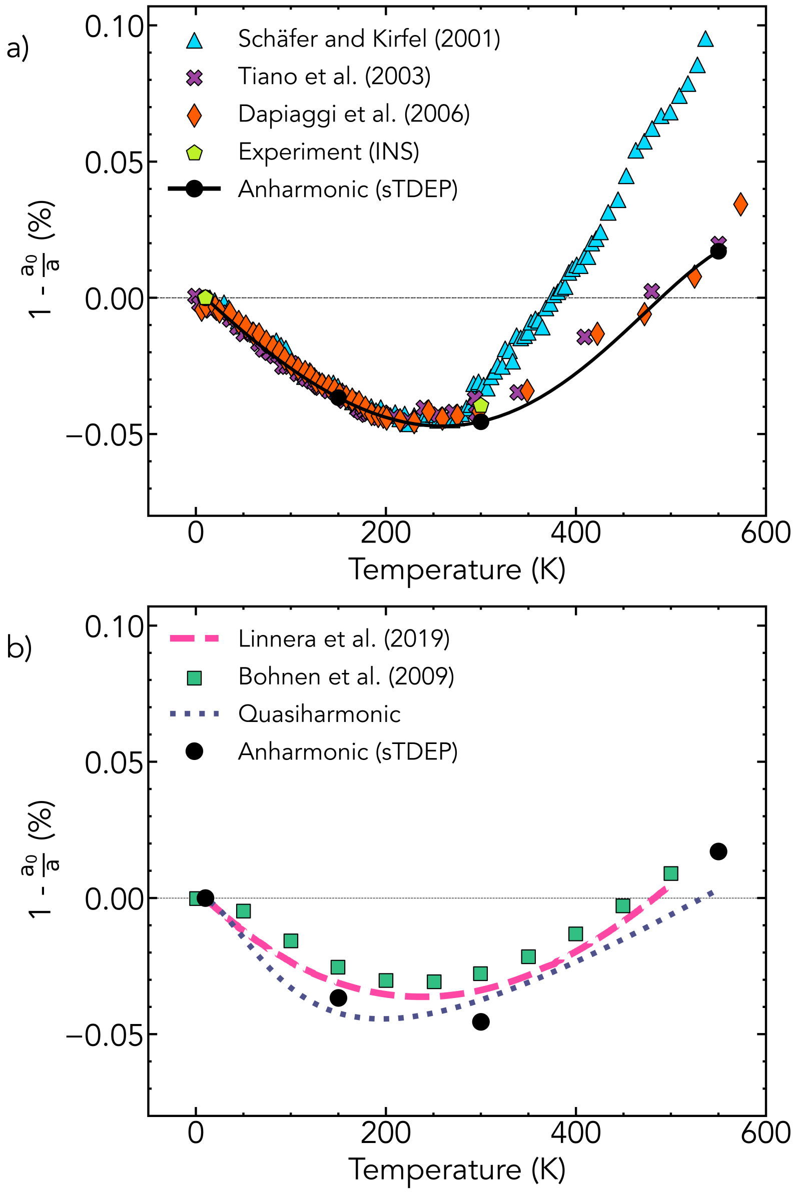

Figure 3.3: Percentage change with temperature of lattice parameter of cuprite from experiment and computation. (a) Experimental results [29–31, 61] are shown as colored markers, compared to AH result from minimized free energies using sTDEP. (b) Calculated percentage change of lattice parameter versus temperature. QH results are colored line and markers [37, 40], compared to sTDEP results shown with black circles.

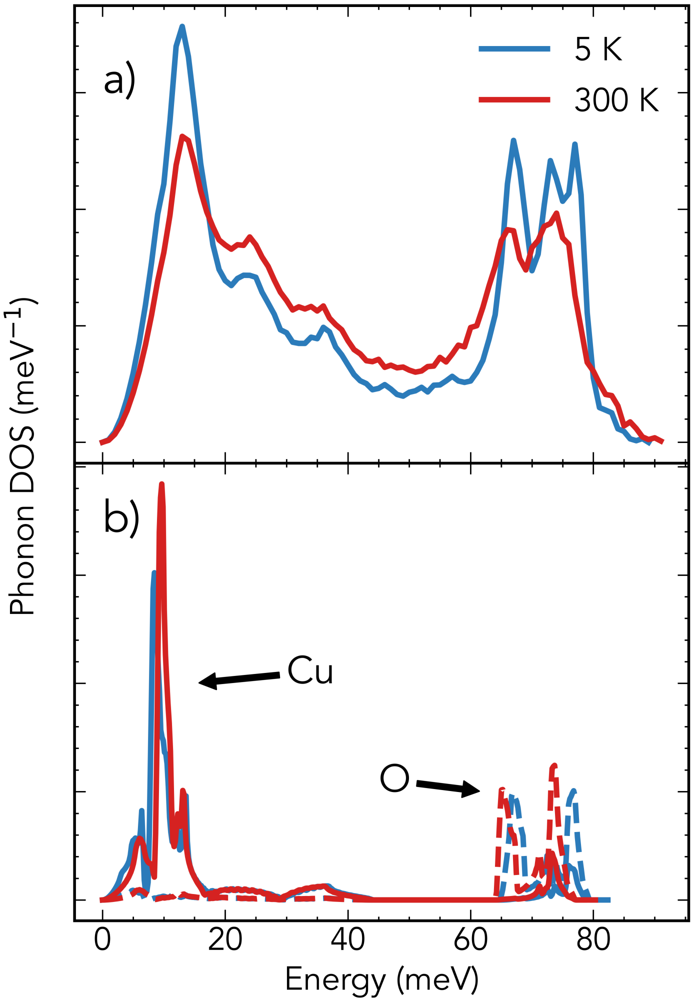

Figure 3.4: Experimental and calculated phonon DOS of cuprite. (a) Phonon DOS from INS measurements on powdered cuprite. (b) Phonon partial DOS from sTDEP calculations using second order terms at 10 K and 300 K. Solid curves are Cu, dashed are O atoms.

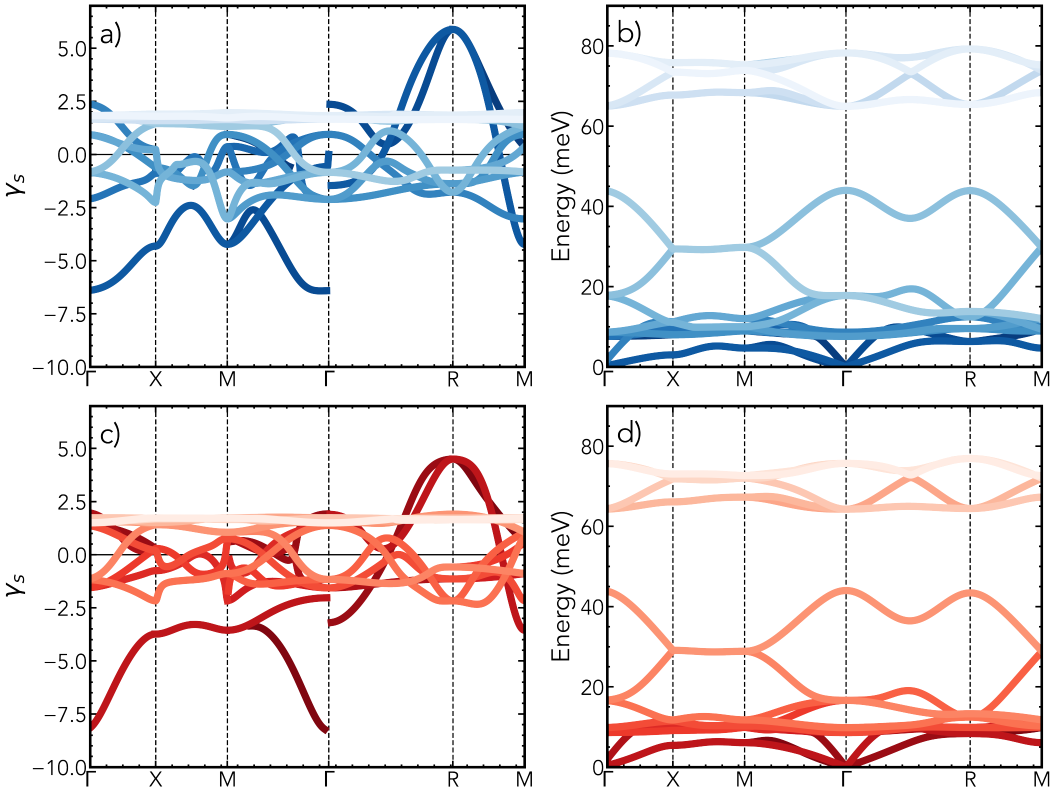

Figure 3.5: Calculated mode Grüneisen parameters for cuprite. Mode Grüneisen parameters for dispersions, shaded to match their corresponding dispersions at (a) 10 K and (c) 300 K. (b,d) Phonon dispersions from quadratic terms in sTDEP calculations at (b) 10 K and (d) 300 K colored to correspond with their matching mode Grüneisen parameters.

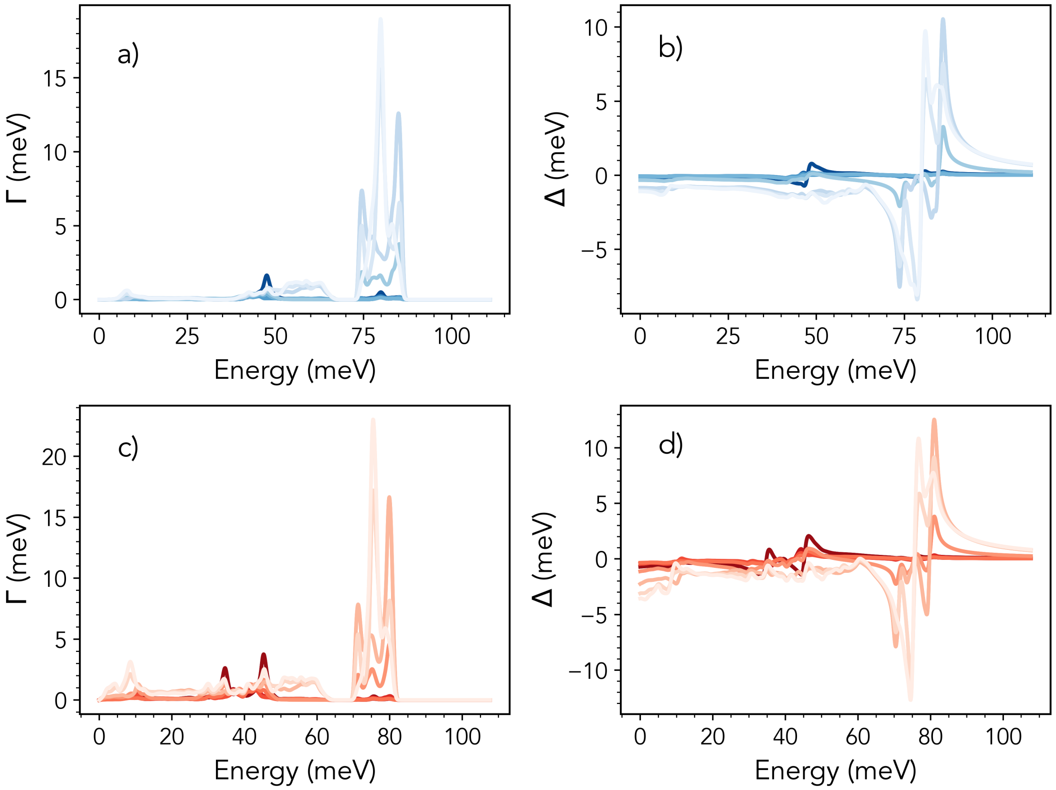

Figure 3.6: Real and imaginary components of the phonon self energy of cuprite. (a,c) are the imaginary part (Γ) of the phonon self-energy at 10 K in blue and 300 K shown in red. Different shades of red and blue correspond to individual modes designated by Figs. 3.5 (b,d), which show the real part (Δ) of the phonon self-energy. Data are for $\vec{Q} = (0.25, 025, 0.0)$.

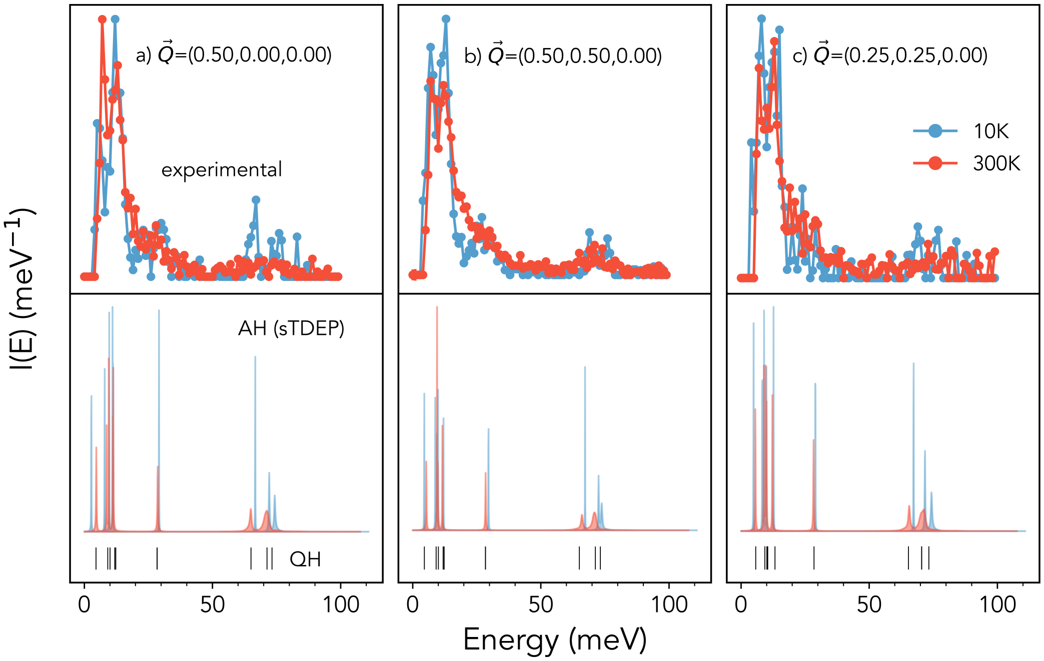

Figure 3.7: Calculated and experimental energy spectra at specific values of $\vec{Q}$. Energy spectra at three values of $\vec{Q}$ at 10 K (blue) and 300 K (red). (a) Energy cut at X-point for experimental (top panel), AH calculations (lower panel), and QH calculation (lower panel, black lines) at labeled temperatures. (b) This plot shows the energy cut at M-point. (c) This plot shows the energy cut halfway between the high symmetry points X and M. The color specifies the experimental and computational data temperature. Both temperatures of the QH data are denoted by black at the bottom because there is no discernible change of QH phonons between 10 K and 300 K.

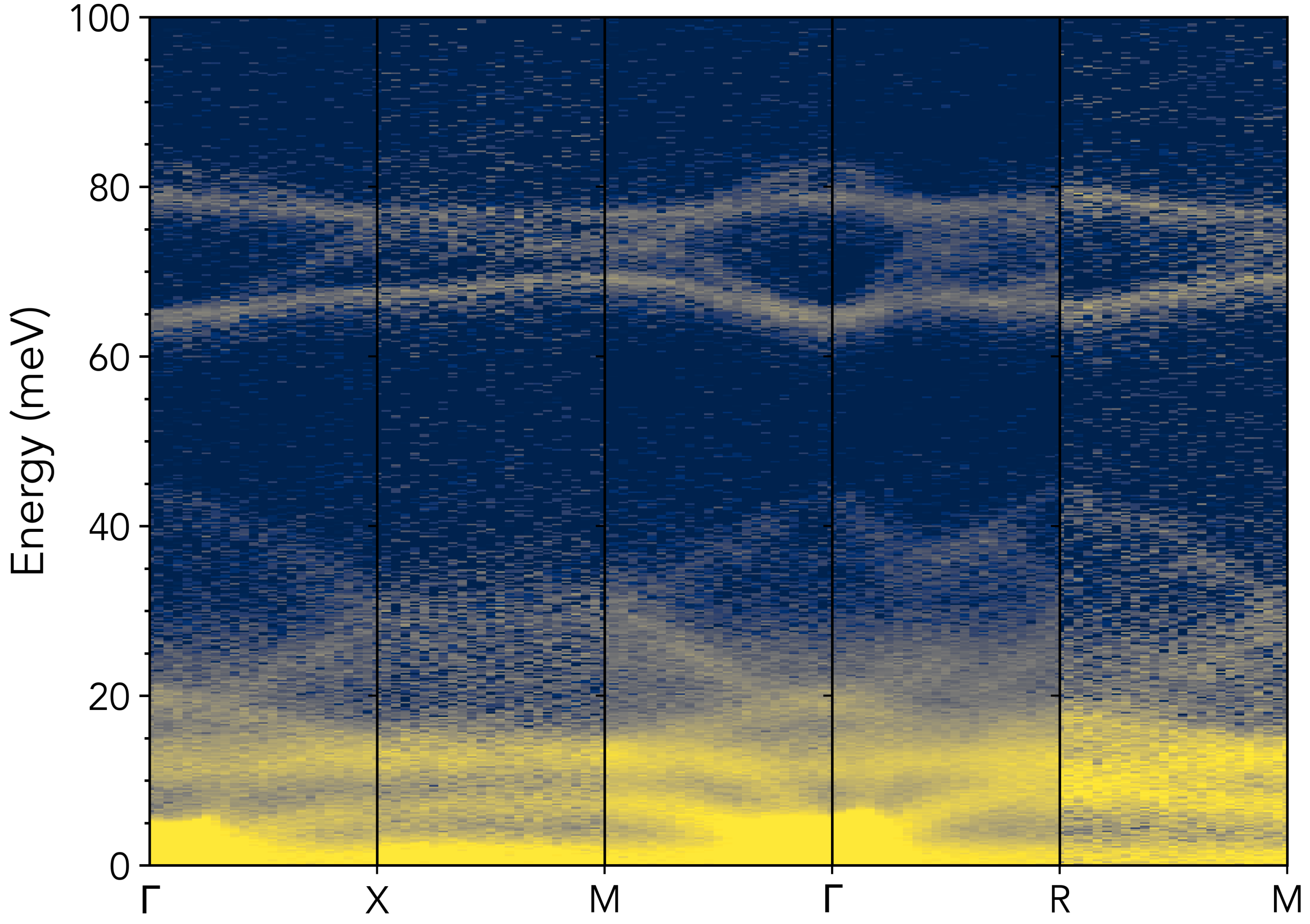

Figure 3.8: Experimental phonon dispersion at 10 K. Zoomed-in portion of Fig. 3.2(a).

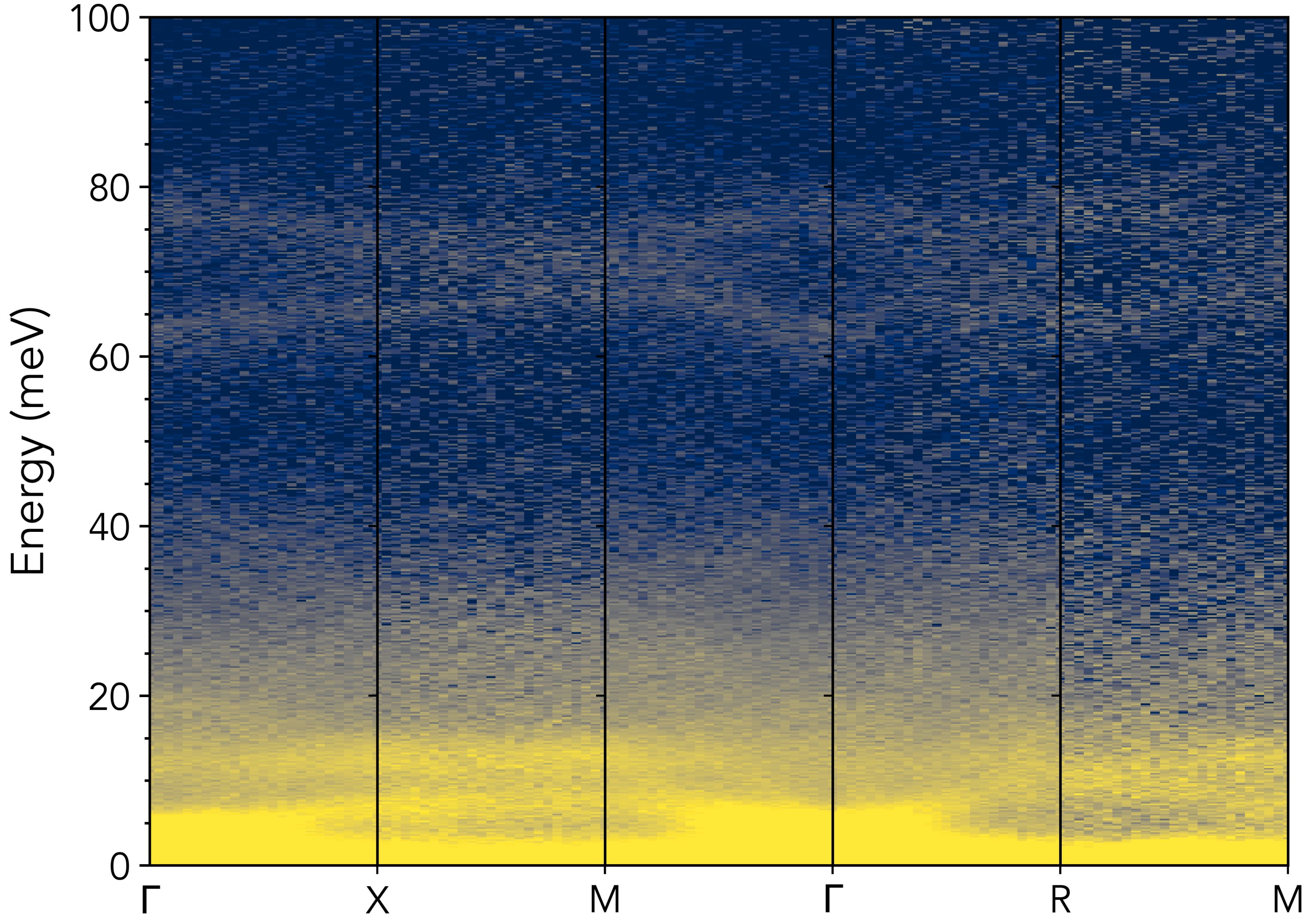

Figure 3.9: Experimental phonon dispersion at 300 K. Zoomed in portion of Fig. 3.2(c).

References

[1] C. N. Saunders, D. S. Kim, O. Hellman, H. L. Smith, N. J. Weadock, S. T. Omelchenko, G. E. Granroth, C. M. Bernal-Choban, S. H. Lohaus, D. L. Abernathy, and B. Fultz, Phys. Rev. B (in press).

[2] W. Mönch, in *Semiconductor surfaces and interfaces* (Springer, Berlin, Heidelberg, 2001), pp. 1–20.

[3] A. Schuster, Phil. Mag. **48**, 251 (1874).

[4] Y. Abdu and A. O. Musa, Rev. Mod. Phys. **2**, 8 (2009).

[5] W. H. Brattain, Rev. Mod. Phys. **23**, 203 (1951).

[6] K. Mikami, Y. Kido, Y. Akaishi, A. Quitain, and T. Kida, Sensors **19**, 1 (2019).

[7] J. Linnera, G. Sansone, L. Maschio, and A. J. Karttunen, J. Phys. Chem. C **122**, 15180 (2018).

[8] D. Y. Kim, C. W. Kim, J. H. Sohn, K. J. Lee, M. H. Jung, M. G. Kim, and Y. S. Kang, J. Phys. Chem. C **119**, 13350 (2015).

[9] M. B. Gawande, A. Goswami, F.-X. Felpin, T. Asefa, X. Huang, R. Silva, X. Zou, R. Zboril, and R. S. Varma, Chem. Rev. **116**, 3722 (2016).

[10] L. Wan, Q. Zhou, X. Wang, T. E. Wood, L. Wang, P. N. Duchesne, J. Guo, X. Yan, M. Xia, Y. F. Li, A. A. Jelle, U. Ulmer, J. Jia, T. Li, W. Sun, and G. A. Ozin, Nat. Catal. **2**, 889 (2019).

[11] J. Zuo, M. Kim, M. O'Keeffe, and J. Spence, Nature **401**, 49 (1999).

[12] R. J. Elliott, Phys. Rev. **124**, 340 (1961).

[13] K. Huang, Z. Phys. **171**, 213 (1963).

[14] C. Carabatos, Phys. Status Solidi B **37**, 773 (1970).

[15] J. Hallberg and R. C. Hanso, Phys. Status Solidi B **42**, 305 (1970).

[16] G. Kugel, C. Carabatos, W. Kress, and H. Id, J. Phys. Colloques **42**, C6-884 - C6 (1981).

[17] Y. Petroff, P. Y. Yu, and Y. R. Shen, Phys. Rev. B **12**, 2488 (1975).

[18] A. Compaan, Solid State Commun. **16**, 293 (1975).

[19] P. Dawson, M. Hargreave, and G. Wilkinson, J. Phys. Chem. Solids **34**, 2201 (1973).

[20] J. Reydellet, M. Balkanski, and D. Trivich, Phys. Status Solidi B **52**, 175 (1972).

[21] A. Compaan and H. Z. Cummins, Phys. Rev. B **6**, 4753 (1972).

[22] P. Y. Yu, Y. R. Shen, Y. Petroff, and L. M. Falicov, Phys. Rev. Lett. **30**, 283 (1973).

[23] J. C. W. Taylor and F. L. Weichman, Can. J. Phys. **49**, 601 (1971).

[24] M. Balkanski, M. Nusimovici, and J. Reydellet, Solid State Commun. **7**, 815 (1969).

[25] E. C. Heltemes, Phys. Rev. **141**, 803 (1966).

[26] M. O'Keeffe, The Journal of Chemical Physics **39**, 1789 (1963).

[27] K. Reimann and K. Syassen, Phys. Rev. B **39**, 11113 (1989).

[28] G. K. White, J. Phys. C: Solid State Phys. **11**, 2171 (1978).

[29] W. Tiano, M. Dapiaggi, and G. Artioli, J. Appl. Crystallogr. **36**, 1461 (2003).

[30] A. Sanson, F. Rocca, G. Dalba, P. Fornasini, R. Grisenti, M. Dapiaggi, and G. Artioli, Phys. Rev. B **73**, 214305 (2006).

[31] M. Dapiaggi, W. Tiano, G. Artioli, A. Sanson, and P. Fornasini, Nucl. Instrum. Methods Phys. Res., B **200**, 231 (2003).

[32] D. L. Abernathy, M. B. Stone, M. J. Loguillo, M. S. Lucas, O. Delaire, X. Tang, J. Y. Y. Lin, and B. Fultz, Rev. Sci. Instrum **83**, 10.1063/1.3680104 (2012).

[33] D. S. Kim, O. Hellman, J. Herriman, H. L. Smith, J. Y. Y. Lin, N. Shulumba, J. L. Niedziela, C. W. Li, D. L. Abernathy, and B. Fultz, Proc. Natl. Acad. Sci. U. S. A. **115**, 1992 (2018).

[34] P. B. Allen, Mod. Phys. Lett. B **34**, 2050025 (2020).

[35] K. Takenaka, Front. Chem. **6**, 267 (2018).

[36] R. Mittal, S. L. Chaplot, S. K. Mishra, and P. P. Bose, Phys. Rev. B **75**, 174303 (2007).

[37] K.-P. Bohnen, R. Heid, L. Pintschovius, A. Soon, and C. Stampfl, Phys. Rev. B **80**, 134304 (2009).

[38] L. H. Rimmer, M. T. Dove, B. Winkler, D. J. Wilson, K. Refson, and A. L. Goodwin, Phys. Rev. B **89**, 28 (2014).

[39] M. K. Gupta, R. Mittal, S. L. Chaplot, and S. Rols, J. Appl. Phys. **115**, 093507 (2014).

[40] J. Linnera, A. Erba, and A. J. Karttunen, J. Chem. Phys. **151**, 184109 (2019).

[41] M. M. Beg and S. M. Shapiro, Phys. Rev. B **13**, 1728 (1976).

[42] E. T. Ritz, S. J. Li, and N. A. Benedek, Journal of Applied Physics **126**, 171102 (2019).

[43] T. Mason, D. Abernathy, I. Anderson, J. Ankner, T. Egami, G. Ehlers, A. Ekkebus, G. Granroth, M. Hagen, K. Herwig, J. Hodges, C. Hoffmann, C. Horak, L. Horton, F. Klose, J. Larese, A. Mesecar, D. Myles, J. Neuefeind, M. Ohl, C. Tulk, X.-L. Wang, and J. Zhao, Physica B Condens. **385-386**, 955 (2006).

[44] O. Arnold, J. Bilheux, J. Borreguero, A. Buts, S. Campbell, L. Chapon, M. Doucet, N. Draper, R. Ferraz Leal, M. Gigg, V. Lynch, A. Markvardsen, D. Mikkelson, R. Mikkelson, R. Miller, K. Palmen, P. Parker, G. Passos, T. Perring, P. Peterson, S. Ren, M. Reuter, A. Savici, J. Taylor, R. Taylor, R. Tolchenov, W. Zhou, and J. Zikovsky, Nucl. Instrum. Meth. A **764**, 156 (2014).

[45] J. Y. Y. Lin, F. Islam, and M. Kresh, J. Open Source Softw. **3**, 440 (2018).

[46] S. T. Omelchenko, Y. Tolstova, S. S. Wilson, H. A. Atwater, and N. S. Lewis, in 2015 ieee 42nd photovoltaic specialist conference (pvsc) (2015), pp. 1–4.

[47] J. L. Niedziela, R. Mills, M. J. Loguillo, H. D. Skorpenske, D. Armitage, H. L. Smith, J. Y. Y. Lin, M. S. Lucas, M. B. Stone, and D. L. Abernathy, Rev. Sci. Instrum **88**, 105116 (2017).

[48] G. Kresse and J. Hafner, Phys. Rev. B **47**, 558 (1993).

[49] G. Kresse and J. Hafner, Phys. Rev. B **49**, 14251 (1994).

[50] G. Kresse and J. Furthmüller, Comput. Mater. Sci. **6**, 15 (1996).

[51] G. Kresse and J. Furthmüller, Phys. Rev. B **54**, 11169 (1996).

[52] G. Kresse and D. Joubert, Phys. Rev. B **59**, 1758 (1999).

[53] J. Sun, A. Ruzsinszky, and J. P. Perdew, Phys. Rev. Lett. **115**, 036402 (2015).

[54] A. Togo and I. Tanaka, Scr. Mater. **108**, 1 (2015).

[55] O. Hellman, I. A. Abrikosov, and S. I. Simak, Phys. Rev. B **84**, 180301 (2011).

[56] O. Hellman, P. Steneteg, I. A. Abrikosov, and S. I. Simak, Phys. Rev. B **87**, 104111 (2013).

[57] O. Hellman and I. A. Abrikosov, Phys. Rev. B **88**, 144301 (2013).

[58] T. H. K. Barron and M. L. Klein, "Perturbation theory of anharmonic crystals", in *Dynamical properties of solids*, edited by G. Horton and A. Maradudin (North-Holland, Amsterdam, 1974), p. 391.

[59] A. A. Maradudin and A. E. Fein, Phys. Rev. **128**, 2589 (1962).

[60] D. C. Wallace, *Statistical physics of crystals and liquids* (World Scientific, 2003).

[61] W. Schäfer and A. Kirfel, Appl. Phys. A **74**, s1010 (2002).

Chapter 4

DIFFUSE INELASTIC INTENSITY IN PHONON SPECTRA OF CUPRITE

4.1 Introduction

This chapter presents experimental and computational evidence of a newly observed intensity contribution to the inelastic phonon spectrum. We can conclude that this spectrum, which we call diffuse inelastic intensity (DII), is not attributable to instrument artifacts, sample defects, or post-processing techniques. In what follows, we present several physical models to explain the DII along with its broader implications in anharmonic (AH) solids.

Recent advances in measurements and computations of AH solids has prompted new interest in AH effects beyond the cubic perturbation term [1, 2]. While this study is the first to observe and interpret the DII, the DII likely falls under a broader category of AH features classified as local nonlinear quantum processes in many-body systems. Existing examples of these processes include intrinsic localized modes (ILM) [3–6], intermodulation phonon sidebands (IPS) [1, 7–9], and AH interference [10, 11].

Throughout this chapter, AH effects exclusively mean phonon-phonon interactions unless otherwise specified. These interactions shift the central position of the spectral intensity of individual phonon modes to a higher or lower energy value, commonly called stiffening or softening, respectively. Another AH change in phonon branches is lineshape broadening. When a branch broadens, the width of the spectral branch, which is given a quantitative value through a fitting, correlates to an increase in the full width at half maximum. For a phonon of energy, $\hbar\Omega$, the phonon self-energy correction is [12]:

$$\Sigma(\Omega) = \Delta(\Omega) + i\Gamma(\Omega), \tag{4.1}$$

where the real component, Δ, shifts the phonon energy and the imaginary component, Γ, broadens the phonon branches. $\hbar\Omega$ is the phonon energy often called the probing energy. We indirectly measure this energy in INS experiments with neutron arrival times at the detectors.

The DII presents as a temperature-dependent spectral band of nonuniform intensity spread over a finite frequency range of the phonon spectra. Due to its broadening nature, we focus on the imaginary component of the phonon self-energy, Γ. The three-phonon interaction is [12]:

$$\begin{aligned}\Gamma_\lambda(\Omega) = \frac{\hbar\pi}{16}\sum_{\lambda'\lambda''}\left|\Phi_{\lambda\lambda'\lambda''}\right|^2 \left\{(n_{\lambda'} + n_{\lambda''} + 1)\delta(\Omega - \omega_{\lambda'} - \omega_{\lambda''})\right\} \\ + (n_{\lambda'} - n_{\lambda''})\left[\delta(\Omega - \omega_{\lambda'} + \omega_{\lambda''}) - \delta(\Omega + \omega_{\lambda'} - \omega_{\lambda''})\right].\end{aligned} \tag{4.2}$$

In this equation, we sum over all of the interactions specified with λ, $\lambda^{'}$, and $\lambda^{''}$. The variables n_λ, $n_{\lambda'}$, $n_{\lambda''}$ are the Bose-Einstein thermal occupancy factors for each of the phonon processes denoted by the subscript. In a perturbative approach, the three-phonon matrix element, $\Phi_{\lambda\lambda'\lambda''}$, is [12]:

$$\Phi_{\lambda\lambda'\lambda''} = \sum_{ijk}\sum_{\alpha\beta\gamma}\frac{\epsilon_\lambda^{i\alpha}\epsilon_{\lambda'}^{j\beta}\epsilon_{\lambda''}^{k\gamma}}{\sqrt{m_i m_j m_k}\sqrt{\omega_\lambda\omega_{\lambda'}\omega_{\lambda''}}}\phi_{ijk}^{\alpha\beta\gamma}e^{i\mathbf{q}\cdot\mathbf{r_i}+i\mathbf{q}\cdot\mathbf{r_j}+i\mathbf{q}\cdot\mathbf{r_k}}. \tag{4.3}$$

In the above equation, m is the mass, and ω is a frequency eigenvalue of the dynamical matrix.

This study uses the previous equations in our phonon spectra calculations performed at nonzero temperature with sTDEP. sTDEP produces the observed noise at lower energy values ($<$ 40 meV). However, at higher temperatures, sTDEP predicts sharp, low-energy acoustic modes not seen in the experiment.

While the discrepancies appear to contraindicate sTDEP for examining these effects, sTDEP results compared with other computational results provide insight into the underlying microscopic mechanisms of the DII. For example, machine-learned interatomic potentials (MLIP) calculations do not fully show the DII. However, the MLIP calculations display more diffuse intensity than sTDEP calculations.

Cuprite (Cu_2O) is an extreme case of a material exhibiting DII, much like the overt presentation of ILMs and intermodulation sidebands in alkali halide compounds. Though not explicitly referenced, past experimental work on Ag_2O shows evidence of DII in the phonon DOS [13]. The feature is evident in the center portion of the DOS as a solid background contribution. The prevalence of DII in Ag_2O is unsurprising due to the similarities between cuprite and Ag_2O. They are both Pn$\bar{3}$m structures and demonstrate high-symmetry bonding behavior with a distinct M-O-M (M=Cu, Ag) bond. Likewise, copper and silver are predominantly coherent scatterers of neutrons of comparable magnitude.

When Cu or Ag bond to oxygen, the resulting oxide is mainly coherent, making it suitable for neutron scattering. Moreover, the mass difference between the Ag/Cu and oxygen delineates the partial DOS contribution. Ag/Cu dominates the DOS below ~40 meV, and oxygen modes dominate above 40 meV.

While we cannot say that any of the neutronic properties of cuprite and Ag_2O mentioned above are the origin of the DII, it does not preclude them. We believe that DII is probably a ubiquitous feature but challenging to resolve with experiments and computations for many materials where the DII is less prominent. There is no mention of a DII-type artifact in the scientific literature. Therefore, we surmise that it was summarily dismissed as poor counting statistics, noise from instrumentation, or a multiphonon effect when it appeared in experiments.

Computational Background

In lattice dynamics calculations, like sTDEP, we use random or stochastic processes to describe the behavior of AH systems at nonzero temperatures. While many use the terms random and stochastic interchangeably, there is a clear distinction. Stochastic processes are random processes, but not all random processes are stochastic. The origin of the word stochastic as we use it today is from the Greek word meaning "guess" or "conjecture." In essence, we use stochastic methods to approximate randomness.

For example, in sTDEP we generate stochastic atomic positions consistent with a Gaussian distribution, u_i, and velocities, $\dot{u}_i$:

$$\begin{aligned} u_i &= \sum_{s=1}^{3N_a} \epsilon_{is} \langle A_{is} \rangle \sqrt{-2\ln \xi_1} \sin 2\pi\xi_2 \\ \dot{u}_i &= \sum_{s=1}^{3N_a} \epsilon_{is} \langle A_{is} \rangle \sqrt{-2\ln \xi_1} \cos 2\pi\xi_2. \end{aligned} \tag{4.4}$$

In the above equation, ξ is a randomly sampled variable ranging from 0 to 1. This variable takes the familiar form of the Box-Mueller transformation [14]. When constructing AH models, we rely on stochastic models in spatial and time coordinates.

The Physics of Noise

We often associate the word noise with music or audio. However, any system that produces a stochastic or random process is capable of generating noise. For example, the average human can hear frequencies within the finite range of 20 to

20,000 Hz. Still, so much more noise around us in our day-to-day lives falls outside the scope that we process as sound. Phonons are a great example of this. The typical frequency of phonons is on the order of terahertz (10^{12}).

While the standard definition of noise carries the connotation that it is unwanted or destructive to pure signal, noise can provide important information about what is happening in a dynamic system. In signal processing and analog electronics, noise gives us information about the source and the underlying mechanisms that drive the system. We can look at phonons the same way. If we can classify the noise present in phonon spectra, we can learn new information about fundamental phonon interactions.

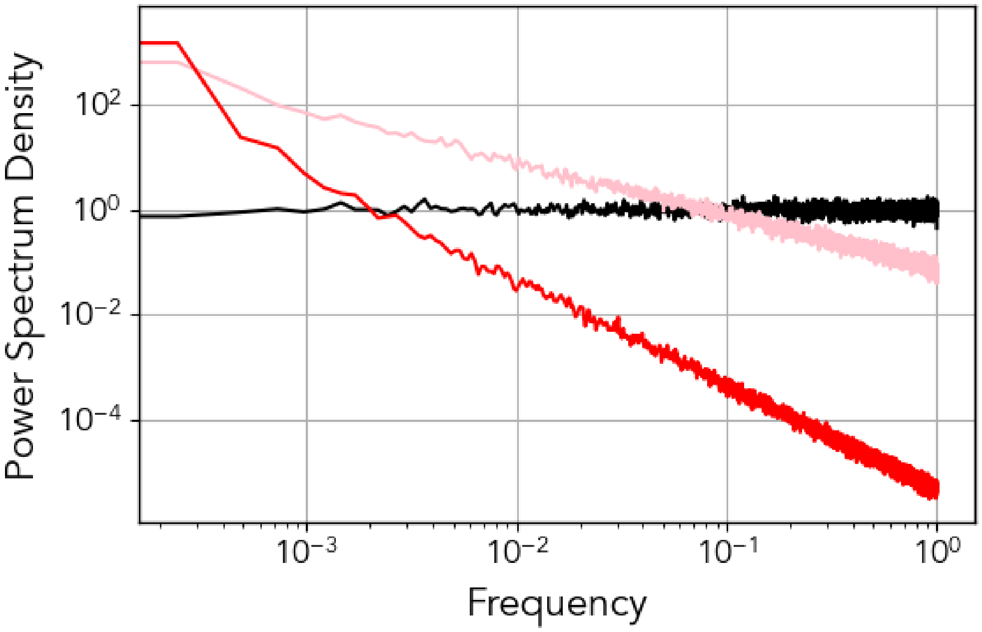

Figure 4.1: Log-log spectra for 1/**f** noise. White noise is shown with the black lines, pink noise is shown in pink, and red or Brownian noise is shown in red.

We categorize noise as a particular color or spectrum. The color stems from a stochastic process and produces a distinct frequency output and power spectrum density. The predominant colors used to classify noise are white, pink, red (Brownian), violet, and grey. There are other noise classifications, including 1/**f** noise, which appears in many systems throughout nature. Fig. 4.1 shows pink, Brownian, and white noise on a log-log plot. The defining feature for each type of 1/**f** noise on the plot is how each changes with increasing frequency.

1/**f** noise has a frequency spectrum with a spectral power density that is inversely proportional to the frequency. The general form of the spectral power density is:

$$S(\mathbf{f}^{\kappa}) \propto \frac{1}{\mathbf{f}^{\kappa}}. \tag{4.5}$$

In this equation, **f** is the frequency. The exponent, κ, ranges from 0 to 2. The value of κ sets the color of noise. While it can take on a non-integer value, the noise shown in Fig. 4.1 shows the noise spectrum for each integer values for κ. We focus on $\kappa = 2$, the condition for Brownian motion, in this chapter.

Brownian motion was first observed in the early 1800s by the botanist Robert Brown [15]. Also referred to as pedesis, derived from the Greek word for leaping, Brownian motion refers to the random motion of small, fast-moving particles suspended in a medium. While it was first seen by Brown looking through a microscope at plant pollen suspended in water, it exists throughout nature. Albert Einstein developed its application to atomic motion in materials. His doctoral thesis developed many of the concepts we use today for looking at Brownian motion in statistical mechanics [16].

Brownian motion is a Wiener process. The Wiener process provides mathematical tools to describe Brownian motion and other continuous time-dependent random processes. In the system we describe in this chapter, we look at how particles' random motion can result in noise in a power spectrum. We use the Wiener–Khinchin theorem, which allows us to relate the random time-dependent motion to a power spectrum.

The following text presents several models to describe the origin of the DII. The first model addresses the incoherent approximation in data reduction. The second model shows how discontinuities in impulses can generate diffuse spectra. The next model looks at the role of higher-order AH contributions, followed by a brief section on AH interference. We also present a model derived from the van Hove function. Lastly, we offer a model incorporating quantum dissipation theory which models oxygen atoms as Brownian particles contained in an AH reservoir of Cu atoms.

4.2 Methods and Tools

This analysis uses similar experimental and computational tools as the previous chapter. While we describe the general procedure for this section, we refer the reader to Chapter 3 for a detailed description.

Experiment

INS measurements used ARCS to perform measurements on a single-crystal of cuprite (see Chapter 3 Section 3.2) at 700 K and 900 K. For both measurements, we mounted the crystal in a low-background electrical resistance vacuum furnace [17]. There were 200 angles in increments of 0.5 °taken at 700 K and 900 K. The incident energy for all single-crystal measurements was 110 meV. An oscillating radial collimator suppressed multiple scattering and background. Similar to the data measured at 10 K and 300 K, the data were reduced in Mantid to obtain the four-dimensional $S(\mathbf{Q},\varepsilon)$. Appendixes D and E contain full detail on the data reduction.

Computation

To calculate the lattice dynamics, we used the Vienna Ab initio Simulation Package (VASP) and the Large-scale Atomic/Molecular Massively Parallel Simulator (LAMMPS) [18]. Additionally, the LAMMPS plugin Machine-Learning (ML) Interatomic Potential (MLIP) package generated interatomic potentials with the Moment Tensor Potential (MTP) method [18, 19].

We trained the ML model and calculated trajectories with Density Functional Theory (DFT) supercell calculations performed with VASP. The DFT calculations used plane-wave basis sets, projector augmented wave (PAW) pseudopotentials, and the generalized gradient approximations (GGA) exchange-correlation functionals [20]. The supercell size was $3 \times 3 \times 3$ containing 162 atoms. The k-grid was $2 \times 2 \times 2$, and the kinetic energy cutoff of 520 eV. There were $\mathrm{N} = 523$ supercell configurations used to train the model. Each supercell had unique atomic displacements generated with sTDEP.

The accuracy of ML algorithms depends heavily on the makeup of the training set. Accuracy is crucial for active learning, where the algorithm makes on-the-fly predictions. Cases that are significantly different from the scope of the training set may require extrapolation rather than interpolation. This can result in significant errors. One method to address this issue is to define extrapolation explicitly. In MLIP, the D-optimality criterion defines extrapolation, which states that a robust training set provides the maximum value of the information matrix determinant. Subsequently, this defines the extrapolation grade, $\gamma(\mathrm{cfg})$, which is comprised of the training set and current configuration and does not require *ab initio* data as an input.

Once training was complete, we performed classical MD simulations with LAMMPS. The LAMMPS plugin Moment Tensor Potential (MTP) method generated interatomic potentials. The supercell size was $30 \times 30 \times 30$ with 162,000 atoms. sTDEP calculations referenced in this chapter use the same procedure described in Section 3.3 of Chapter 3. The computational results from MD calculations were post-processed in the package VVCORE. See Appendix F for a detailed explanation of the calculations and their code implementation.

To generate DII on a more straightforward monatomic system, we performed calculations on face center cubic Cu at 300 K using LAMMPS with MLIP. The training sets consisted of 162 atoms in a 3x3x3 supercell. In these calculations, we work with a modified Morse potential within LAMMPS. The Morse potential is AH and initially developed for diatomic molecules. In this work, we apply it to a monatomic system without loss of accuracy. The functional form is:

$$V_{\mathrm{M}}(r) = D_{\mathrm{e}} \left(1 - e^{-\alpha(r - r_{\mathrm{e}})}\right)^2, \tag{4.6}$$

where $\mathrm{D_e}$ sets the depth and α sets the width of the potential well. For the Morse potential, the value for α is:

$$\alpha = \sqrt{k_e/2D_e}. \tag{4.7}$$

In the above expression, k_e is the force constant at the minimum of the potential well. For our calculations with LAMMPS, we assembled a discontinuous Morse pair potential to simulate the proposed impulse between adjacent atoms. We varied the size of the potential jump with 1, 3, 5, 10 eV/Å. We also compared the difference between using a Gaussian function in place of a discontinuity.

4.3 Results

Figure 4.2 shows the phonon dispersion high-symmetry direction along Γ to X for fcc Cu at 300 K for each energy. The panels show the phonon dispersion corresponding to an increase in the jump size. We see that with an increase in the jump size, there is an increase in the noise.

Figure 4.3 shows spatial slices at the center point between the high-symmetry direction Γ and X for fcc Cu at 300 K as a function of energy. Each line color shows a different value of the potential jump (0-10 eV/Å). With an increase in the jump size, there is an increase in the noise trending towards high energy.

Figure 4.4 shows the interatomic force in the copper system. Each color shows a different jump size ranging from 0 to 10 eV/Å. Figure 4.5 shows a zoomed-in

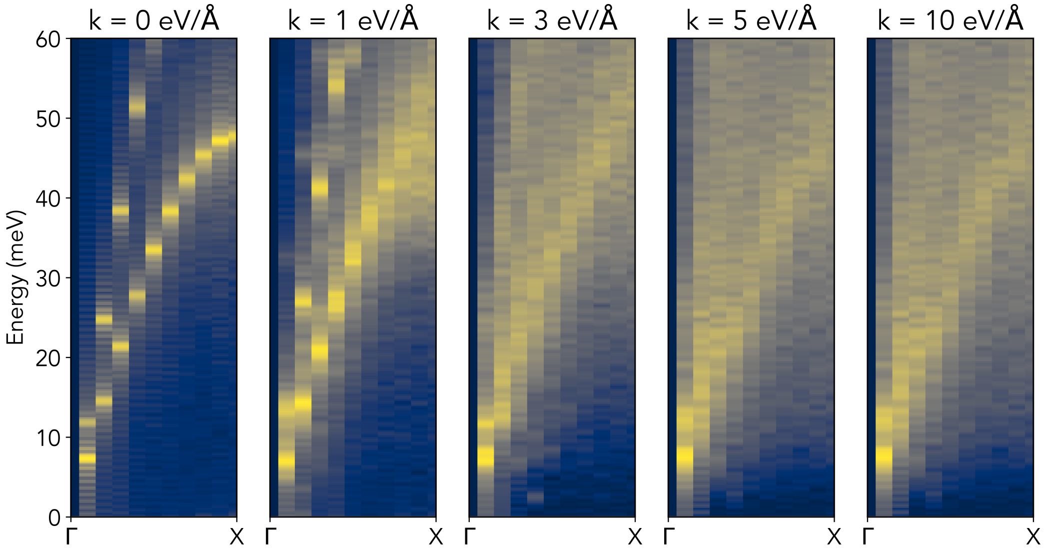

Figure 4.2: Data for fcc Cu simulated at 300 K along the high-symmetry direction, Γ to X, with respect to energy. Each panel corresponds to a different value of k, the magnitude of the atom jumps.

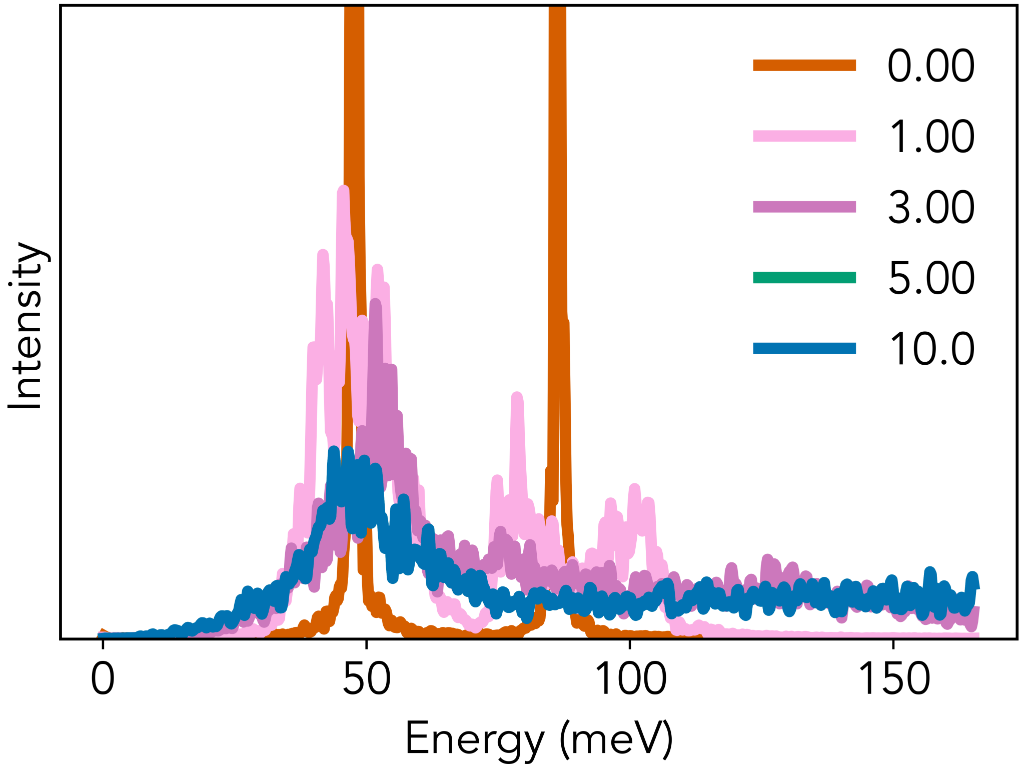

Figure 4.3: Data cut between Γ and X for fcc Cu at 300 K with respect to energy. Each line is for a different value of k, the magnitude of the atom jump.

version of Fig. 4.4. Figure 4.6 shows the discontinuity introduced into the force constant.

Figures 4.7 and 4.8 show processed phonon spectra at 700 K and 900 K from INS measurements along high-symmetry crystallographic directions. For both temperatures, the only discernible details are the low-energy acoustic modes. The DII dominates the remainder of the spectra.

Figure 4.13 shows phonon spectra from INS measurements and AH calculations along high-symmetry crystallographic directions. Figure 4.13 a) and c) show the folded experimental data from the single-crystal at 700 and 900 K, respectively, and Fig. 4.13 c) and d) show the corresponding AH MLIP calculations. The main features and energies of the calculated and measured intensities agree. The calculated high-energy optical modes show a broadening and softening. Due to the degree of broadening in the experimental measurements, it is not easy to ascertain whether the softening is consistent with the experiment. Below 45 meV, there is inconsistency in the low-energy optical modes. While calculations yield a diffuse signal, the optical modes maintain their features. In the experimental results, the optical modes are entirely diffuse.

Figure 4.14a)-d) shows sTDEP calculations for a) 10 K, b) 150 K, c) 300 K, and d) 550 K. These temperature results show the softening of the optical modes as the temperature increases. Approaching 550 K, the DII increases in intensity as the low energy optical modes from 20 meV to 40 meV soften. The DII is most visible from the high-symmetry points X to M. While there is visible temperature-dependent broadening of the high energy optical modes, this is not the case for the modes below 40 meV.

4.4 Discussion

Overall, MLIP calculations better account for the experimentally measured behavior at 700 K (Fig. 4.7) and 900 K (Fig. 4.8). All calculations do not account for what we observe experimentally fully. One approach to understanding what is happening in this system is to investigate experimental components that we have not accounted for in our calculations that would make the collected dispersions more diffuse than they ought to be.

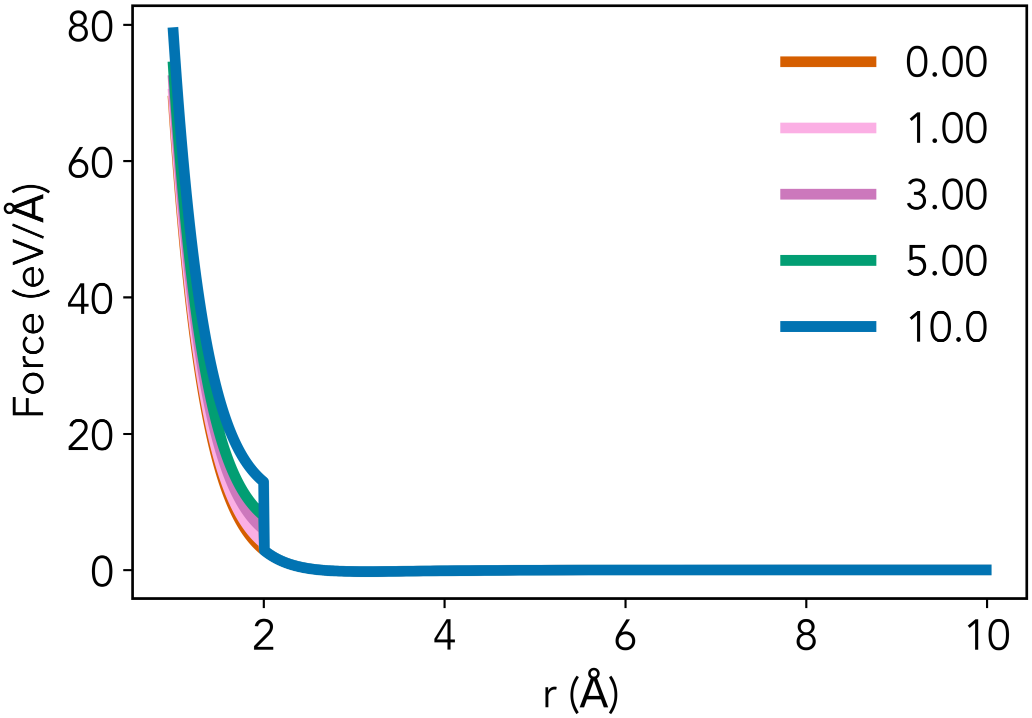

Figure 4.4: The interatomic forces in the copper system. The magnitude of the jump in the force is shown by the color of the line.

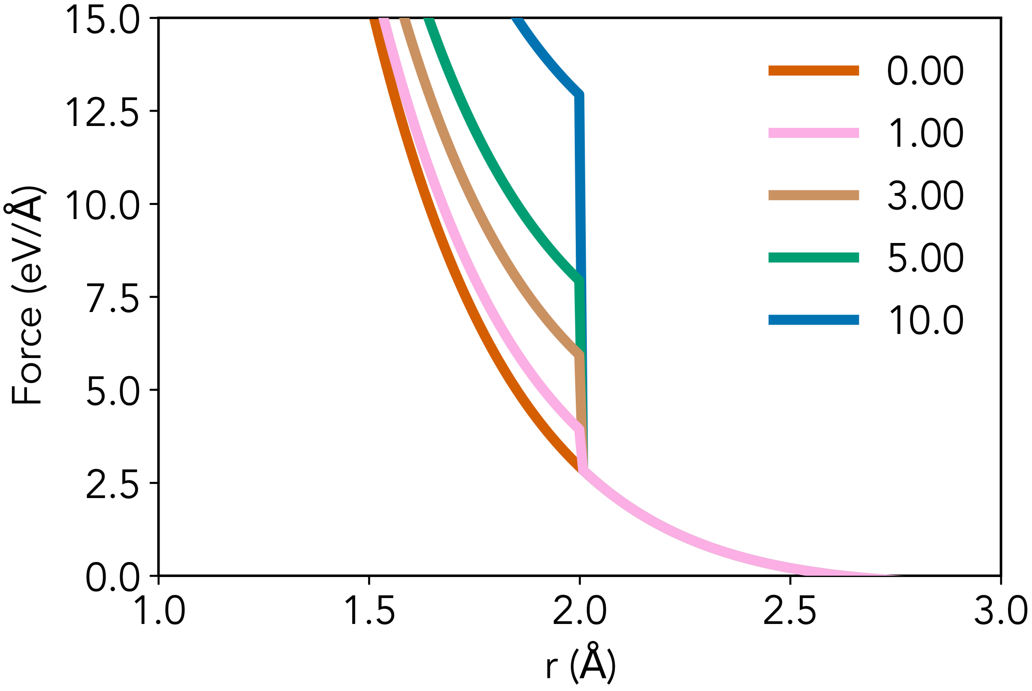

Figure 4.5: Expanded region of Fig. 4.4. The magnitude of the jump in the force is shown by the color of the line.

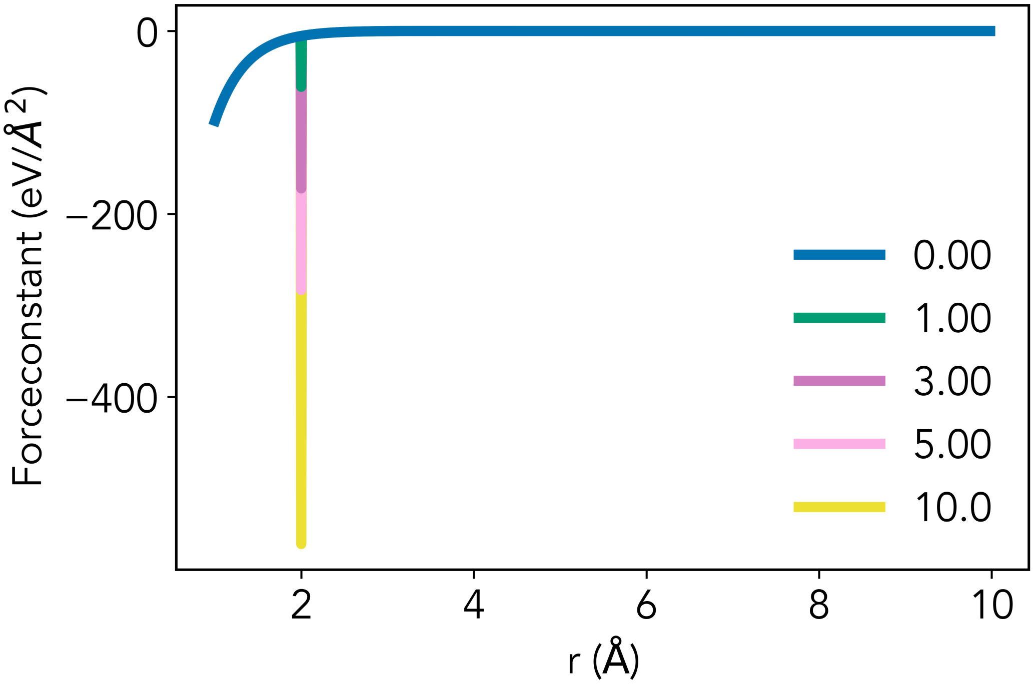

Figure 4.6: The nearest neighbor forceconstants in the copper system. The magnitude of the jump in the force is shown by the color of the line.

Contributions of Phonon Dissipation Through Friction

This section expresses the DII in its contribution to the total scattering power spectrum, $S(\omega)$. The origin of this spectral contribution is from phonon friction energy dissipation. Internal instabilities from phonon-phonon coupling and finite phonon lifetimes are redistributed over the entire phonon spectrum [21]. Derivations of the generalized quantum Langevin equation can generate dissipative friction forces in dynamic systems of non-interacting phonon modes while never reaching thermalization.

Cuprite has a distinct linear O-Cu-O bond. This linear bonding with the negative thermal expansion (NTE) below room temperature prompted an investigation into the presence of rigid unit modes (RUMs) in cuprite [22]. However, later experiments investigating the same thermal expansion behavior showed that the tetrahedral unit (OCu_4) in cuprite was not rigid [23].

Our own examination of the individual AH configurations used in Chapter 3 shows that the local tetrahedral unit becomes largely distorted at elevated temperatures. Furthermore, the displacements of O atoms dominate the optical modes above 60 meV. The relative flatness of the modes is typical of isotropic vibrations of individual O-atoms. This study concluded that the ionic bonding in cuprite includes weak intranetwork interactions between Cu atom correlations and cuprophilic O atom interactions which become increasingly dominant with higher temperatures.

While we know that a rigid model does not accurately describe the dynamics of cuprite, the intranetwork interactions do allow some rigidity like frictional dissipation through the movement of Cu atoms over a plane of the O atoms. Further, this frictional interaction is necessary if we assume a closed quantum system.

In what follows, we derive an expression for the total scattering power spectrum of Brownian-like harmonic oscillators, Cu atoms, coupled to an AH reservoir of O atoms. We use a modified version of the Caldeira-Leggett (CL) model where we have a nonlinear system weakly coupled to a reservoir [24]. This range requires quantum operators to at least second-order. In solid-state quantum optics, the contribution of the weak nonlinear regime to the total spectrum is negligible; however, it may contribute more in other domains like Raman spectroscopy and inelastic neutron scattering (INS).

When examining phonon behavior in materials, one typically assumes a system in equilibrium. However, in our weakly coupled nonlinear system, we do not assume thermalization, also called thermal equilibrium, due to phonon dissipation in friction-like interaction.

Recent studies on intrinsic localized modes and intermodulation phonon sidebands in alkali halides strongly suggest that there is internal phonon coupling in the system that arises from nonlinear many-body effects [1]. The authors present a final symmetrized power spectral density that obeys detailed balance when in thermal equilibrium. However, thermal equilibrium is not experimentally or computationally confirmed.

Detailed balance states that elementary processes, like the collision of a neutron with atomic nuclei, must be in equilibrium with the reverse process [25]. For the four-dimensional neutron scattering function, $S(\omega)$, this means

$$S(-\omega) = \exp\left[-\frac{\omega}{k_\mathrm{B}T}\right] S(\omega). \tag{4.8}$$

In Eq. (4.8), ω, k_B, and T are the frequency of oscillation, Boltzmann's constant, and temperature.

In grossly equivalent optical systems, there exists a phenomenon known as sideband inequivalence [26]. Side-band inequivalence is not possible in the presence of strong coupling. It has a short lifetime in highly nonlinear systems. Moreover, it is forbidden in linear systems, making it challenging to observe experimentally.

We proposed that the motion of the Cu atoms in cuprite is Brownian-like. While Brownian systems are one of the most commonly used examples of Markovian systems, we do not assume a Markovian setup. This assumption means that the system has a memory of prior states. Further, we assume a system with phonon dissipation from friction interactions and infer locally broken detailed balance. Locally broken detailed balance does not necessarily mean that detailed balance in the entire setup is broken, but rather broken local contributions. The last assumption is that an outside force does not externally drive our system.

The Hamiltonian of the system and bath is

$$\begin{aligned}\hat{H} = \hbar\omega_0 \hat{a}^\dagger(t)\hat{a}(t) + \sum_k \left[\hbar\omega_k \hat{b}_k^\dagger(t)\hat{b}_k(t) + \left(\hat{b}_k^\dagger(t) + \hat{b}_k(t)\right)^3\right] \\ + \sum_k \hbar\left(V_k \hat{a}^\dagger(t)\hat{b}_k(t) + V_k^* \hat{a}(t)\hat{b}_k^\dagger(t)\right)\end{aligned} \tag{4.9}$$

where $\hat{a}^\dagger(t)$, $\hat{a}(t)$, $\hat{b}_k^\dagger(t)$, $\hat{b}_k(t)$ are time-dependent creation and annihilation operators of the harmonic oscillator system with resonant frequency ω_0 and of the reservoir with frequency ω_k, respectively. The variables V_k and V_k^* are the phonon scattering amplitudes between a O atom of index k and a Cu atom. The creation and annihilation must obey the commutation relationships [27]

$$[a(t), a^\dagger(t)] = \delta \qquad [b_j(t), b_{j'}^\dagger(t)] = \delta_{jj'} \tag{4.10}$$

and

$$[a(t), b_k^\dagger(t)] = [b_j(t), b_k^\dagger(t)] = [a(t), b_i^\dagger(t)] = [a^\dagger(t), b_j^\dagger(t)] = 0. \tag{4.11}$$

where $\delta_{jj'}$ is the Dirac delta function. The remaining variables in Eq. (4.10) and (4.11).

We can write Eq. (4.9) in terms of the composite Hamiltonians

$$\hat{H} = \hat{H}_S + \hat{H}_R + \hat{H}_I. \tag{4.12}$$

In Eq. 4.12, $\hat{H}_S$ is the Hamiltonian of the system harmonic oscillator

$$\hat{H}_S = \hbar\omega_0 \hat{a}^\dagger(t)\hat{a}(t). \tag{4.13}$$

$\hat{H}_R$ is the Hamiltonian of the AH reservoir

$$\hat{H}_R = \sum_k \left[\hbar\omega_k \hat{b}^\dagger(t)\hat{b}(t) + \left(\hat{b}^\dagger(t) + \hat{b}(t)\right)^3\right]. \tag{4.14}$$

The remaining composite Hamiltonian expression is the interaction term is $\hat{H}_I$

$$\hat{H}_I = \sum_k \hbar\left(V_k \hat{a}^\dagger(t)\hat{b}_k(t) + V_k^* \hat{a}(t)\hat{b}_k^\dagger(t)\right). \tag{4.15}$$

Caldierra and Leggett construct the master equation in terms of the quantum reduced density operator [28]

$$\begin{aligned}\frac{d\hat{\rho}(t)}{dt} =& -i\omega_0'(t)\left[\hat{a}^\dagger(t)\hat{a}(t), \hat{\rho(t)}\right] \\ &+\gamma_1(t)\left[2a(t)\rho(t)\hat{a}^\dagger(t) - \hat{a}^\dagger(t)\hat{a}(t)\rho(t) - \rho(t)\hat{a}^\dagger(t)\hat{a}(t)\right] \\ &+\gamma_2(t)\left[\hat{a}(t)\rho(t)\hat{a}^\dagger(t) + \hat{a}^\dagger\rho(t)\hat{a}(t) - \hat{a}^\dagger(t)\hat{a}(t)\rho(t) - \rho(t)a(t)a^\dagger(t)\right].\end{aligned} \tag{4.16}$$

In Eq. (4.16), ω_0' is a renormalized frequency of the time-dependent Einstein oscillator. $\gamma_1(t)$ and $\gamma_2(t)$ are the phonon dissipation an fluctuation (noise) respectively.

We obtain ρ by taking the trace of the degrees of freedom of the entire system an reservoir such that $\rho(t) = Tr[\rho_{tot}(t)]$, where $\rho_{tot}(t) = e^{-\frac{i}{\hbar}\hat{H}(t-t_0)}\rho(t_0)e^{\frac{i}{\hbar}\hat{H}(t-t_0)}$ [29, 30]. This allows the separation into a time evolution component multiplied by the initial state of the system at an arbitrary initial time t_0. We can then write the initial state of the total system as a product of an initial state of the system multiplied by the thermal state of the reservoir, $\rho_{tot}(t_0) = \rho(t_0) \bigotimes \rho_R(t_0)$, where $\rho_R(t_0) = \exp\left[-\beta\hat{H}_R\right]/Tr\left[\exp\left(-\beta\hat{H}_R\right)\right]$.

Previous calculations [31] show the following

$$\omega_0' = -Im\left[\frac{\dot{u}(t)}{u(t)}\right], \tag{4.17}$$

$$\gamma_1(t) = -Re\left[\frac{\dot{u}(t)}{u(t)}\right], \tag{4.18}$$

and

$$\gamma_2(t) = \dot{v(t)} - 2v(t)Re\left[\frac{\dot{u}(t)}{u(t)}\right]. \tag{4.19}$$

In the above equations, $u(t)$ is a non-equilibrium spectral Green's function which satisfies the Schwinger-Dyson equation of motion,

$$\dot{u}(t) + i\omega_0' u(t) + \int_{t_0}^{t} d\tau g(t-\tau)u(t) = 0, \tag{4.20}$$

with the initial condition $u(t_0) = 1$. Using the non-equilibrium fluctuation dissipation theorem for the correlation function,

$$v(t) = \int_{t_0}^{t} d\tau \int_{t_0}^{t} d\tau' g_2(\tau - \tau' u^*(\tau) u(\tau'), \tag{4.21}$$

where g_1 and g_2 are time correlation functions,

$$g_1(t-\tau) = \int_0^\infty \frac{d\omega}{2\pi} J(\omega) \exp\left[-i\omega(t-\tau)\right] \tag{4.22}$$

and

$$g_2(t-\tau) = \int_0^\infty \frac{d\omega}{2\pi} J(\omega) n(\omega, T) \exp\left[-i\omega(t-\tau)\right]. \tag{4.23}$$

The above equations for g_1 and g_2 contain the information necessary to describe the non-Markovian memory effects of the system. $n(\omega, T)$ is the Planck occupancy factor. The expression for the spectral density is

$$J(\omega) = 2\pi \sum_k \left|V_k\right|^2 \delta(\omega - \omega_k). \tag{4.24}$$

If we assume a continuous spectral density, the expression becomes

$$J(\omega) = 2\pi v(\omega) \left|V_k\right|^2, \tag{4.25}$$

where $v(\omega)$ is the density of final states of the reservoir.

If we want to obtain the quantum noise of our system, we need to take the autocorrelation

$$S(\omega) = \lim_{t\to\infty} \int_{-\infty}^{\infty} e^{i\omega\tau} \left\langle a'(t+\tau) a(t) \right\rangle d\tau. \tag{4.26}$$

It has been shown [27] that in the master equation we have the relationship,

$$\left\langle a'(t+\tau) a(t) \right\rangle = u'(t+\tau) u(t) \left\langle a'(t_0) a(t_0) \right\rangle + v(t, t+\tau), \tag{4.27}$$

where we use the more general form of Eq. (4.21),

$$v(t, t+\tau) = \int_{t_0}^{t} d\tau_1 \int_{t_0}^{t+\tau} d\tau_2 u(t, \tau_2) g_2(\tau_1, \tau_2) u^*(t+\tau, \tau_2). \tag{4.28}$$

We use the exact form of the spectral Green's function,

$$u(t) = \mathcal{Z} e^{-i\omega_b(t-t_0)} + \frac{1}{\pi} \int_0^\infty \frac{\gamma_1(\omega) e^{-i\omega(t-t_0)}}{\left[\omega - \omega_0 - \Delta(\omega)\right]^2 + \gamma_1^2(\omega)} d\omega. \tag{4.29}$$

In the above expression, we have the real correction to the self-energy $\gamma_1(\omega) = J(\omega)/2$ and the imaginary correction (Kramer's Kronig relation),

$$\Delta(\omega) = \mathcal{P}\int_0^\infty \frac{J(\omega')}{\omega - \omega'} d\omega'. \tag{4.30}$$

In Eq. (4.29), the term $\mathcal{Z}$ is the energy correction from the coupling between the Einstein oscillators and the reservoir. It is expressed as

$$\mathcal{Z} = \frac{1}{(1 - \Sigma'(\omega_b))^2}, \tag{4.31}$$

where $\omega_b = \omega_0 + \delta(\omega_b)$. The above expression relates the residue of $\Sigma(z)$ at the pole when $z = \omega_b$.

Using the above equations, we solve for the noise contribution to the spectrum

$$\begin{aligned} S(\omega) &= \lim_{t\to\infty}\int_{-\infty}^{\infty} e^{i\omega\tau}\langle a'(t+\tau)a(t)\rangle \, d\tau \\ &= \lim_{t\to\infty}\int_{-\infty}^{\infty} \left[e^{i\omega\tau}u'(t+\tau)u(t)\langle a'(t_0)a(t_0)\rangle + v(t, t+\tau)\right] d\tau, \end{aligned} \tag{4.32}$$

where we get

$$\begin{aligned} S(\omega) =& \mathcal{Z}^2\delta(\omega - \omega_b)\langle a'(t+\tau)a(t)\rangle \\ &+ \left[\frac{\mathcal{Z}^2 J(\omega)n(\omega, T)}{(\omega - \omega_b)^2} + \frac{J(\omega)n(\omega, T)}{[\omega - \omega_0 - \Delta(\omega)]^2 + \gamma_1(\omega)^2}\right] \\ =& S_1(\omega) + S_2(\omega). \end{aligned} \tag{4.33}$$

$S_1(\omega)$ and $S_2(\omega)$ are the correlation term contributions from the system (S_1) and reservoir (S_2) to the noise spectrum due to the coupling.

We perform a power series expansion on S_1 giving us

$$\begin{aligned} S_2(\omega) =& \frac{\mathcal{Z}^2 J(\omega)n(\omega, T)}{(\omega - \omega_b)^2} + \frac{J(\omega)n(\omega, T)}{\omega_0^2\gamma_1^2(\omega)}\left(\sum_{n=0} P_n(x)xy^n\right)^2 \\ =& \frac{\mathcal{Z}^2 J(\omega)n(\omega, T)}{(\omega - \omega_b)^2} + \frac{J(\omega)n(\omega, T)}{\omega_0^2\gamma_1^2(\omega)}\left[1 + 2xy + O(x^2y^2) + \ldots\right] \end{aligned} \tag{4.34}$$

where $x = \omega_0/\sqrt{\omega_0^2 + \gamma_1^2(\omega)}$ and $y = (\omega - \delta(\omega)/\sqrt{\omega_0^2 + \gamma_1^2(\omega)})$. In our experimental results, the greatest noise appears in the low-frequency limits where $\hbar\omega/k_BT << 1$ and $\omega_0 << \omega_0$. In this limit, the expression becomes

$$S(\omega) = \frac{\eta' k_B T}{\omega^{1-s}} = \frac{\mu k_B T}{\omega^\kappa} \tag{4.35}$$

where $\eta' = \eta\omega_c^{1-s}/\hbar\omega_0^2$.

While this model clearly produces the observed $1/\mathbf{f}$ noise, we later address limitations on the value of κ in Eq. (4.35). Previous studies on decoherence dynamics of $1/\mathbf{f}$ noise [32] have plots comparing different values in Eqs. (4.35), (4.34), and (4.33). We refer the reader to these plots.

Aside from cuprite, a similar self-interacting weakly correlated network is $CsPbBr_3$ which looks at the AH behavior as a phonon gas and rattling motions of Cs^+ cations. Investigating materials with cage-like structures with some rigidity and significant mass discrepancies between atomic constituents might prove valuable for further experimental validation of the DII.

Modeling Brownian Motion in an Anharmonic Reservoir with Perturbation Theory

In the previous section on phonon dissipation, we presented a non-Markovian model which produces $1/\mathbf{f}$ noise in the low frequency. Here we consider the other case of Markovian Brownian motion. Cu atoms exhibit Brownian motion in an AH field or medium from nearby O atoms in this setup. We model the behavior of this setup using a purely AH double-well potential. Prior studies have shown the efficacy of modeling phononic behavior using a double-well potential [33]. This AH potential has a similar form to a Landau potential for a second-order transition [34]. We show that the correlated Brownian motion of Cu atoms in an AH O field produces a diffuse intensity in the power spectrum. The work in this section draws from previous theoretical studies on classical dynamics correlations between harmonic Brownian particles subject to a purely AH field [35].

We use the time-dependent spatial variable $\mathbf{q}_s(t)$, for the system of Cu-atoms and $\mathbf{q}_{r,\lambda}(t)$, for the reservoir of O-atoms. Further differences are in subscripts of the variables.

The total Hamiltonian follows the expression:

$$\hat{H} = \hat{H}_S + \hat{H}_R + \hat{H}_I + \hat{H}_C. \tag{4.36}$$

In the equation for $\hat{H}$, the first term, $\hat{H}_S$, is a Hamiltonian that describes the system of Cu-atoms. The Cu-atoms act as Einstein oscillators, each vibrating at a frequency of ω_s. As a result, the Hamiltonian is the same as one for a simple quantum harmonic oscillator:

$$\hat{H}_S = \frac{\mathbf{p}_s(t)^2}{2M_s} + U_s(\mathbf{q}_s(t)). \tag{4.37}$$

For now, we express the potential simply as $U_S(\mathbf{q}_s(t))$. The other variables are the momentum, $\mathbf{p}_s(t)$, for a single oscillator with mass, M_s.

The second term in Eq. (4.36) is the Hamiltonian for the AH reservoir of O-atoms, $\hat{H}_R$. For this Hamiltonian, we will use the following AH expression

$$\begin{aligned}\hat{H}_R = \sum_{\lambda} \Bigg[&\left(\frac{\mathbf{p}_{r,\lambda}(t)^2}{2M_{r,\lambda}} + \frac{1}{2} M_{r,\lambda} \omega_{r,\lambda}^2 \mathbf{q}_{r,\lambda}(t)^2 \right) \\ &+ \gamma \left(U_{r,\lambda}(\mathbf{q}_{r,\lambda}(t)) - \frac{1}{2} M_{r,\lambda} \omega_{r,\lambda}^2 \mathbf{q}_{\mathbf{r},\lambda}(t)^2 \right) \Bigg].\end{aligned} \tag{4.38}$$

In this expression, the subscript r denotes a variable of the reservoir. This expression sums over λ AH oscillators in the reservoir each with mass, $M_{R,\lambda}$, and frequency, $\omega_{r,\lambda}$. For adjusting the strength of a perturbation, we include γ. Note that Eq. (4.38) recovers the equation for the simple harmonic oscillator when $\gamma = 0$.

We model the AH potential from the standard equation for a double-well oscillator, $U(q) = -\alpha q^2 + \beta q^4$, and use the following expression for the AH potential:

$$U_{r,\lambda}(\mathbf{q}_{r,\lambda}(t)) = \frac{\alpha_\lambda^2}{2\beta_\lambda} - \alpha_\lambda \left(\mathbf{q}_{r,\lambda}(t) - \sqrt{\frac{\alpha_\lambda}{2\beta_\lambda}} \right)^2 + \beta_\lambda \left(\mathbf{q}_{r,\lambda}(t) - \sqrt{\frac{\alpha_\lambda}{2\beta_\lambda}} \right)^4. \tag{4.39}$$

In the above expression, α_λ and β_λ are positive constants. The $\sqrt{\frac{\alpha_\lambda}{2\beta_\lambda}}$ term sets the origin of the AH potential to the minimum of the left well.

In Eq. (4.36), the next component is a correlation term between the system and the reservoir. For this calculation we assume the coupling is linear in both reference frames. This term must include both $\mathbf{q}_s(t)$ and $\mathbf{q}_{r,\lambda}(t)$:

$$\hat{H}_I = \rho C_{r,\lambda} \mathbf{q}_s(t) \mathbf{q}_\lambda(t). \tag{4.40}$$

In the coupling Hamiltonian, ρ is a sufficiently small scaling prefactor that we will use for our perturbative approach. $C_{r,\lambda}$ is a coupling constant between the harmonic system and the λ-th oscillator in the AH reservoir. The final two terms, $\mathbf{q}_s(t)$ and $\mathbf{q}_{r,\lambda}(t)$ are linear position functions in the system and reservoir reference frames specified by the subscript.

The final term in our general Hamiltonian is $\hat{H}_C$. This term is often called a counter term. The counter term ensures that the reservoir does not directly modify the harmonic potential system. We write it as a second-order perturbation expansion term of the coupling Hamiltonian:

$$\hat{H}_C = -\rho^2 \frac{C_{r,\lambda}^2}{2M_{r,\lambda}\omega_{r,\lambda}^2}\mathbf{q}_s(t)^2. \tag{4.41}$$

Summing the components, the full Hamiltonian becomes

$$\begin{aligned}
\hat{H} =& \hat{H}_S + \hat{H}_R + \hat{H}_I + \hat{H}_C \\
=& \frac{\mathbf{p}_s(t)^2}{2M_s} + U_s(\mathbf{q}_s(t)) \\
&+ \sum_\lambda \Bigg[\left(\frac{\mathbf{p}_{r,\lambda}(t)^2}{2M_{r,\lambda}} + \frac{1}{2}M_{r,\lambda}\omega_{r,\lambda}^2\mathbf{q}_{r,\lambda}(t)^2 \right) \\
&+ \gamma \left(U_{r,\lambda}(\mathbf{q}_{r,\lambda}(t)) - \frac{1}{2}M_{r,\lambda}\omega_{r,\lambda}^2\mathbf{q}_{r,\lambda}(t)^2 \right) \\
&+ \rho C_{r,\lambda}\mathbf{q}_s(t)\mathbf{q}_{r,\lambda}(t) - \rho^2 \frac{C_{r,\lambda}^2}{2M_{r,\lambda}\omega_{r,\lambda}^2}\mathbf{q}_s(t)^2 \Bigg].
\end{aligned} \tag{4.42}$$

With the full Hamiltonian in phase space coordinates, we use Hamilton's equations for $\mathbf{p}$ and position, $\mathbf{q}$:

$$\frac{d\mathbf{q}}{dt} = \frac{\partial \hat{H}}{\partial \mathbf{p}}, \tag{4.43}$$

$$\frac{d\mathbf{p}}{dt} = -\frac{\partial \hat{H}}{\partial \mathbf{q}}. \tag{4.44}$$

The goal is to obtain the positions in both reference frames, $\mathbf{q}_s(t)$ and $\mathbf{q}_{r,\lambda}(t)$. Starting for the harmonic system:

$$\begin{aligned}
\frac{d\mathbf{p}_s(t)}{dt} &= -\frac{\partial \hat{H}}{\partial \mathbf{q}_s} \\
&= -\frac{\partial U_s(\mathbf{q}_s(t))}{\partial \mathbf{q}_s(t)} - \sum_\lambda \left[\rho C_\lambda \mathbf{q}_{r,\lambda}(t) - \rho^2 \frac{C_{r,\lambda}^2}{M_{r,\lambda}\omega_{r,\lambda}^2}\mathbf{q}_s(t) \right].
\end{aligned} \tag{4.45}$$

The left hand side of the equation can be written as $\frac{d\mathbf{p}_s}{dt} = M_s\frac{d\dot{\mathbf{q}}_s(t)}{dt}$, where the dot specifies a time derivative. We solve for $\mathbf{q}_{r,\lambda}(t)$ to obtain an expression for $\mathbf{q}_s(t)$ that is independent of the spatial coordinates of the reservoir:

$$M_s\ddot{\mathbf{q}}_s(t) + \frac{\partial U_s(\mathbf{q}_s(t))}{\partial \mathbf{q}_\mathbf{s}(\mathbf{t})} = -\sum_\lambda \left[\rho C_{r,\lambda}\mathbf{q}_{r,\lambda}(t) - \rho^2 \frac{C_{r,\lambda}^2}{M_{r,\lambda}\omega_{r,\lambda}^2}\mathbf{q}_s(t) \right]. \tag{4.46}$$

For this, we use a perturbation theory approach:

$$\mathbf{q}_{r,\lambda}(t) = \mathbf{q}_{r,\lambda}^{(0)}(t) + \rho\mathbf{q}_{r,\lambda}^{(1\rho)}(t) + \gamma\mathbf{q}_{r,\lambda}^{(1\gamma)}(t) + \rho\gamma\mathbf{q}_{r,\lambda}^{(\rho\gamma 2)}(t) + \rho^2\mathbf{q}_{r,\lambda}^{(2\rho)}(t) + \gamma^2\mathbf{q}_{r,\lambda}^{(2\gamma)}(t) + \dots \tag{4.47}$$

Due to the relative magnitude of the zeroth and first order terms, we only keep terms up to first order for both ρ and γ:

$$\mathbf{q}_{r,\lambda}(t) = \mathbf{q}^{(0)}_{r,\lambda}(t) + \rho\mathbf{q}^{(1\rho)}_{r,\lambda}(t) + \gamma\mathbf{q}^{(1\gamma)}_{r,\lambda}(t). \tag{4.48}$$

Substituting the above expression into Eq. (4.46):

$$\begin{aligned}\sum_{\lambda} M_{r,\lambda}\ddot{\mathbf{q}}_{r,\lambda}(t) &= -\sum_{\lambda}\left[\gamma\left(\frac{\partial U_{r,\lambda}(\mathbf{q}_{r,\lambda}(t))}{\partial\mathbf{q}_{r,\lambda}(t)} - M_{r,\lambda}\mathbf{q}_{r,\lambda}(t)\right) + \rho C_{r,\lambda}\mathbf{q}_{r,\lambda}(t)\right]\\ &= -\sum_{\lambda}\Big[\gamma\Big(2\alpha_1\mathbf{q}_{r,\lambda}(t) - 3\alpha_2\mathbf{q}^2_{r,\lambda}(t) + 4\alpha_3\mathbf{q}^3_{r,\lambda}(t)\\ &\quad - M_{r,\lambda}\mathbf{q}_{r,\lambda}(t)\Big) + \rho C_{r,\lambda}\mathbf{q}_s(t)\Big]\end{aligned} \tag{4.49}$$

For the zeroth order case ($\gamma = \rho = 0$), we get:

$$\ddot{\mathbf{q}}^{(0)}_{r,\lambda}(t) + \omega^2_{r,\lambda}\mathbf{q}^{(0)}_{r,\lambda}(t) = 0 \tag{4.50}$$

and the following solution:

$$\begin{aligned}\mathbf{q}^{(0)}_{r,\lambda}(t) &= \mathbf{q}_{r,\lambda}(0)\cos\omega_{r,\lambda}t + \frac{\mathbf{p}_{r,\lambda}(0)}{M_{r,\lambda}\omega_{r,\lambda}}\sin\omega_{r,\lambda}t\\ &= \mathbf{q}_{0,r,\lambda}\cos\omega_{r,\lambda}t + \frac{\mathbf{p}_{0,r,\lambda}}{M_{r,\lambda}\omega_{r,\lambda}}\sin\omega_{r,\lambda}t\end{aligned} \tag{4.51}$$

where $\mathbf{q}_{r,\lambda}(t = 0) = \mathbf{q}_{0,r,\lambda}$ and $\mathbf{p}_{r,\lambda}(t = 0) = \mathbf{p}_{0,r,\lambda}$.

Now we want to do the same for the first-order of γ. From this, we obtain the following solution [35]:

$$\begin{aligned}\mathbf{q}^{(1\gamma)}_{r,\lambda}(t) &= K_0 + K_{1s}\sin\omega_{r,\lambda} + K_{1c}\cos\omega_{r,\lambda}\\ &\quad - K_{2s}\sin\omega_{r,\lambda} - K_{2c}\cos\omega_{r,\lambda}\\ &\quad - K_{3s}\sin\omega_{r,\lambda} - K_{3c}\cos\omega_{r,\lambda}\end{aligned} \tag{4.52}$$

The expressions for K are:

$$\begin{aligned}
\omega_{r,\lambda}^2 K_0 =& \frac{3}{M_{r,\lambda}}\sqrt{2\alpha_\lambda\beta_\lambda}\left[Q_\lambda^2 + P_\lambda^2\right] \\
4\omega_{r,\lambda}^2 K_{1s} =& \Omega_\lambda^2 P_\lambda - \frac{3\beta_\lambda}{M_{r,\lambda}}\left[P_\lambda^3 + Q_\lambda^2 P_\lambda\right] \\
4\omega_{r,\lambda}^2 K_{1c} =& \Omega_\lambda^2 Q_\lambda - \frac{3\beta_\lambda}{M_{r,\lambda}}\left[Q_\lambda^3 + Q_\lambda P_\lambda^2\right] \\
3\omega_{r,\lambda}^2 K_{2s} =& \frac{6\sqrt{2\alpha_\lambda\beta_\lambda}}{M_{r,\lambda}} Q_\lambda P_\lambda \\
3\omega_{r,\lambda}^2 K_{2c} =& \frac{3\sqrt{2\alpha_\lambda\beta_\lambda}}{M_{r,\lambda}}\left[Q_\lambda^2 - P_\lambda^2\right] \\
8\omega_{r,\lambda}^2 K_{3s} =& \frac{\beta_\lambda}{M_{r,\lambda}}\left[P_\lambda^3 - 3Q_\lambda^2 P_\lambda\right] \\
8\omega_{r,\lambda}^2 K_{3c} =& \frac{\beta_\lambda}{M_{r,\lambda}}\left[3Q_\lambda P_\lambda^2 - Q_\lambda^3\right]
\end{aligned} \tag{4.53}$$

where $Q_\lambda = \mathbf{q}_{r,\lambda}(0)$, $P_\lambda = \mathbf{p}_{r,\lambda}(0)/(M_{r,\lambda}\omega_{r,\lambda}^2)$ and $\Omega_\lambda = \left[\omega_{r,\lambda}^2 - \frac{4\alpha_\lambda}{M_{r,\lambda}}\right]^{1/2}$. With a complete solution $\mathbf{q}_{r,\lambda}^{(1)}(t)$, we do the same for the perturbation term, ρ. The solution is:

$$\mathbf{q}_{r,\lambda}^{(1\rho)}(t) = -\frac{C_{r,\lambda}}{M_{\lambda\omega_{r,\lambda}^2}}\left[\mathbf{q}_s(t) - \mathbf{q}_s^{(0)}(t)\cos\omega_{r,\lambda}t - \int_0^\infty dt'\dot{\mathbf{q}}_s(t')\cos\omega_\lambda(t-t')\right] \tag{4.54}$$

We see here that the counter term we used cancels out with the full expression for $\mathbf{q}_{r,\lambda}(t)$. Further, we see that we can use the above solutions and the original Langevin equation for Brownian motion to write the expression:

$$M_s\dot{\mathbf{q}}_s(t) + U_s(\mathbf{q}_s(t)) + \int_0^t \gamma^2 \sum_\lambda \frac{C_{r,\lambda}^2}{M_{r,\lambda}\omega_{r,\lambda}}\cos\omega_{r,\lambda}(t-t')\dot{\mathbf{q}}_s^{(0)}(t)dt' = \Gamma(t). \tag{4.55}$$

We are interested in finding an expression for $\Gamma(t)$ because by the definition of the Langevin equation for a harmonic oscillator in a medium which takes the form:

$$M\frac{d\mathbf{v}}{dt} = -\mu\mathbf{v} + \Gamma(t) - kx, \tag{4.56}$$

where M is mass, $\boldsymbol{v}$ is velocity, kx is the harmonic spring constant multiplied by displacement from the original position, and $\Gamma(t)$ is the noise term.

To further simplify the expression, we must set some parameters based on what is happening in our system. The relaxation time of the Brownian particle will be significantly shorter than the relaxation time of the reservoir. Therefore, we equate $\mathbf{q}_s^{(0)}(t) = \mathbf{q}_s(t)$ to simplify the expression:

$$M_s\dot{\mathbf{q}}_s(t) + \frac{\partial U_s(\mathbf{q}_s(t))}{\partial \mathbf{q_s}(\mathbf{t})} + \gamma^2 \sum_\lambda \frac{C^2_{r,\lambda}}{M_{r,\lambda}\omega_{r,\lambda}} \int_0^t \cos\omega_{r,\lambda}(t-t')\dot{\mathbf{q}}_s(t)dt' = \Gamma(t). \tag{4.57}$$

To determine the contribution of the noise, we need to take the time auto-correlation of the noise function, $\Gamma(t)$. To do this, we use perturbation theory and model our system as a canonical ensemble. We use the probability function for a specific value of λ:

$$\mathcal{P}_\lambda = \frac{1}{Z}e^{-\hat{H}_\lambda/k_BT}. \tag{4.58}$$

The above equation gives us one of the probabilities. To obtain the probability of the whole system, we use:

$$\mathcal{P} = \Pi_\lambda \frac{1}{Z}e^{-\hat{H}_\lambda/k_BT}. \tag{4.59}$$

Using the Hamiltonian we found in Eq. (4.38), we separate the individual Hamiltonians into two components:

$$\begin{aligned} \hat{H}_0 &= \sum_\lambda \left[\left(\frac{\mathbf{p}^2_{r,\lambda}(t)}{2M_{r,\lambda}} + \frac{1}{2}M_{r,\lambda}\omega^2_{r,\lambda}\mathbf{q}^2_{r,\lambda}(t)\right)\right], \\ \hat{H}_{1,\lambda} &= \left(U_{r,\lambda}(\mathbf{q}_{r,\lambda}(t)) - \frac{1}{2}M_{r,\lambda}\omega^2_{r,\lambda}\mathbf{q}^2_{\mathbf{r},\lambda}(t)\right). \end{aligned} \tag{4.60}$$

We recognize that the solution follows the fluctuation-dissipation theorem from here. For the noise contribution to the power spectrum up to second-order terms, we obtain:

$$\langle\Gamma(t)\Gamma(t')\rangle = \frac{\gamma}{\beta_\lambda} + \lambda^2\epsilon \sum_\nu \frac{D_{r,\lambda}C^2_{r,\lambda}}{M_{r,\lambda}\omega^2_{r,\lambda}} \cos\omega_{r,\lambda}(t-t'). \tag{4.61}$$

The variable $D_{r,\lambda}$ can be written as:

$$D_{r,\lambda} = \frac{1}{k_BT}\left(\frac{1}{2} - \frac{2\alpha_\lambda}{M_{r,\lambda}\omega^2_{r,\lambda}}\right) - \frac{1}{(k_BT)^2}\frac{6\beta_\lambda}{(M_{r,\lambda}\omega^2_{r,\lambda})^2}. \tag{4.62}$$

From these equations, we recover an expression that reflects higher-order $\frac{1}{k_BT}$ corrections to the fluctuation-dissipation theorem. The dissipation in the system can be tuned based on the values of α_λ and β_λ. It is important to note that the order of the noise is $\frac{1}{k_BT}$, which is comparable to the energy of our system.

The physical meaning of $D_{r,\lambda}$ is not entirely intuitive. The terms α and β are adjustable parameters that define the AH well. These will be specific to each system. While we write them as constants, they might depend on spatial coordinates or frequency, as do the displacement term prefactors in AH codes like sTDEP. To obtain a more physical understanding of the behavior of the noise, we can compare its behavior at different temperatures. We can calculate values at different temperatures if we assume that the only explicit temperature dependence comes from T. Setting all variables equal to 1 and letting $\omega_{r,\lambda}$ range from 0 to 100, we can substitute different temperatures. For this example, we take a ratio of $D_{r,\lambda}$ for 10 K, 300 K, and 1000 K. Between 10 K and 300 K, $D_{r,\lambda}$ increases thirty times. Between 10 K and 1000 K, it increases one hundred times, shown in Fig. 4.9. The corresponding value for the noise time correlation appears in Fig. 4.10. This function behaves similarly to the proposed Gaussian impulse model shown in Fig. 4.11.

To further validate this model, we need to perform molecular dynamics simulations. For example, we should tune the peaks in Fig. 4.10 to determine if they numerically correspond to particle collision times in MD simulations.

Addressing Other Colors of Noise

The previous section described a model where the oxygen atoms act as independent Einstein oscillators undergoing Brownian motion that introduce Brownian noise into the power spectrum. Here we discuss the possibilities of other types of noise, specifically pink noise. We assume the oxygen atoms act as unperturbed Einstein oscillators similar to the previous Brownian model. Returning to the concept of $\frac{1}{\mathbf{f}^{\kappa}}$ noise. We examine the $\kappa = 1$, known as the pink noise case.

Revisiting Eq. (4.1), we showed the corrections to the phonon self-energy for a phonon of energy $\hbar\Omega$. In these equations, the real part of the phonon self-energy Δ shifts the phonon energy, and the imaginary component Γ in Eq. (4.2) broadens it. We will use these equations to show that the diffuse spectra do not come from pink noise from a superposition of Lorentzian functions.

Previous work has shown that a superposition of Lorentzian functions can approximate all complex functions that obey the Kramers-Kronig relations [36]. Moreover, the Kramers-Kronig relations result from causality in both the frequency and time domain, which tells us a response must follow a cause.

In an ideal INS experiment, the one-phonon neutron cross section can be written as:

$$\sigma_\lambda(\Omega) \propto \frac{2\omega_\lambda \Gamma_\lambda(\Omega)}{\left[\Omega^2 - \omega_\lambda^2 - 2\omega_\lambda \Delta_\lambda(\Omega)\right]^2 + 4\omega_\lambda^2 \Gamma_\lambda^2(\Omega)}. \tag{4.63}$$

In the above equation, we measure the probing energy $\hbar\Omega$ during an experiment. It is the likelihood of exciting a phonon with momentum $\mathbf{q}$ and energy $\hbar\Omega$. ω_λ^2 is an eigenvalue of the dynamical matrix for the one phonon process λ. It is analogous to measuring the phonon lineshape when varying the probing energy.

We can use the Kramers-Kronig transform to obtain the real part of the phonon self-energy:

$$\Delta(\Omega) = \frac{1}{\pi} \int \frac{\Gamma(\omega)}{\omega - \Omega} d\omega \tag{4.64}$$

For our specific case, we can rewrite the one-phonon scattering cross section in terms of a superposition of Lorentzian functions. The desired form of our function is given by:

$$\mathcal{L}(\omega') = \frac{1}{\pi} \frac{\frac{1}{2}\Gamma'}{(\omega' - \omega_0')^2 + \left(\frac{1}{2}\Gamma'\right)^2}. \tag{4.65}$$

In the previous equation, $\mathcal{L}$ designates the Lorentzian function. When the resonance frequency, ω_0', is greater than zero, then ω' is a subsidiary frequency. Γ' is a bandwidth. The prime designation differentiates these variables with the frequencies in the one-phonon cross-section.

Comparing this function to the one-phonon scattering cross-section, we find that in the limit where $\Gamma_\lambda(\Omega)$ and $\Delta(\Omega)$ approach small constant values, we recover a Lorentzian function. $1/\mathbf{f}^\kappa$ noise is commonly explained by a superposition of Lorentzian functions with a spread in relaxation times [32, 37]. It is tempting to argue that sTDEP generates pink noise through a superposition of Lorentzian function. However, this does not correspond with the physics of our system.

The Role of Discontinuities in Diffuse Spectral Intensity

While many interatomic potentials in DFT calculations are continuous, model systems could include discontinuities. For example, phase noise is a frequency-domain view of the noise spectrum around an oscillator signal. At the same time, jitters are a time-domain measure of the timing accuracy of the oscillator period. To get from the impulse to the spectral function, we take the autocorrelation of the displacement in time. While this does not reflect the random nature of a jump we are likely to see, it results in diffuse intensity.

Here we present a model system of copper atoms in a Morse Potential. We introduce a discontinuity in the atomic momentum and the resulting potential to show how this generates diffuse spectra that decrease with increasing energy. We assume interactions between nearest neighbors and the Born-von Karman boundary condition holds.

A Morse potential has the functional form:

$$V_{\mathrm{M}}(r) = D_{\mathrm{e}}\left(1 - e^{-\alpha(r-r_{\mathrm{e}})}\right)^2. \tag{4.66}$$

In the above equations, $\mathrm{D_e}$ is the depth of the potential well; α regulates the width of the well; $\mathrm{r_e}$ is the equilibrium atomic bond length; r is the distance between atoms.

From this, we obtain the force:

$$F_{\mathrm{M}} = -\frac{dV_M}{dr}. \tag{4.67}$$

In classical mechanics, the force equals the negative of a force constant multiplied by the the distance of the particle from its equilibrium point:

$$F = -k_f(r - r_{\mathrm{e}}). \tag{4.68}$$

Solving for the forceconstant, k_f, and substituting Eq. (4.67) into the above equation,

$$\begin{aligned} k_f(r) &= -F/(r - r_{\mathrm{e}}) \\ &= -\frac{2aD_e(V(r)^2 - V(r))}{(r - r_{\mathrm{e}})}. \end{aligned} \tag{4.69}$$

In Chapter 3, we compared the accuracy of quasiharmonic (QH) and AH models to predict the thermal expansion and overall phonon behavior in cuprite at temperatures from 10 K to 300 K. Here we look at higher temperature single-crystal measurements taken at 700 K and 900 K. Next, we focus on the overall phonon behavior, exhibiting exciting features at elevated temperatures. At higher temperatures, the spectra take on a diffuse appearance. Neither our sTDEP nor MLIP calculations show this behavior.

Higher-Order Anharmonic Contributions

The previous study of cuprite (see Ch.3) showed that higher-order AH terms might be needed to model the microscopic temperature-dependent dynamics correctly.

To further ascertain the role of higher-order AH terms play in reproducing the DII, we compared phonon dispersions calculated with sTDEP with results from the MLIP package with LAMMPS as described in Section 4.2. While the former considered AH terms to cubic order, the latter included all AH terms.

From the AH approximation, we know that the three-phonon processes cause the phonon spectral function to approach zero as we approach double the maximum phonon frequency. For cuprite, this upper bound is roughly 600 K, which is approximately 75 meV [38]. Including the factor of two, we expect the dispersion to approach zero as we increase in frequency up to 100 meV, as seen in Fig. 4.12.

Based on the observed behavior, we know that three-body AH terms are not entirely responsible for the DII. If it were, DII would be a significant component in the majority of, if not all, phonon dispersions at nonzero temperatures. However, we observe that MLIP produces more noise than sTDEP. Therefore, while higher-order AH terms do not generate sufficient noise, we see that they play a small part in creating DII. We examine the similarities and differences in our simulations to determine why MLIP calculated dispersions show more uniform noise in the phonon spectra than sTDEP. Notably, sTDEP and MLIP calculations showed cuprite's distinct low-energy acoustic and optical modes. However, as seen in Fig. 4.13 the experimental results show nontrivial broadening in this range.

Gaussian Impulse Model

The high-energy optical modes show a modest softening and considerable broadening in the calculations with an increase in temperature (Fig.4.14). In Chapter 3, we mentioned the relationship between the size of the lattice constant and the central positions of the optical peaks, so we can reasonably attribute the softening of the high-energy optical modes to the change in lattice size from thermal expansion (Appendix C).

Below 40 meV, the experimental DII is prominent and appears as a background signal beneath the phonon dispersion curves. The curves significantly broaden at 300 K, but still retain features. The DII is characteristically similar to diffuse scattering from displacement disorder in a diffraction pattern. We adapt this displacement disorder model to work in the time domain.

In the cuprite system, we postulate that the motion of the O-atoms is disturbed by sudden momentum transfers from adjacent Cu atoms in the time domain. The momentum transfers abruptly change the O-atom's vibrational phase, resulting in a discontinuous force and momentum. The momentum takes a similar form to a boxcar or unit impulse function. This behavior is analogous to phase noise and jitter behavior seen in electronic band-pass filters that attenuate frequencies that fall outside a specific range. The resulting signal is filtered, but contains noise-like artifacts from the attenuation in both the frequency and time domains. Here we offer a similar analytical model for phase and amplitude disorder in the time domain for the dynamics of an A-atom with B-neighbors analogous to the O-atom and Cu-atoms in cuprite.

For an unperturbed Einstein quantum oscillator, we have the usual equations of motion for the oxygen atom in the cuprite crystal:

$$i\hbar\frac{\partial}{\partial t}\hat{a}(x,t) = \left[\hat{a}(x,t),\hat{H}\right] = \hbar\omega(x,t). \tag{4.70}$$

The subsequent Hamiltonian for this setup is:

$$\hat{H} = \hbar\omega\left(\hat{a}^\dagger\hat{a} + \frac{1}{2}\right) \tag{4.71}$$

where the lowering and raising operators $\hat{a}$(x,t) and $\hat{a}^\dagger$(x,t), for a phonon with frequency ω_0 are, respectively:

$$\hat{a}(x,t) = \hat{a}(x)e^{-i\omega_0 t} \tag{4.72}$$

and

$$\hat{a}^\dagger(x,t) = \hat{a}^\dagger(x)e^{i\omega_0 t}. \tag{4.73}$$

These operators allow us to construct a real wavefunction solution for an Einstein oscillator:

$$\psi(x,t) = \sqrt{\frac{\hbar}{2\omega_0}}\left[\hat{a}(x)e^{-i\omega t} + \hat{a}^\dagger(x)e^{i\omega t}\right]. \tag{4.74}$$

Looking at the phonon dispersions along the high-symmetry path in Fig. 3.2, the form of the modes does not vary wildly, meaning the O-atom vibrations do not have a strong **Q**-dependence. Therefore, we neglect the **Q**-dependence of the phonons, unit location, or any spatial information. This assumption allows for the simplification of Eq. (4.74).

$$\begin{aligned}\psi^*(t=0) &= \sqrt{\frac{\hbar}{2\omega_0}}\left[\hat{a}^\dagger + \hat{a}\right]\ , \\ \psi(t) &= \sqrt{\frac{\hbar}{2\omega_0}}\left[\hat{a}e^{-i\omega_0 t} + \hat{a}^\dagger e^{i\omega t}\right]\ . \end{aligned} \tag{4.75}$$

The double differential cross-section for one phonon inelastic neutron scattering in the incoherent approximation is [39]:

$$\left(\frac{d^2\sigma}{d\Omega dE}\right) = \frac{k_f}{k_i}\frac{N}{M}e^{-2W}\frac{\mathbf{Q}^2}{3}\frac{\sigma}{2\pi\hbar}\int_{-\infty}^{\infty} e^{-i\omega t}\left\langle \psi^*(0)\psi(t)\right\rangle dt\ . \tag{4.76}$$

In this equation, N is the number of atoms; M is the atomic mass, σ is the neutron scattering cross section. The shape of the energy spectrum is from the integral, where $\langle\rangle$ denotes the thermal average:

$$I(\omega) = \int_{-\infty}^{\infty} e^{-i\omega t}\left\langle \psi^*(0)\psi(t)\right\rangle dt\ . \tag{4.77}$$

We need to calculate the time autocorrelation function in the above expression: $\langle\psi^*(0)\psi(t)\rangle$. This is straightforward for a harmonic oscillator:

$$I(\omega) = \int_{-\infty}^{\infty} e^{-i\omega t}\frac{\hbar}{2\omega_0}\left[\left\langle \hat{a}^\dagger\hat{a}\right\rangle e^{-i\omega_0 t} + \left\langle \hat{a}\hat{a}^\dagger\right\rangle e^{i\omega_0 t}\right] dt\ . \tag{4.78}$$

The thermal averages for our harmonic oscillator give:

$$I(\omega) = \frac{\hbar}{2\omega_0}2\pi\left[\langle n\rangle\,\delta(\omega+\omega_0) + \langle n+1\rangle\,\delta(\omega-\omega_0)\right]\ . \tag{4.79}$$

This $I(\omega)$ has two peaks at $\pm\omega_0$ about the elastic line with relative intensities as expected from detailed balance as $\frac{\langle n+1\rangle}{\langle n\rangle}$.

However, the oxygen atom (atom A) does not behave like a simple harmonic oscillator for more than a few cycles. The model assumes that brief interactions with a heavier B-atom modify an A-atom's motion. Furthermore, we presume A- and B-atoms vibrate independently and have significantly different frequencies, which is the case for oxygen and copper. When an A- and B-atom reach a critical distance, a transfer of impulse $\pm\Delta p$ occurs that alters the dynamics of the lighter A-atom oscillation. This interaction causes a sudden change in the forces between the atoms and the resulting energy of the A-atom. Although this alters the energy, the thermal average remains $k_\mathrm{B}T$. However, there is an error in the phase of oscillation that is cumulative.

We expect phase changes with positive and negative signs. Overall, the phase changes average to zero but have a mean-squared error that grows with the number of impulse transfers. This provides a basic explanation that originates from the van Hove function of Eq. (**??**), but we can look at the specific dynamics of this system. The momentum of the A-atom has a time-dependence

$$\psi_\mathrm{A}(t) = \psi_0\left\{\exp(\mathrm{i}[\omega_\mathrm{A}t + \phi_{\mathrm{A|B}}(t)]) + c.c.\right\} \tag{4.80}$$

which would have pure frequencies $\pm\omega_{\mathrm{A}}$ if ϕ were constant, with a spectral shape of $I(\omega) \simeq \delta(\omega \mp \omega_{\mathrm{A}})$. For nonzero $\phi_{\mathrm{A|B}}(t)$, a time-averaged spectrum would have a spread in frequencies that increases with the amplitude of the stochastic function ϕ and the frequency of energy transfers, $1/\tau$. Analogously, phase noise in oscillators has a power spectrum that is peaked near ω_0, but has broad tails that extend over a wide range of frequencies [40]. In our model, the characteristic time τ for the phase errors of the A-atom is the period of oscillation of the B-atom ($\tau = 2\pi/\omega_{\mathrm{B}}$). The frequency spectrum of the real fluctuating quantity $\psi_{\mathrm{A}}(t)$ is obtained from its time-time correlation function over long times, and the Wiener-Khinchin theorem.

Each stochastic change of phase of the A-atom, $\Delta\phi$, is assumed to have a Gaussian probability distribution with zero mean and a standard deviation, γ. This changes when we look at the first impulse transfer at time τ

$$P_{\Delta\phi}(t) = \frac{1}{\sqrt{\pi}\,\gamma}\,\mathrm{e}^{-(t-\tau)^2/\gamma^2}. \tag{4.81}$$

The second impulse transfer from the B-atom adds to the phase uncertainty of the A-atom. With respect to the phase at the initial time, it is the convolution of Eq. (4.81) with itself, giving a Gaussian with standard deviation $\sqrt{2}\gamma$. The convolution with Eq. (4.81) is performed at each time interval τ, so

$$P_{\phi}(t) = \sum_{n=-\infty}^{\infty} \frac{1}{\sqrt{|n|\,\pi\,\gamma}}\,\mathrm{e}^{-(t-n\tau)^2/(|n|\gamma^2)} \tag{4.82}$$

which is a sum of Gaussians spaced by intervals of τ and the width of the Gaussians increase with time. The case $n = 0$ is taken as the limit $\tau \to 0$, giving a δ-function of unit area. Terms with negative n give the phase distributions at earlier times that give the reference phase at $t = 0$.

The power spectrum from the phase disorder, $I(\omega)$, is the Fourier transform of the time-time correlation function, $P_{\phi}(t)$

$$I(\omega) = \int_{-\infty}^{\infty} e^{-i\omega t}\Big(\sum_{n=-\infty}^{\infty} \frac{1}{\sqrt{|n|\,\pi\,\gamma}} e^{-(t-n\tau)^2/(|n|\gamma^2)}\Big)dt\ . \tag{4.83}$$

Substituting $t' = t - n\tau$ and taking Fourier transforms of the series of Gaussian functions:

$$I(\omega) = \sum_{n=-\infty}^{\infty} e^{-\omega^2|n|\gamma^2/4}\ e^{-in\omega\tau}\ . \tag{4.84}$$

Evaluating Eq. (4.84) as two geometric series [41]

$$I(\omega) = \frac{1}{1-\exp\big[-\omega^2\gamma^2/4+\mathrm{i}\omega\tau\big]} + c.c. - 1\ , \tag{4.85}$$

$$I(\omega) = \frac{1-\mathrm{e}^{-\omega^2\gamma^2/2}}{1+\mathrm{e}^{-\omega^2\gamma^2/2}-2e^{-\omega^2\gamma^2/4}\cos(\omega\tau)}\ . \tag{4.86}$$

A time-time correlation function for the phase of the A-atom, of Eq. (4.82), is shown in Fig. 4.16a for the ratio $\gamma = \tau/3$. The corresponding $I(\omega)$ of Eq. (4.86) is shown in Fig. 4.16b for $\gamma = \tau/3$ and two other ratios, showing the sensitivity of the fluctuation spectrum to the ratio γ/τ. Small values of γ/τ give sharp features in the spectrum at the characteristic frequency of the B-atom and its harmonics. These features would be difficult to observe in experiments because the main peak of Fig. 4.16b largely overlaps the spectrum from the Einstein mode of the B-atom at ω_B. Small changes in the value of γ greater than $\tau/3$ quickly eliminate the peaks in the intensity spectrum however, as shown in Fig. 4.16b.

In all cases, our stochastic model for $I(\omega)$ of the A-atom rises gradually from zero to a plateau at approximately $2\omega_\mathrm{B}$. A roll-off at low frequencies is predicted with Eq. (4.86), and seems consistent with the low intensity below the acoustic modes in Fig. 4.13. Although the analytical form of $I(\omega)$ extends to infinity in ω, there must also be a roll-off at large ω because the impulse is not instantaneous.

For $\mathrm{Cu_2O}$, first, consider how the Einstein modes of the O-atoms alter the dynamics of the Cu-atoms. The characteristic time for the O-atom vibration is $\tau \simeq 1.7 \times 10^{-13}$ sec (70 meV). This was the τ used for numerical values in Fig. 4.16. The γ is less certain, but should increase with temperature, smoothing any peaks in $I(\omega)$. We can make similar arguments for how impulse transfers from neighboring Cu-atoms alter the O-atom dynamics. This transfer should be a strong effect, owing to the mass difference between Cu and O.

When Cu-atoms alter the dynamics of O-atom vibrations, we expect a broad inelastic spectrum from phase fluctuations at the energies above the peak of the Cu phonon partial DOS at 12 meV (Fig. 3.4). Several phonon dispersions are in this energy range, spreading the normal mode spectrum and allowing the multiple contributions of the phase fluctuation spectra to be proportionately larger.

The momentum of the B-atom increases as $\sqrt{2mk_\mathrm{B}T}$. We expect the impulse transfers to increase as $\sqrt{T}$, and the relative intensity of the broad background from phase fluctuations to increase with T, in qualitative agreement with the experimental trend of Fig. 4.13. A small change in γ can quickly smooth the distinct phonon peaks in $I(\omega)$.

In our model, the atoms that dominate the phase fluctuation spectra are the neighbors of the atoms that dominate the normal modes. We expect the fractional contribution to the diffuse intensity in $I(\omega)$ at energies below 50 meV to be from O-atoms scattered out of their vibrational modes by the slower-moving Cu-atoms in their first-neighbor shell. Above 50 meV, we expect the diffuse background to originate from Cu-atoms perturbed by the faster-moving O-atoms. Quantitative interpretations would require consideration of the different phonon modes that can interact in cuprite and the transition towards classical behavior as the low-energy modes (such as the band at 10 meV) become more occupied with temperature. Correlations in the motions of Cu and O-atoms would bring structure to the diffuse intensity.

This approach assumes that the noise is uniform throughout the spectrum. While sTDEP calculations show the phase noise appearing prominently in the lower energy modes, MLIP calculations capture more of this broad diffusivity than the experimental INS results.

Anharmonic Interference

When investigating the DII in cuprite, we would be remiss if we did not address the phenomenon known as AH interference. Ambegaokar, Conway, and Baym first proposed AH interference at the 1963 International Conference on Lattice Dynamics [42]. While the theory of it was a topic of interest in lattice dynamics in the 1960s, there was a lack of convincing experimental evidence. There has been no further experimental validation in the years following its inception. Initially defined as the diffuse spectral intensity from the interaction between the one-phonon contribution to the dynamic structure factor with various multiphonon components, we extend the idea past the one-phonon case.

Since the 1960s, advancements in code packages have allowed us to work with higher-order phonon effects. For example, AH interference can form from the interaction of an n-phonon process with an m-phonon process. In this portion of the text, we endeavor to determine if AH in cuprite is sufficiently large enough to cause a diffuse spectral intensity. If so, we must also determine if it would produce the type of Brownian noise we see in the phonon spectra.

The one-phonon cross-section has a resonant frequency equal to the phonon frequency. The corresponding lineshape for the one-phonon cross-section is equal to the inverse of the phonon lifetime. In materials with non-negligible AH interference, the resonant phonon frequency shifts from the phonon frequency, and the neutron scattering cross-section deviates strongly from a Lorentzian function.

The AH interference contribution to the dynamic structure-function, $S_p(\mathbf{Q}, E)$ between a one-phonon process with a multiphonon process in the original 1963 paper is:

$$S_p(\mathbf{Q}, \omega) = \frac{2e^{-2W}}{1 - e^{-\beta\omega}} \times Im \left[R_i(\mathbf{Q}, \omega - i\varepsilon) \mathcal{D}_{ij}(\mathbf{Q}, \omega - i\varepsilon) R_j(\mathbf{Q}, \omega - i\varepsilon) \right] . \tag{4.87}$$

The first term on the right hand of the above expression, $R_i(\mathbf{Q}, \omega - i\varepsilon)$ can be written as:

$$R_i(\mathbf{Q}, \omega - i\varepsilon) = \mathbf{Q}_i + \int_{\infty}^{\infty} \frac{d\omega}{2\pi} \tag{4.88}$$

In the above expression, $\mathcal{D}_{ij}(\mathbf{Q} - i\varepsilon)$ is:

$$\mathcal{D}_{ij}(\mathbf{Q}, \omega - i\varepsilon) = \int_{\infty}^{\infty} \frac{d\omega}{2\pi} \frac{A_{ij}}{\mathbf{Q}, \omega} \tag{4.89}$$

These expressions are far too small in magnitude to generate the noise that we see.

In his 1963 paper on AH corrections for a cubic crystal, Thompson estimates the intensity ratio of the interference terms to the total intensity [43]. He estimates that the AI contributes approximately 1% to the one-phonon peak. Overall he estimates an even more minor correction of 0.01% for the Bravais lattice. While we cannot entirely isolate the DII to obtain a corresponding percentage, we observe a more significant effect than Thompson's calculated percentages. Further, his estimation shows that the AI contribution for the one-phonon case directly depends on the thermal expansion. However, cuprite has very small thermal expansion coefficients even at elevated temperatures. Therefore it is unlikely that AI is responsible for the diffuse background.

4.5 Conclusions

In this work, we performed calculations on cuprite using the AH codes sTDEP and MLIP to explain the DII. At the same time, each code produced some degree of this diffuse phenomenon, but neither fully matched what we saw in the experimental INS data at 700 K and 900 K. To further understand the underlying mechanisms of the DII, we proposed and tested a Gaussian impulse model that relied on the mass discrepancies between the oxygen and copper atoms which we saw as phase differences. In addition, we analyzed the possibility of a failing of the incoherent approximation, which would present a noise-like background if present. We also looked at the role force discontinuities play in noise production. Lastly, we looked into AH interference. While AH interference would produce the type of noise we expect to see, it would not be sufficiently large enough.

We addressed several possible origins of the DII in cuprite throughout this chapter. Concepts such as pink noise lack scientific justification in this setting. AH interference is too negligible in magnitude relative to the spectrum. Ideas such as Gaussian impulses in-phase and AH reservoirs provide classical and quantum explanations for this phenomenon. However, a more in-depth analysis of other compounds is required.

These are promising models, and it may be possible to use them with molecular dynamics calculations to give more quantitative comparisons to experimental measurements of DII.

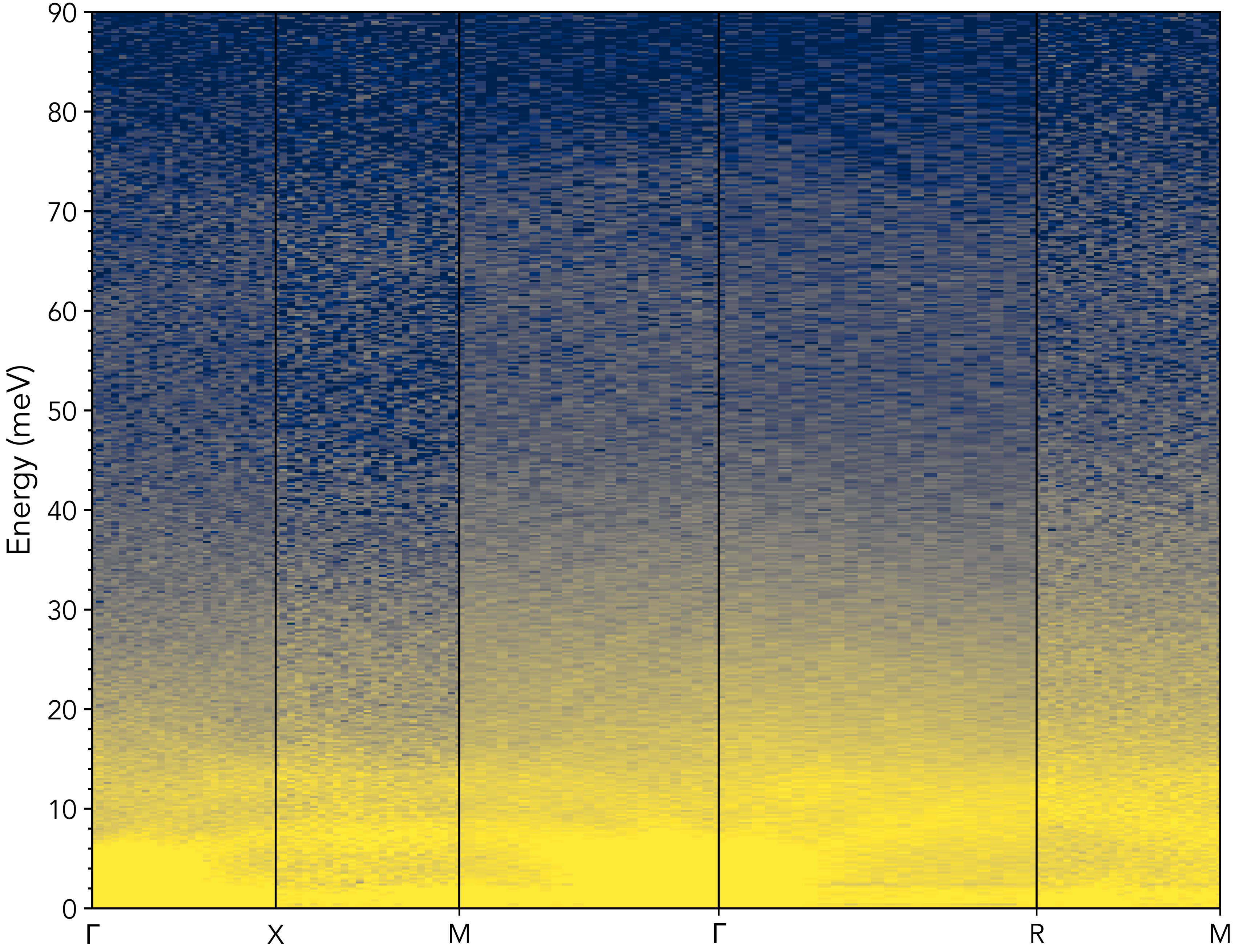

Figure 4.7: Zoomed in portion of Fig. 3.2a

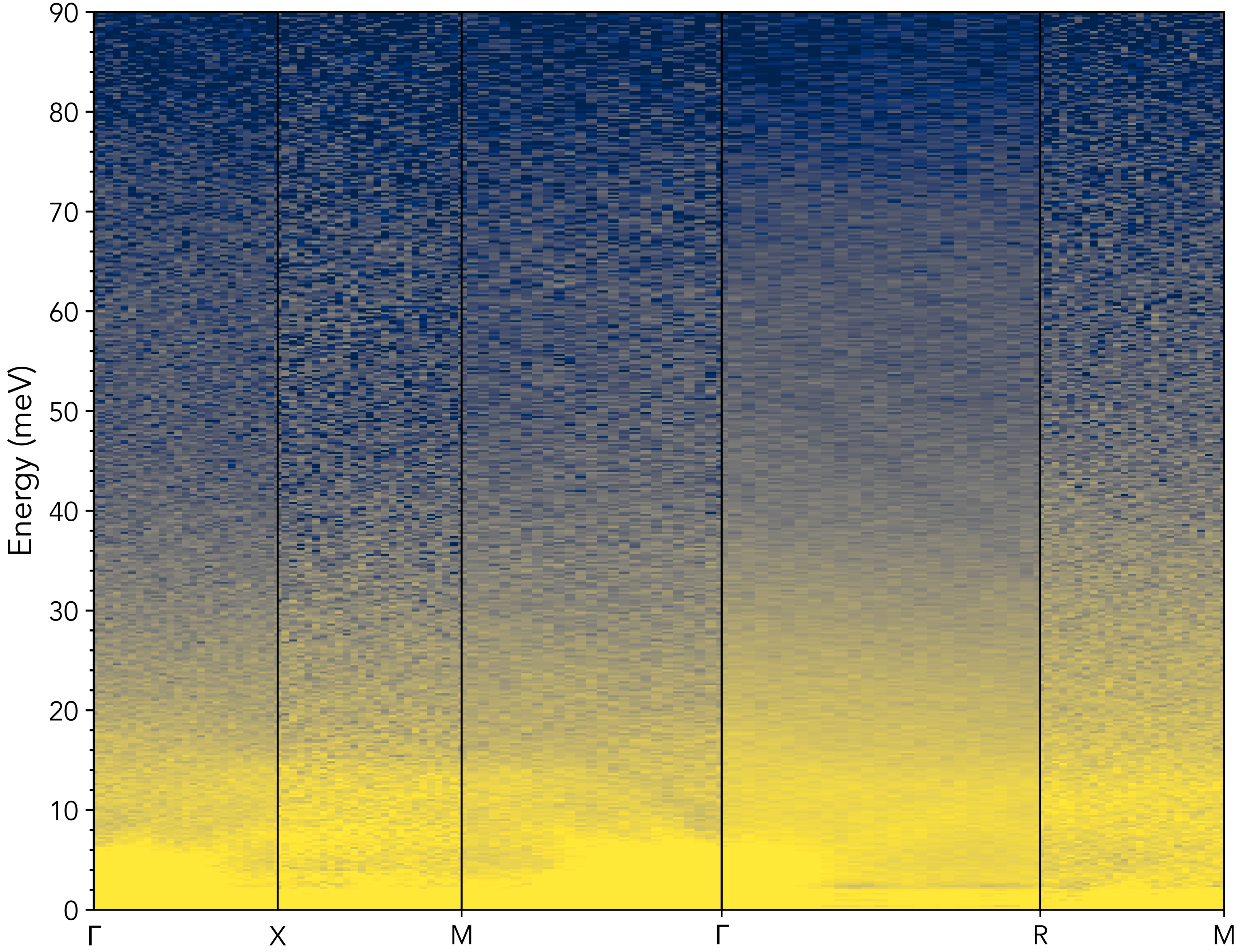

Figure 4.8: Zoomed in portion of Fig. 3.2c

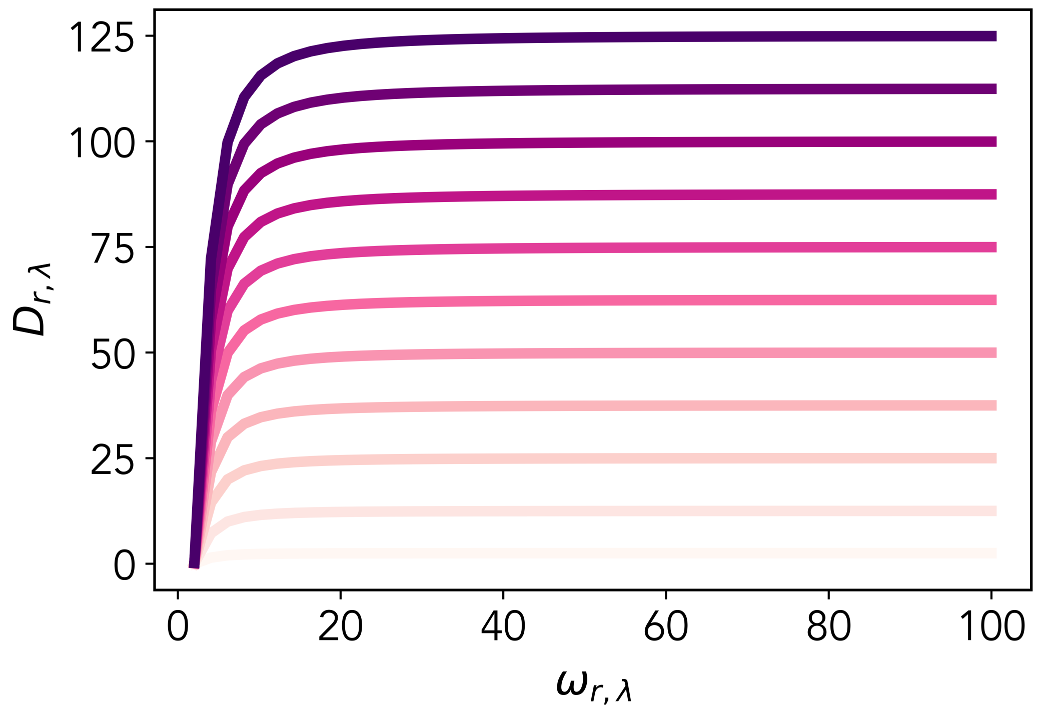

Figure 4.9: Comparison of $D_{r,\lambda}$ for different temperature values. Low temperature values appear in light pink and high temperature values are in dark purple. The temperatures range from 10 K to 500 K. All other variables in the expressions are set to unity.

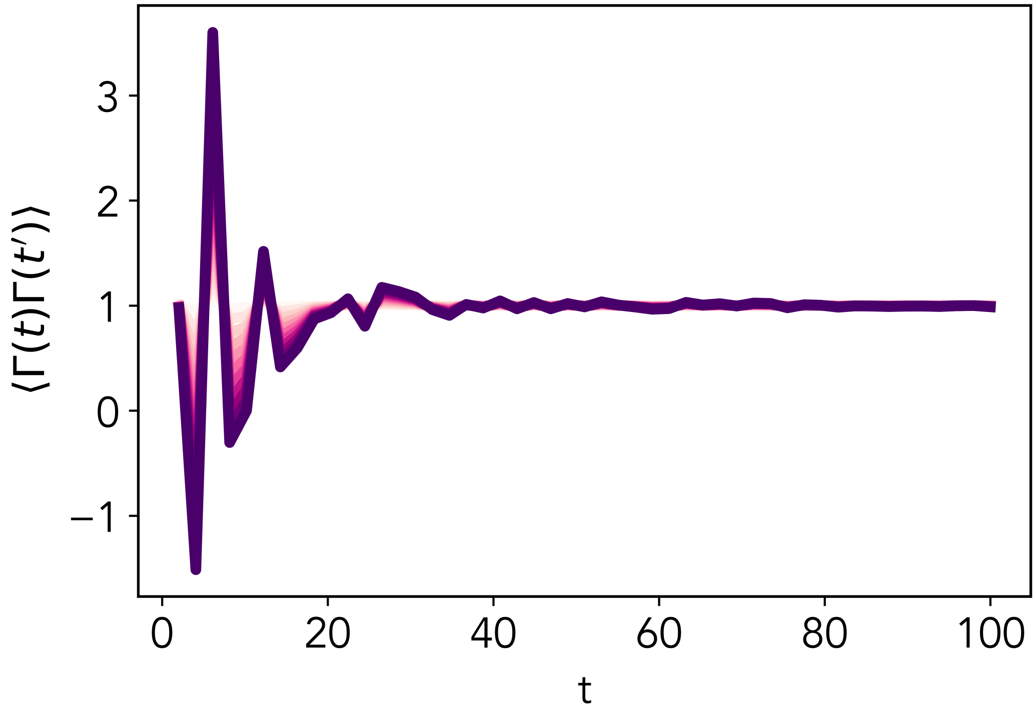

Figure 4.10: Comparison of the noise time correlation, $\langle\Gamma(t)\Gamma(t')\rangle$, plotted as a function of time from temperatures ranging from 10 K to 500 K. High temperatures are shown in dark purple, and low temperatures are shown in light pink. All other variables in the expressions are set to unity.

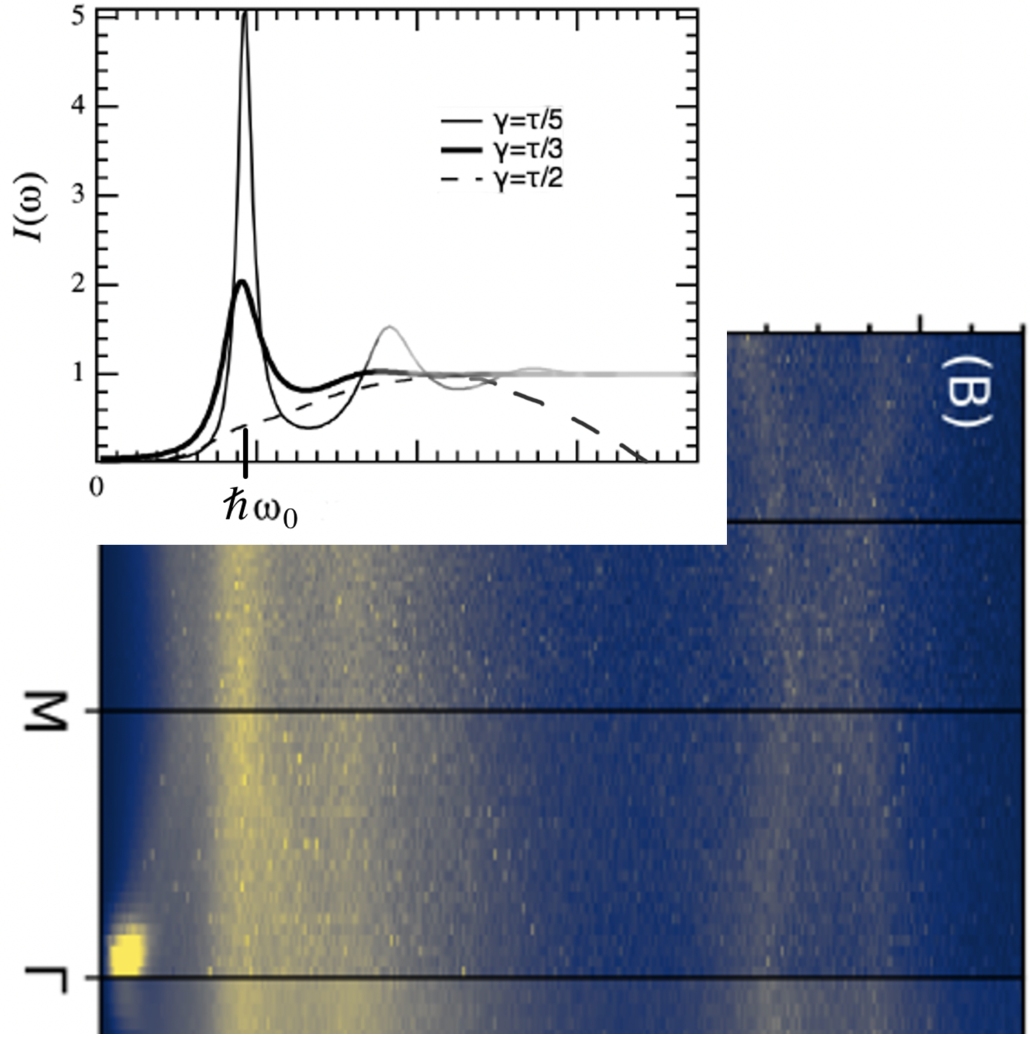

Figure 4.11: Comparison of spectral weight predicted in Fig. 4.13 with the experimental data from cuprite at 300 K. The positioning of the calculated curve is over the peak in the phonon scattering dominated by copper atoms, and the diffuse tails extend above and below the experimental range. The comparison suggests that $\gamma \simeq \tau/3$.

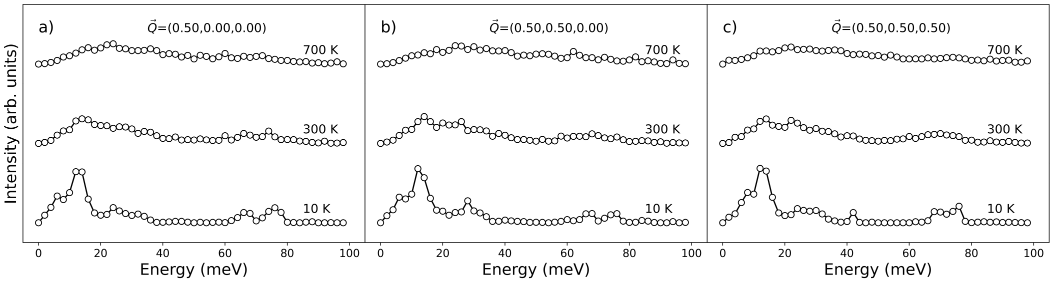

Figure 4.12: Cuts from the INS data for experimental data. Location in Q of the cut is shown in each panel. At high energy, the spectrum goes to zero.

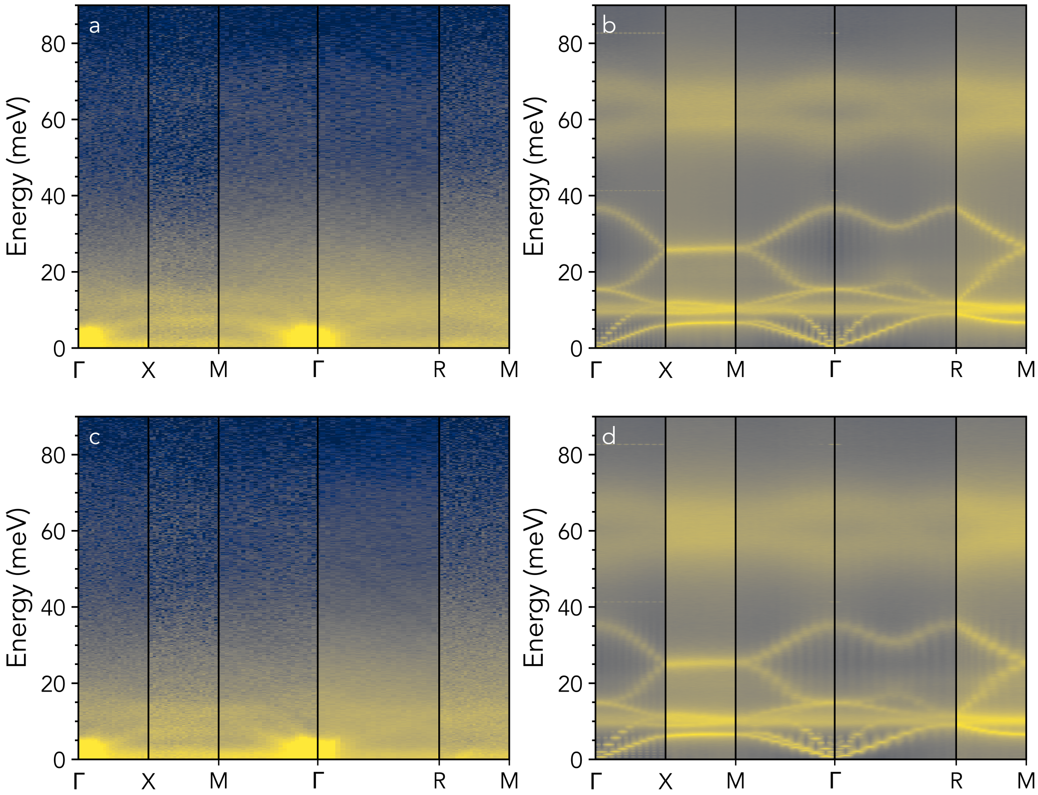

Figure 4.13: a, c) Phonon dispersions along high-symmetry directions measured by INS at 700 and 900 K respectively. Phonon dispersions calculated with MLIP at b) 700 K and d) 900K.

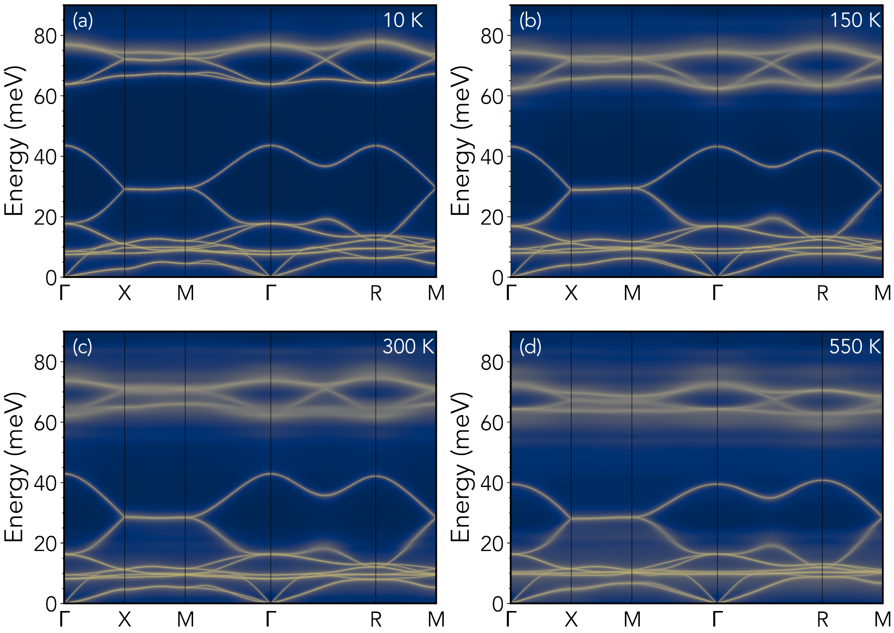

Figure 4.14: This plot shows calculated sTDEP phonon dispersions for (a) 10 K, (b) 150 K, (c) 300 K, (d) 550 K along the high-symmetry path.

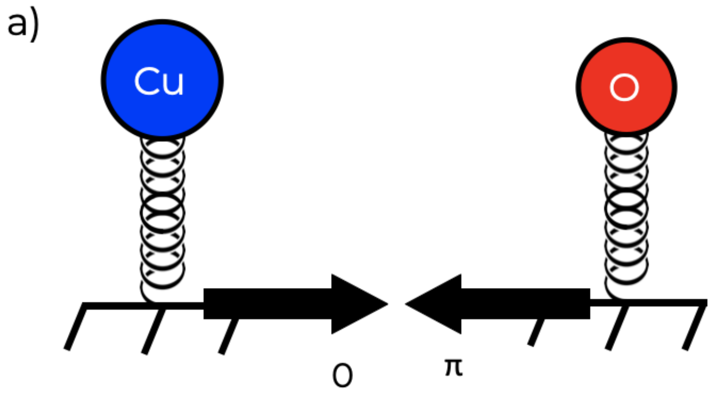

(a) This is a cartoon representation of the dynamics between the O (red) and Cu atoms (blue) before the impulse interaction. In this setup, the Cu and O have different phases.

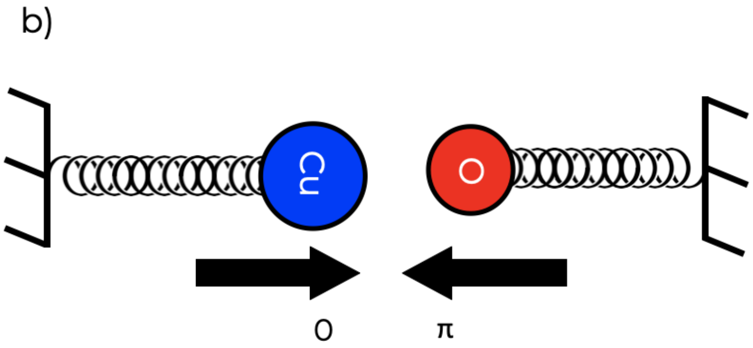

(b) This is a cartoon representation of the dynamics between the O and Cu atoms. As the O and Cu get closer, the dynamics of the O-atom are altered by an impulse transfer from the Cu.

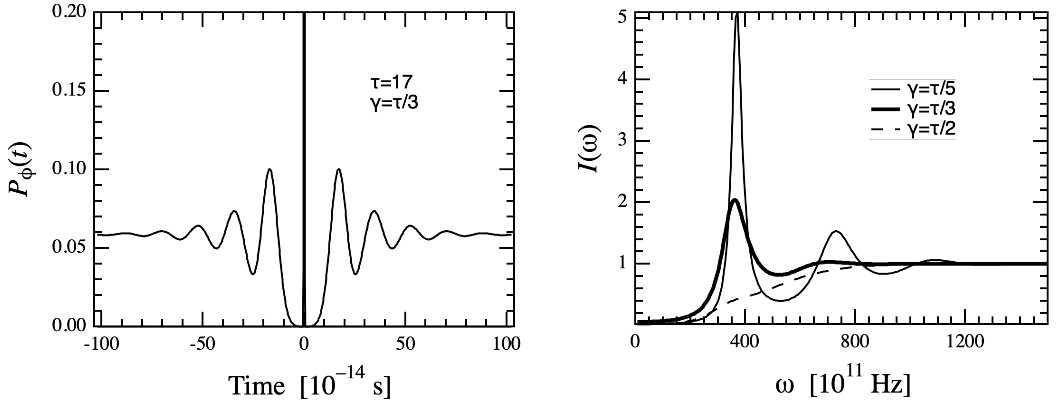

Figure 4.16: (a) Time-time correlation function of Eq. (4.82) for $\gamma = \tau/3$. (b) Intensity $I(\omega)$ of Eq. (4.86) from Fourier transform of panel a, for different ratios of γ/τ.

References

[1] Y. Shen, C. N. Saunders, C. M. Bernal, D. L. Abernathy, T. J. Williams, M. E. Manley, and B. Fultz, Phys. Rev. B **103**, 134302 (2021).

[2] F. Knoop, T. A. R. Purcell, M. Scheffler, and C. Carbogno, Phys. Rev. Mater. **4**, 083809 (2020).

[3] M. Sato and A. J. Sievers, Nature **432**, 486 (2004).

[4] M. E. Manley, A. J. Sievers, J. W. Lynn, S. A. Kiselev, N. I. Agladze, Y. Chen, A. Llobet, and A. Alatas, Phys. Rev. B **79**, 134304 (2009).

[5] M. E. Manley, D. L. Abernathy, N. I. Agladze, and A. J. Sievers, Sci. Rep. **1**, 4 (2011).

[6] M. E. Manley, O. Hellman, N. Shulumba, A. F. May, P. J. Stonaha, J. W. Lynn, V. O. Garlea, A. Alatas, R. P. Hermann, J. D. Budai, H. Wang, B. C. Sales, and A. J. Minnich, Nat. Commun. **10**, 1928 (2019).

[7] M. Kempa, P. Ondrejkovic, P. Bourges, P. Marton, and J. Hlinka, Phys. Rev. B **89**, 054308 (2014).

[8] S. Pailhès, H. Euchner, V. M. Giordano, R. Debord, A. Assy, S. Gomès, A. Bosak, D. Machon, S. Paschen, and M. de Boissieu, Phys. Rev. Lett. **113**, 025506 (2014).

[9] A. Rivière, S. Lepri, D. Colognesi, and F. Piazza, Phys. Rev. B **99**, 024307 (2019).

[10] H. R. Glyde and R. Taylor, Phys. Rev. B **25**, 6500 (1982).

[11] R. A. Cowley, E. C. Svensson, and W. J. L. Buyers, Phys. Rev. Lett. **23**, 525 (1969).

[12] O. Hellman and I. A. Abrikosov, Phys. Rev. B **88**, 144301 (2013).

[13] T. Lan, C. W. Li, J. L. Niedziela, H. Smith, D. L. Abernathy, G. R. Rossman, and B. Fultz, Phys. Rev. B **89**, 054306 (2014).

[14] G. E. P. Box and M. E. Muller, Ann. Math. Stat. **29**, 610 (1958).

[15] R. Brown, Philos. Mag. **4**, 161 (1828).

[16] A. Einstein, *Investigations on the theory of the Brownian movement*, Dover Books on Physics (Dover Publications, Mineola, NY, June 1956).

[17] J. L. Niedziela, R. Mills, M. J. Loguillo, H. D. Skorpenske, D. Armitage, H. L. Smith, J. Y. Y. Lin, M. S. Lucas, M. B. Stone, and D. L. Abernathy, Rev. Sci. Instrum **88**, 105116 (2017).

[18] A. P. Thompson, H. M. Aktulga, R. Berger, D. S. Bolintineanu, W. M. Brown, P. S. Crozier, P. J. in 't Veld, A. Kohlmeyer, S. G. Moore, T. D. Nguyen, R. Shan, M. J. Stevens, J. Tranchida, C. Trott, and S. J. Plimpton, Comp. Phys. Comm. **271**, 108171 (2022).

[19] A. Shapeev, Multiscale Model. Simul. **14**, 1153 (2016).

[20] J. P. Perdew, K. Burke, and M. Ernzerhof, Phys. Rev. Lett. **77**, 3865 (1996).

[21] S. Y. Krylov and J. W. M. Frenken, Sci. Rep. **11**, 19964 (2021).

[22] L. H. N. Rimmer, M. T. Dove, B. Winkler, D. J. Wilson, K. Refson, and A. L. Goodwin, Phys. Rev. B **89**, 214115 (2014).

[23] K. W. Chapman and P. J. Chupas, Chem. Mater. **21**, 425 (2009).

[24] A. O. Caldeira and A. J. Leggett, Phys. A: Stat. Mech. Appl. **121**, 587 (1983).

[25] G. N. Lewis, Proc. Natl. Acad. Sci. U.S.A. **11**, 179 (1925).

[26] S. Khorasani, Sci. Rep. **9**, 9075 (2019).

[27] C. U. Lei and W.-M. Zhang, Ann. Phys. **327**, 1408 (2012).

[28] A. Caldeira and A. Leggett, Phys. A: Stat. Mech. Appl. **121**, 587 (1983).

[29] R. Feynman and F. Vernon, Ann. Phys. **24**, 118 (1963).

[30] F. Haake and R. Reibold, Phys. Rev. A **32**, 2462 (1985).

[31] M. M. Ali, P.-Y. Lo, and W.-M. Zhang, New J. Phys. **16**, 103010 (2014).

[32] G. Zanella, *Superposition of similar single-sided rtn processes and 1/f noise*, 2005.

[33] T. Kofané and A. Dikandé, Solid State Commun. **86**, 749 (1993).

[34] L. LANDAU, Nature **138**, 840 (1936).

[35] C. Bhadra and D. Banerjee, J. Stat. Mech.: Theory Exp **2016**, 043404 (2016).

[36] C. A. Dirdal and J. Skaar, Phys. Rev. A **88**, 033834 (2013).

[37] G. Zanella, *Co-operation of two-state processes and 1/f noise*, 2003.

[38] M. Giar, M. Heinemann, and C. Heiliger, Phys. Rev. B **96**, 075202 (2017).

[39] S. W. Lovesey, *Theory of neutron scattering from condensed matter: volume ii: polarization effects and magnetic scattering* (Clarendon Press, 1986).

[40] A. Hajimiri and T. H. Lee, IEEE J. Solid-State Circuits **33**, 179 (1998).

[41] B. Fultz and J. Howe, "Patterson functions and diffuse scattering", in *Transmission electron microscopy and diffractometry of materials*, 4th ed. (Springer, Berlin, Heidelberg, 2013) Chap. 10, pp. 463–520.

[42] V. Ambegaokar, J. M. Conway, and G. Baym, in *Lattice dynamics*, edited by R. Wallis (Pergamon, 1965), pp. 261–270.

[43] B. V. Thompson, Phys. Rev. **131**, 1420 (1963).

Chapter 5

FINAL REMARKS AND FUTURE DIRECTIONS

In this work, we used experimental methods, computation, and theory to explain the mechanisms driving the thermal behavior of cuprite. We show the inherent value in using an anharmonic (AH) over a quasiharmonic (QH) model. AH models describe the thermal expansion behavior while simultaneously obtaining accurate macroscopic quantities and correct microscopic behavior.

We presented an in-depth look at the newly seen phenomena, diffuse inelastic intensity (DII), and proposed several models to describe the atomic behavior. These models go beyond perturbation theory and allow us to truly understand the factors that contribute to AH behavior in solids.

Understanding systemic trends in thermophysical properties of materials guides our comprehension of the fundamental AH mechanisms. However, machine learning (ML) models that attempt to predict phonon behavior using only atomic species and configurations as input fail to capture the role atomic interactions and dynamic behavior have in our understanding of more complex AH features like DII [1].

This final chapter presents the beginnings of a comparative study of experimental phonon linewidths. This analysis highlights the need for phonon data collection and post-processing standardization and how new experimental and computational methods reveal previously unseen anharmonic phenomena. We also address the future of single-crystal data analysis.

5.1 Advancements in Methods

Phonon linewidths are indicative of phonon lifetimes owing to 3-phonon processes. However, experimental phonon lineshapes often vary substantially between phonon branches in a material. Differences in experimental techniques further complicate this. Luckily, many trends are sufficiently large enough to see easily. The visibility of these trends is partly due to advancements in experimental methods and equipment. The three main methods are Raman, high-resolution inelastic X-rays, triple-axis, and TOF chopper spectrometry. Each differs in sample environments, data reduction methods, and instrument settings.

There is some standardization in the neutron scattering community in data collection. Most modern facilities capture data in event mode. Data captured in event mode maintains event information during the reduction and correction process, reducing the need for unnecessary corrections or renormalizations [2, 3]. Strides in big to medium data allow us to quickly process the 4-D $S(\mathbf{Q},\varepsilon)$ scattering functions which for single crystals are on the order of 50 to one hundred gigabytes. The tools now exist for users with limited computer science and data backgrounds to process their data in Python Jupyter notebooks, MATLAB, and customized tools while preserving data in event mode.

Improvements in instrumentation, sample environments, and data reduction allow us to examine artifacts in experimental methods that were previously unattainable [4]. For example, data from experiments of inelastic scattering of thermal neutrons performed on time-of-flight (TOF) chopper spectrometers with a high-flux pulsed neutron source provides improved instrument resolution in both **Q** and E over triple-axis spectrometer data [5–8]. TOF chopper spectrometers allow greater exploration of Q-space than triple-axis spectrometers which confine us to individual energy scans at single energy points in **Q**-space. This versatility is valuable when we want to explore features not along high-symmetry directions or weaker features visible only through the addition of multiple Brillouin zones.

We have seen simultaneous advancements in high-performance computing software and hardware with these experimental enhancements. These developments allow us to perform more ab initio calculations and use more advanced exchange-correlation functionals. These improved computational tools allow us to model highly correlated electronic systems more accurately at high temperatures and understand the phonons and thermodynamic behavior.

There have been significant advances in computational methods to describe anharmonic lattice dynamics in solids in the past decade. In a matter of years, the community went from writing new code specific to their system for each data analysis to having multiple packages to choose from. Some of these packages include but are not limited to ALAMODE [9–11], TDEP [12–14], CSLD [15–17], HIPHIVE [18], PHONO3PY [19], and SHENGBTE [20].

With every improvement in simulation, we seek to refine the experiments and data reduction to obtain new information once hidden by experimental noise or masked by approximations in our algorithms. Many existing codes accomplish this by calculating second-order and third-order force constants. However, quartic terms remain a computational challenge to decouple from quadratic terms.

Newer packages and plug-ins utilize machine-learning through MLIP or machine-learning force-fields (MLFF) [21, 22]. These codes include AH terms to infinite order; however, there is no straightforward way to isolate and identify the magnitude of each anharmonic term.

Predicting the magnitude of individual and total anharmonicity in materials is inherently valuable for our overall understanding of the properties in materials that are rooted in anharmonicity. Recent studies have proposed computational benchmarks to look at pure anharmonicity that was dependent on the standard deviation of the distribution of anharmonic force components obtained from ab initio forces and their harmonic approximation, normalized by the absence of external forces [23]. From a computational perspective, this works quite well. However, it is not entirely obvious how it carries over to experimental data, which is still the golden standard when determining the accuracy of anharmonic calculations.

5.2 Experimental Trends

We present an initial compilation of experimental lineshapes in the literature. Figure 5.1 shows the temperature dependence of the normalized lineshapes for the materials Pd, Si, CsI, Al, UO_2, and YNi_2B_2C. Since the y-axis is proportional to the three phonon process, we will talk about it as a measure of anharmonicity. Looking at Si, denoted by green circles, it falls on the lower end of what we would call an anharmonic material. The phonon linewidths of UO_2, shown with brown circles, are broader than Si by four factors. Comparing Si to other pure single elements with relatively simple structures like Pd and Al, we see that they all fall close in value, except for Al at higher temperatures. Notably, Si has small anharmonicity on the scale of Fig. 5.1. This trend is consistent with recent studies that argued that Si has low anharmonicity [24]. However, the AH phonon shifts are much more significant than QH shifts [25], which is also the case for cuprite. In general, the pure elements are less anharmonic overall. Although it is premature to conclude the anharmonicity of elements and compounds with ionic versus covalent, we can still see the beginnings of AH trends with plots such as this one. A major challenge in constructing a dataset like this one is that there is no standardization of data or post-processing. Some of what we attribute to anharmonicity are possibly artifacts leftover by instrumentation and data reduction.

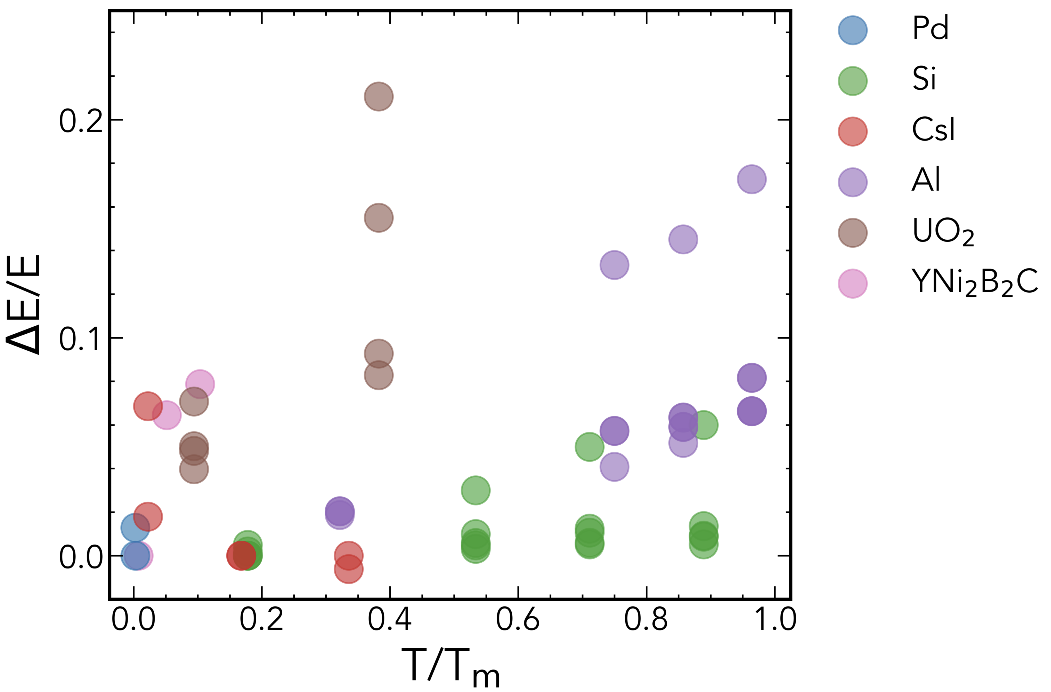

Figure 5.1: This plot compares phonon lineshapes for different materials [26–32]. The y-axis compares phonon lineshapes normalized by central energies. The x-axis shows the temperature weighted by the melting temperature.

5.3 The Future of Single Crystal Neutron Experiments

In this research, we worked with various teams to create better workflows for processing INS data of single crystals. From when we began today, techniques like data folding dispersion data for single crystals are increasingly feasible with new data structures and GPU-enabled codes. However, there has not been substantial analysis comparing folded and unfolded datasets. We need to understand better when specific data post-processing techniques are valuable to understanding the science and when they can mask features. While software like OCLIMAX exists for calculating multiphonon and multiple scattering contributions for powder, we need to develop and streamline this capability for single crystals [33]. In the future, ideally, we will be able to run synthetic experiments by having three-dimensional scans of our samples.

We need faster ways to process single-crystal data in terms of computing. During this work, we collaborated with the NVIDIA RAPIDS team at NERSC to develop folding code that the RAPIDS team helped enable for GPU [34]. We sped up steps in the workflow by factor 191 compared to the CPU processing time in this process. GPUs will be a promising tool for speeding up experimental data processing.

5.4 The Future of Lattice Dynamics

Over the next several years, we will be able to measure and compute new types of AH effects. These effects include the previously discussed nonlinear quantum effects that stem from many-body theory and effects we have not imagined. In addition, through higher resolution measurements, machine learning codes, and GPU-based codes, we will be able to examine effects in materials that we have yet to imagine. I am excited to see what lies ahead.

References

[1] Z. Chen, N. Andrejevic, T. Smidt, Z. Ding, Q. Xu, Y.-T. Chi, Q. T. Nguyen, A. Alatas, J. Kong, and M. Li, en, Adv. Sci. (Weinh.) **8**, e2004214 (2021).

[2] G. E. Granroth, K. An, H. L. Smith, P. Whitfield, J. C. Neuefeind, J. Lee, W. Zhou, V. N. Sedov, P. F. Peterson, A. Parizzi, H. Skorpenske, S. M. Hartman, A. Huq, and D. L. Abernathy, J. Appl. Crystallogr. **51**, 616 (2018).

[3] P. F. Peterson, S. I. Campbell, M. A. Reuter, R. J. Taylor, and J. Zikovsky, Nuclear Instruments and Methods in Physics Research Section A: Accelerators, Spectrometers, Detectors and Associated Equipment **803**, 24 (2015).

[4] K. Page, B. Haberl, L. Coates, and M. Tucker, Rev. Sci. Instrum. **89**, 092601 (2018).

[5] M. J. Cooper and R. Nathans, Acta Crystallogr. **23**, 357 (1967).

[6] S. A. Werner and R. Pynn, J. Appl. Phys. **42**, 4736 (1971).

[7] N. J. Chesser and J. D. Axe, Acta Crystallogr. A **29**, 160 (1973).

[8] G. Xu, P. M. Gehring, V. J. Ghosh, and G. Shirane, Acta Crystallogr. A **60**, 598 (2004).

[9] T. Tadano and S. Tsuneyuki, Phys. Rev. B **92**, 054301 (2015).

[10] Y. Oba, T. Tadano, R. Akashi, and S. Tsuneyuki, Phys. Rev. Mater. **3**, 033601 (2019).

[11] T. Tadano, Y. Gohda, and S. Tsuneyuki, J. Phys. Condens. Matter **26**, 225402 (2014).

[12] O. Hellman, I. A. Abrikosov, and S. I. Simak, Phys. Rev. B **84**, 180301 (2011).

[13] O. Hellman, P. Steneteg, I. A. Abrikosov, and S. I. Simak, Phys. Rev. B **87**, 104111 (2013).

[14] O. Hellman and I. A. Abrikosov, Phys. Rev. B **88**, 144301 (2013).

[15] F. Zhou, W. Nielson, Y. Xia, and V. Ozoli , Phys. Rev. Lett. **113**, 185501 (2014).

[16] F. Zhou, W. Nielson, Y. Xia, and V. Ozoli , Phys. Rev. B **100**, 184308 (2019).

[17] F. Zhou, B. Sadigh, D. Åberg, Y. Xia, and V. Ozoli , Phys. Rev. B **100**, 184309 (2019).

[18] F. Eriksson, E. Fransson, and P. Erhart, en, Adv. Theory Simul. **2**, 1800184 (2019).

[19] A. Togo, L. Chaput, and I. Tanaka, Phys. Rev. B **91**, 094306 (2015).

[20] W. Li, J. Carrete, N. A. Katcho, and N. Mingo, Comp. Phys. Commun. **185**, 1747 (2014).

[21] A. Shapeev, Multiscale Model. Simul. **14**, 1153 (2016).

[22] O. T. Unke, S. Chmiela, H. E. Sauceda, M. Gastegger, I. Poltavsky, K. T. Schütt, A. Tkatchenko, and K.-R. Müller, Chem. Rev. **121**, 10142 (2021).

[23] F. Knoop, T. A. R. Purcell, M. Scheffler, and C. Carbogno, Phys. Rev. Mater. **4**, 083809 (2020).

[24] F. Knoop, T. A. R. Purcell, M. Scheffler, and C. Carbogno, Phys. Rev. Mater. **4**, 083809 (2020).

[25] D. S. Kim, O. Hellman, J. Herriman, H. L. Smith, J. Y. Y. Lin, N. Shulumba, J. L. Niedziela, C. W. Li, D. L. Abernathy, and B. Fultz, Proc. Natl. Acad. Sci. U. S. A. **115**, 1992 (2018).

[26] A. Glensk, B. Grabowski, T. Hickel, J. Neugebauer, J. Neuhaus, K. Hradil, W. Petry, and M. Leitner, Phys. Rev. Lett. **123**, 235501 (2019).

[27] X. Tang, C. W. Li, and B. Fultz, Phys. Rev. B **82**, 184301 (2010).

[28] L. Pintschovius, F. Weber, W. Reichardt, A. Kreyssig, R. Heid, D. Reznik, O. Stockert, and K. Hradil, Pramana **71**, 687 (2008).

[29] B. Wei, X. Yu, C. Yang, X. Rao, X. Wang, S. Chi, X. Sun, and J. Hong, Phys. Rev. B **99**, 184301 (2019).

[30] R. Youngblood, Y. Noda, and G. Shirane, Phys. Rev. B **19**, 6016 (1979).

[31] J. W. L. Pang, A. Chernatynskiy, B. C. Larson, W. J. L. Buyers, D. L. Abernathy, K. J. McClellan, and S. R. Phillpot, Phys. Rev. B **89**, 115132 (2014).

[32] D. S. Kim, O. Hellman, N. Shulumba, C. N. Saunders, J. Y. Y. Lin, H. L. Smith, J. E. Herriman, J. L. Niedziela, D. L. Abernathy, C. W. Li, and B. Fultz, Phys. Rev. B **102**, 174311 (2020).

[33] Y. Q. Cheng, L. L. Daemen, A. I. Kolesnikov, and A. J. Ramirez-Cuesta, J. Chem. Theory Comput **15**, PMID: 30735379, 1974 (2019).

[34] R. Becker, B. Nick, and L. Stephen, *Rapids makes gpus more accessible for python users at the national energy research scientific computing center*, May 2020.

Appendix A

THERMAL STABILITY OF CUPRITE

There are reports in the literature that cuprite dissociates at elevated temperatures [1]. We annealed powdered samples of cuprite for one hour in a vacuum at 300 K, 773 K, 973 K, 1173 K and measured post-annealing diffraction patterns at room temperature to test this claim. Figure A.1 shows insignificant changes to the samples after heating. This result is consistent with the synthesis of our cuprite single crystal by the float zone growth method, which exposed the crystal to high temperatures to remove cupric oxide (CuO) and suppress void formation [2].

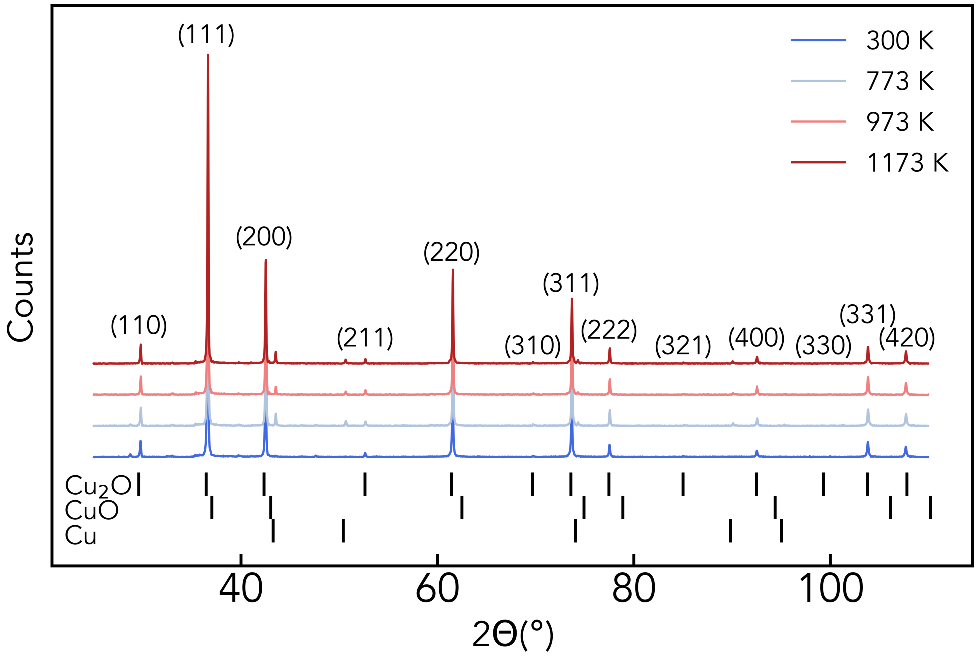

Figure A.1: Post-annealing X-ray diffraction patterns measured at 300 K, 773 K, 972 K, and 1173 K. Peaks are indexed. Black markers under the diffraction patterns are positions of diffraction peaks from Cu, CuO, and Cu_2O.

References

[1] A. Sanson, F. Rocca, G. Dalba, P. Fornasini, R. Grisenti, M. Dapiaggi, and G. Artioli, Phys. Rev. B **73**, 214305 (2006).

[2] S. T. Omelchenko, Y. Tolstova, S. S. Wilson, H. A. Atwater, and N. S. Lewis, in 2015 ieee 42nd photovoltaic specialist conference (pvsc) (2015), pp. 1–4.

Appendix B

SINGLE CRYSTAL SAMPLE SETUP

For 10 K inelastic neutron scattering measurements, the single crystal was suspended with a niobium and platinum mount (Fig. B.1). Only platinum was in contact with the cuprite crystal. The platinum and niobium were not directly in the neutron beam. The crystal was similarly mounted for 300 K measurements but contained in a thin aluminum canister. Background measurements were obtained from the aluminum canister. Aluminum has distinct phonon features around 20 and 30 meV [1]. However, scattering from the thin aluminum was less than 2% of the cuprite sample, which dominated the inelastic intensity at 20-30 meV [2]. The background was found to be negligible and was not subtracted from the data. We determined the experimental lattice parameter using white-beam measurements of the total scattering.

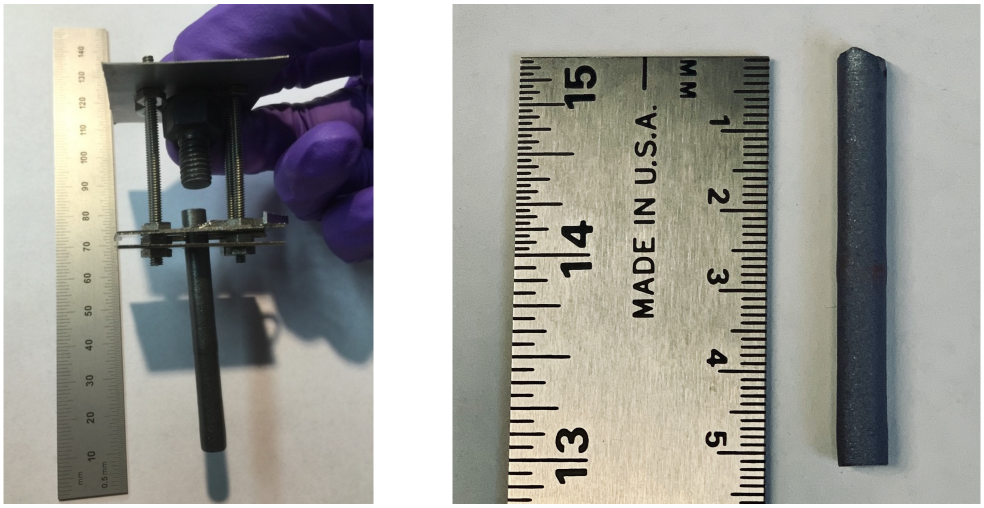

Figure B.1: The left-hand image shows the single crystal with platinum and niobium mount used for measurement. The right hand image data measurements shows the same single crystal after the experiment removed from the mount.

References

[1] M. Kresch, M. Lucas, O. Delaire, J. Y. Y. Lin, and B. Fultz, Phys. Rev. B **77**, 024301 (2008).

[2] V. F. Sears, Neutron News **3**, 26 (1992).

Appendix C

DETAILS ON THERMAL EXPANSION CALCULATIONS

Considerable effort has gone into determining the optimal exchange-correlation functional for both electronic structure calculations and lattice dynamics calculations in cuprite. We calculated and compared equilibrium lattice constants for LDA, PBE, PBE0, SCAN metaGGA, AM05, HSE06 with an experimental value (Table C.1). We found that AM05, PBE0, SCAN metaGGA, and HSE06 all yielded reasonable results for lattice constants. HSE06 and SCAN metaGGA gave similar electronic band gaps. A clear relationship was seen between the accuracy of the equilibrium lattice constants and the position of the optical modes. Due to the computational cost of HSE06 we were not able to use it for large supercell calculations.

For sTDEP calculations, 20 canonical configurations were generated for each of the five volumes. Zero-point energy was enabled. When calculating force constants, the cutoff radius for second-order force constants was 100.0 Å, and the cutoff for third-order force constants was 50.0 Å. For phonon dispersion calculations, the q-point mesh was 26x26x26, and the integration method was the standard Monkhorst-Pack mesh. Default values were used for calculating the phonon self-energy. In the PHONOPY calculations, the sampling mesh was 8x8x8.

Previous studies performed convergence testing on supercell size and the number of k-points [3]. Our results agree with previous convergence testing for QH and

Functional	a_0 (Å)
LDA	4.1814[a]
PBE	4.1323[a]
PBE0	4.2851[a]
SCAN	4.2580
AM05	4.2395
HSE06	4.2887[a]
Experiment	4.2696[b]

Table C.1: This table compares the equilibrium lattice constant, a_0, and electronic bandgap, for various exchange correlations and experiment.
[a] Reference [1]
[b] Reference [2]

AH calculations. We considered the effect of supercell size and the number of k-points on the phonon dispersions and lineshapes for our convergence testing. We performed *ab initio* calculations on displaced configurations of atoms and calculated the corresponding free energy.

Using the finite displacement method in PHONOPY, we calculated phonon frequencies for five volumes [4]. Using the Stochastic Temperature Dependent Effective Potential Method (sTDEP) package, we calculated phonon dispersions at finite temperatures by fitting first-principles forces on atoms in the supercell to the following model Hamiltonian [5]:

$$H = U_0 + \sum_i \frac{\mathbf{p}_i^2}{2m} + \frac{1}{2} \sum_{ij\alpha\beta} \Phi_{ij}^{\alpha\beta} u_i^\alpha u_j^\beta \tag{C.1}$$

where i, j denotes an atom and α, β are Cartesian coordinates.

To simulate effects of higher temperature, we generated various configurations of atoms by stochastic sampling of a canonical ensemble, with Cartesian displacements, u_i^α, normally distributed around a mean thermal displacement [6]:

$$u_i^\alpha = \sum_s \frac{\epsilon_s^{i\alpha} c_{s,\alpha}}{\sqrt{m_i}} \sqrt{-2\ln \xi_1} \sin(2\pi\xi_2). \tag{C.2}$$

Here c_α is the amplitude for a normal mode s, ϵ_s, ω_s are the normal mode eigenvector and frequency respectively, and ξ_1 and ξ_1 are random numbers between 0 and 1.

$$c_{s,\alpha} = \sqrt{\frac{\hbar(2n_s + 1)}{2m_s\omega_s}} \tag{C.3}$$

This amplitude in Eq.C.3 accounts for nuclear quantum effects through zero point amplitude. We used this for our AH calculations. To obtain phonon dispersions, we used the model Hamiltonian:

$$H = U_0 + \sum_i \frac{\mathbf{p}_i^2}{2m} + \frac{1}{2} \sum_{ij\alpha\beta} \Phi_{ij}^{\alpha\beta} u_i^\alpha u_j^\beta + \frac{1}{3!} \sum_{ijk\alpha\beta\gamma} \Phi_{ijk}^{\alpha\beta\gamma} u_i^\alpha u_j^\beta u_k^\gamma. \tag{C.4}$$

with the corresponding Helmholtz free energy in the main text. Here $U_0(T, V)$ depends on temperature and volume.

References

[1] L. Y. Isseroff and E. A. Carter, Phys. Rev. B **85**, 235142 (2012).

[2] A. Werner and H. D. Hochheimer, Phys. Rev. B **25**, 5929 (1982).

[3] J. Linnera, A. Erba, and A. J. Karttunen, J. Chem. Phys. **151**, 184109 (2019).

[4] A. Togo and I. Tanaka, Scr. Mater. **108**, 1 (2015).

[5] O. Hellman, P. Steneteg, I. A. Abrikosov, and S. I. Simak, Phys. Rev. B **87**, 104111 (2013).

[6] O. Hellman and I. A. Abrikosov, Phys. Rev. B **88**, 144301 (2013).

Appendix D

MULTIPHONON CORRECTION FOR POLYATOMIC SYSTEMS

The multiphonon correction for a crystal structure with multiple species can be approximated using existing derivations for the multiphonon scattering correction for a monatomic system within the incoherent approximation. We follow the conventions and derivation from V. Sears' 1973 paper on approximations for the incoherent neutron scattering function, $S(\mathbf{Q}, \varepsilon)$ [1]. In the equation for the multiphonon dynamical structure factor:

$$S(\mathbf{Q}, \varepsilon) = e^{-2W} \sum_{n=2}^{\infty} \frac{(2W)^n}{n!} \frac{\sigma}{M} A_n(\varepsilon), \tag{D.1}$$

$\mathbf{Q}$ is the reciprocal space vector; ε is the phonon energy; σ is the incoherent neutron scattering cross section; M is the atomic mass; and $2W$ is two times the Debye-Waller factor.

$$2W = 2W\left(|\mathbf{Q}|\right) = \frac{\hbar |\mathbf{Q}|^2}{2M} \int_0^{\infty} \frac{g(\varepsilon)}{\varepsilon} \coth\left(\frac{\varepsilon}{2k_B T}\right) \, d\varepsilon \; . \tag{D.2}$$

$A_n(\varepsilon)$ is defined as convolution of the thermally-weighted 1-phonon scattering profile with the thermally-weighted (n-1)-phonon scattering profile

$$A_n(\varepsilon) = A_1(\varepsilon) \circledast A_{n-1}(\varepsilon) = \int_0^{\infty} A_1(\varepsilon - E) A_{n-1}(\varepsilon) \, d\varepsilon \tag{D.3}$$

The 1^{st} order phonon spectrum, $A_1(\varepsilon)$, can be expressed as:

$$A_1(\varepsilon) = \frac{g(\varepsilon)}{\varepsilon} \frac{1}{e^{\varepsilon/k_B T} - 1}. \tag{D.4}$$

This can be broken down into two simple components. The first is the DOS, $g(\varepsilon)$, divided by the energy, ε. This term accounts for the fact that low-energy acoustic modes have larger amplitudes of motion than high-energy modes, and it allows us to properly weight the expression. The other term that appears in $A_1(\varepsilon)$ is the Planck occupancy factor modified for phonons.

$$n(\varepsilon, T) = \frac{1}{e^{-\frac{\varepsilon}{k_B T}} - 1} \tag{D.5}$$

This gives us the average number of phonons at a given energy value.

The DOS is a vital part of these calculations. Despite its importance, there is no standard for what type of phonon DOS to use to minimize introducing error into our data post-processing. The following options exist for obtaining a phonon DOS for the above equations: (1) calculated total, (2) calculated partial, (3) measured total, and (4) measured partial. Each option has pros and cons associated with it, and the reader should use the option best suited for their specific situation.

In the case of a monatomic system where (1) calculated total DOS and (3) measured total are relevant, one must consider that the peaks of the calculated will be significantly sharper than what can be measured experimentally. This peak sharpness can result in an undersubtration of the multiphonon contributions. In this scenario, an instrument resolution function can be convoluted with the calculated DOS to make it more reflective of what is seen in experiment [2].

Conversely, using an experimental DOS risks oversubtracting the multiphonon contribution. To understand this, we must first understand how we obtain the experimental DOS. The most common way is to perform INS on a powder or polycrystalline sample. Once the data is collected, it needs to be reduced. This reduction involves calculating and subtracting a multiphonon contribution. This process is typically done in an iterative fashion until a convergence criteria is achieved [3]. Some multiphonon contribution may remain in the experimental DOS. This leftover contribution will affect the scaling factor in Eq. D.4.

Another option for obtaining a phonon DOS from experiment is calculating the DOS in each Brillouin zone in our single crystal data. This options is more complicated than measuring the DOS directly from a sample. To understand how to perform this calculation with single crystal data, we turn to the definition of the phonon DOS. We know that it is the number of modes per unit frequency or energy in a unit volume of space. To successfully calculate the DOS for each Brillouin zone (BZ), we need complete data coverage in each zone or a concrete understanding of the partial volume of the data within the boundaries of the expected zone. In single crystal experiments, parts of BZ are often missing due to lack of full detector coverage and size and shape of the sample. However, the advantage to this approach is that we would be considering the number of modes specific to each zone. This approach results in similar error to using the experimentally measured DOS since we would like have remaining components of the multiphonon contribution to the DOS in this weighting factor.

In the example calculation shown in this appendix, we show the multiphonon

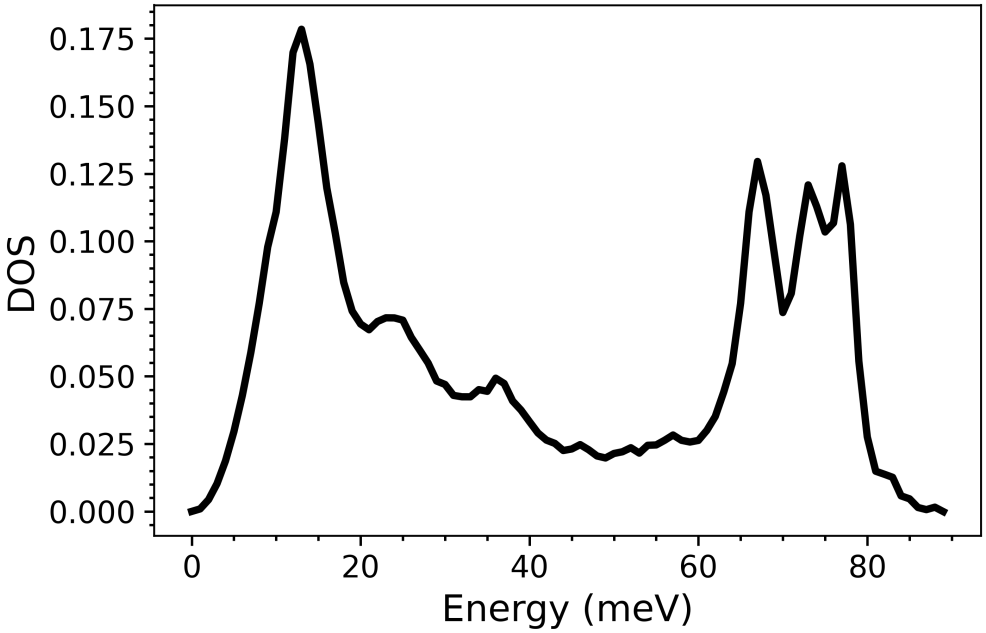

Figure D.1: This figure shows the experimental density of states for cuprite at 5 K

dynamical structure factor results for 700 K in Fig.D.2 using an experimentally obtained DOS from powder measurements shown in Fig.D.1).

When the system we are working with has multiple atom species, it is necessary to consider how to treat the interactions between different atom species along with self-interactions. In previous publications it has been treated as a function of all the possible correlations of different atom species [4]. In this setup for a system with two atom species, we define $A_1(\varepsilon)$ as

$$\begin{aligned} A_{1,\alpha}(\varepsilon) &= \frac{g_\alpha(\varepsilon)}{\varepsilon}\frac{1}{e^{\varepsilon/k_BT}-1} \\ A_{1,\beta}(\varepsilon) &= \frac{g_\beta(\varepsilon)}{\varepsilon}\frac{1}{e^{\varepsilon/k_BT}-1} \end{aligned} \tag{D.6}$$

where α and β specify the atom species type, $g_\alpha(\varepsilon)$ is the partial density of state for species α, and $g_\beta(\varepsilon)$ is the partial density of state for species β. $A_{n,\alpha/\beta}$ written as a sum of all correlation

$$\begin{aligned} A_{n,\alpha} &= A_{1,\alpha} \circledast A_{n-1,\alpha} + \frac{1}{n}A_{1,\alpha} \circledast A_{n-1,\beta} + \frac{n-1}{n}A_{1,\beta} \circledast A_{n-1,\alpha} \\ A_{n,\beta} &= A_{1,\beta} \circledast A_{n-1,\beta} + \frac{1}{n}A_{1,\beta} \circledast A_{n-1,\alpha} + \frac{n-1}{n}A_{1,\alpha} \circledast A_{n-1,\beta} \end{aligned} \tag{D.7}$$

For proof of concept, let's look at a simplified case of these equations where α

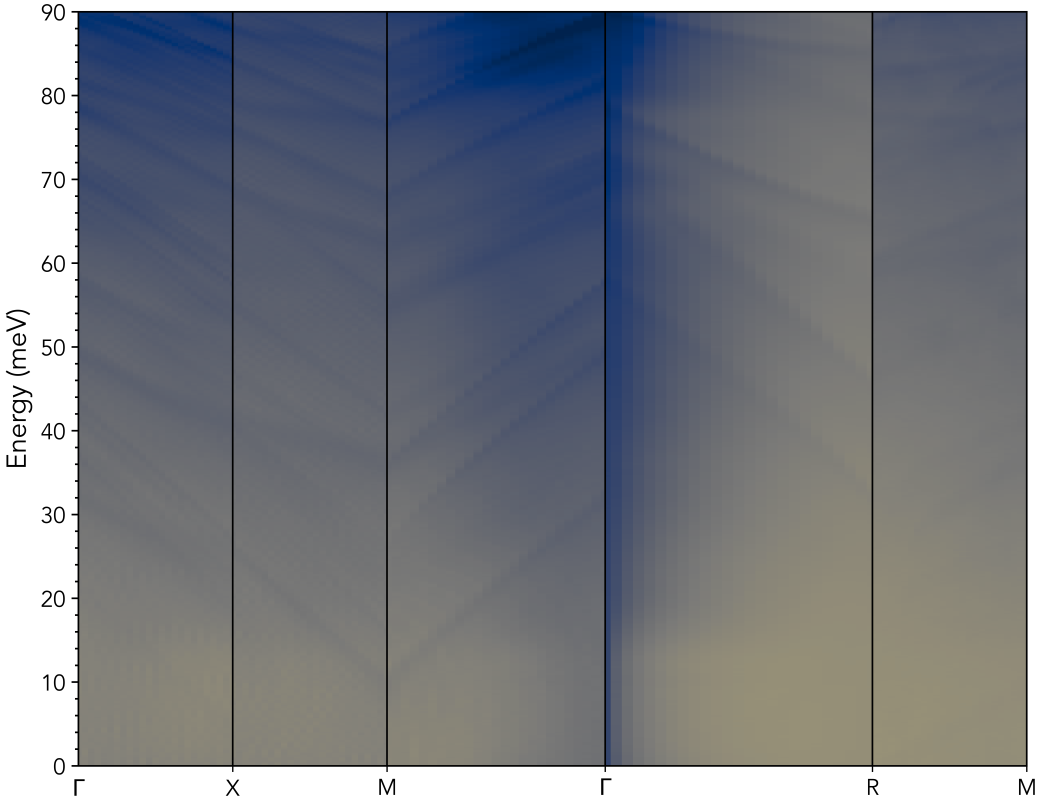

Figure D.2: This shows the weighted, thermal factor corrected multiphonon approximation for 700 K along the folded high-symmetry path in cuprite. The experimental density of state for 5 K was used for this calculation. The streaking seen throughout originates from weighting the multiphonon contribution with the number of neutron events recorded.

and β are the same, designated by γ, and $g_\alpha + g_\beta = g_\gamma$ such that $g_\alpha = g_\beta = \frac{1}{2} g_\gamma$

$$\begin{aligned}
A_{n,\alpha} &= \frac{g_\alpha(\varepsilon)}{\varepsilon} \frac{1}{e^{\varepsilon/k_B T} - 1} \circledast A_{n-1,\alpha} \\
&\quad + \frac{1}{n} \frac{g_\alpha(\varepsilon)}{\varepsilon} \frac{1}{e^{\varepsilon/k_B T} - 1} \circledast A_{n-1,\beta} + \frac{n-1}{n} \frac{g_\beta(\varepsilon)}{\varepsilon} \frac{1}{e^{\varepsilon/k_B T} - 1} \circledast A_{n-1,\alpha} \\
A_{n,\beta} &= \frac{g_\beta(\varepsilon)}{\varepsilon} \frac{1}{e^{\varepsilon/k_B T} - 1} \circledast A_{n-1,\beta} \\
&\quad + \frac{1}{n} \frac{g_\beta(\varepsilon)}{\varepsilon} \frac{1}{e^{\varepsilon/k_B T} - 1} \circledast A_{n-1,\alpha} + \frac{n-1}{n} \frac{g_\alpha(\varepsilon)}{\varepsilon} \frac{1}{e^{\varepsilon/k_B T} - 1} \circledast A_{n-1,\beta}
\end{aligned}$$

Combining like terms

$$\begin{aligned}
A_{n,\alpha} &= \left(\frac{1}{e^{\varepsilon/k_BT}-1}\right)\left(\frac{1}{\varepsilon}\right)\Big[g_\alpha(\varepsilon)\circledast A_{n-1,\alpha} \\
&\quad + \frac{1}{n}g_\alpha(\varepsilon)\circledast A_{n-1,\beta} + \frac{n-1}{n}g_\beta(\varepsilon)\circledast A_{n-1,\alpha}\Big] \\
A_{n,\beta} &= \left(\frac{1}{e^{\varepsilon/k_BT}-1}\right)\left(\frac{1}{\varepsilon}\right)\Big[g_\beta(\varepsilon)\circledast A_{n-1,\beta} \\
&\quad + \frac{1}{n}g_\beta(\varepsilon)\circledast A_{n-1,\alpha} + \frac{n-1}{n}g_\alpha(\varepsilon)\circledast A_{n-1,\beta}\Big]
\end{aligned}$$

Now we add $A_{n-1,\alpha} + A_{n-1,\beta}$

$$\begin{aligned}
A_{n,\alpha} + A_{n,\beta} &= \left(\frac{1}{e^{\varepsilon/k_BT}-1}\right)\left(\frac{1}{\varepsilon}\right)\left[\left(g_\alpha(\varepsilon) + \frac{n-1}{n}g_\beta(\varepsilon) + \frac{1}{n}g_\beta(\varepsilon)\right)\circledast A_{n-1,\alpha}\right. \\
&\quad \left. + \left(\frac{1}{n}g_\alpha(\varepsilon) + g_\beta(\varepsilon) + \frac{n-1}{n}g_\alpha(\varepsilon)\right)\circledast A_{n-1,\beta}\right]
\end{aligned} \tag{D.8}$$

Substituting $g_\alpha(\varepsilon) = g_\beta(\varepsilon) = \frac{1}{2}g_\gamma(\varepsilon)$

$$\begin{aligned}
A_{n,\alpha} + A_{n,\beta} &= \left(\frac{1}{e^{\varepsilon/k_BT}-1}\right)\left(\frac{1}{2\varepsilon}\right)\left[\left(1 + \frac{n-1}{n} + \frac{1}{n}\right)g_\gamma(\varepsilon)\circledast A_{n-1,\alpha}\right. \\
&\quad \left. + \left(\frac{1}{n} + 1 + \frac{n-1}{n}\right)g_\gamma(\varepsilon)\circledast A_{n-1,\beta}\right]
\end{aligned} \tag{D.9}$$

Substituting $A_{n,\alpha} + A_{n,\beta} = A_{n,\gamma}$,

$$A_{n,\alpha} + A_{n,\beta} = \left(\frac{1}{e^{\varepsilon/k_BT}-1}\right)\left(\frac{g_\gamma(\varepsilon)}{\varepsilon}\right)\circledast\left(A_{n-1,\alpha} + A_{n-1,\beta}\right) \tag{D.10}$$

This gives us the final expression

$$A_{n,\gamma} = \left(\frac{1}{e^{\varepsilon/k_BT}-1}\right)\left(\frac{g_\gamma(\varepsilon)}{\varepsilon}\right)\circledast A_{n-1,\gamma} \tag{D.11}$$

There is no ideal practice here for the multiphonon correction of single crystal datasets. Ideally, we want to keep our computational and experimental errors separate. However, we also want to avoid adding error by subtracting a multiphonon component that includes an unaccounted for multiphonon contribution from another experimental dataset. This appendix explains the calculation and subtraction of the multiphonon correction for the cuprite single crystal dataset and discusses options that the reader can implement in their own experimental single crystal data reduction.

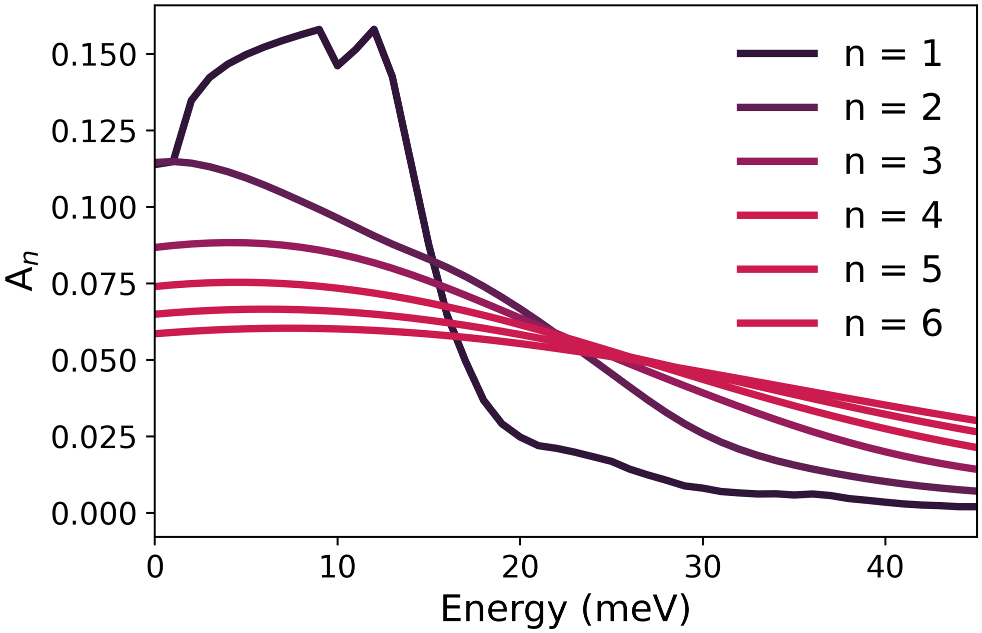

Figure D.3: This figure shows the form of A$_n$ for cuprite for n = 1 through 6.

For the low temperature data (10 K and 300 K), an experimental phonon density of state from powder measurements was used rather than calculated. This was done with the knowledge that the multiphonon contributions would be relatively small at these temperatures. Conveniently, we happened to have experimental data from powder cuprite at 5 K and 300 K.

Forms of A$_n(\varepsilon)$ for n = 0 to 6 are shown in Fig. D.3. The elastic peak which was approximated with a skewed Lorenztian function. The elastic peak was then subtracted and subsequent convolutions were performed to recursively obtain the remaining values of A$_n(\varepsilon)$.

For Cu_2O, a polyatomic system, we used averaged versions of these equations. This also reflects our decision to use the DOS from a powder sample. For Eq. **??**, we replace σ and M with:

$$\sigma_{av} = \frac{2}{3}\sigma_{Cu} + \frac{1}{3}\sigma_O \ , \tag{D.12}$$

$$M_{av} = \frac{2}{3}M_{Cu} + \frac{1}{3}M_O \ . \tag{D.13}$$

Fractions in front of the partial contributions are the partial molar fractions. The final result is a multiphonon $S(\vec{Q},\varepsilon)$ that is averaged between Cu and O that we subtract from the experimental $S(\vec{Q},\varepsilon)$.

D.1 Code Excerpts

The following are snippets of the Python3 code with comments and pseudocode used to calculate the multiphonon correction.

The A_0 term is used to subtract the elastic peak from the density of state. There is an asymmetry in the ARCS resolution function that results in an elastic peak that more resembles a skewed Lorentzian rather than a Gaussian. To simplify the peak subtraction a Gaussian fit was used for these calculations.

```python
from scipy.signal import gaussian
def A0(e, g):
    e, g = reflected(e,g)
    return gaussian(len(e), std=0.5)
```

The expression for A_1 is described in Eq. D.4. Issues encountered when programming this component include divide-by-zero or not-a-number errors. These issues can be circumvented by suppressing the warning (shown in the code below) or replacing the zero or not-a-number with a sufficiently small number

```python
import numpy as np

def A1(e, g, T, de):
    beta = kbi/T
    g0 = gamma0(e, g, T, de)
    e, g = reflected(e,g)
    with np.errstate(invalid='ignore'):
        f = (g/e) / g0 / (1-np.exp(-e*beta))
        ind = np.argwhere(np.isnan(f))
        f[ind]=(f[ind-1]+f[ind+1])/2
        return f
```

The expression for A_n is described in Eq. D.3.

```python
from scipy.signal import convolve
import numpy as np

def An(e, g, T, de, n):
    if n == 0:
        A_val = A0(e, g)
    elif n == 1:
```

```
        A_val = A1(e, g, T, de)
        return A_val
    else:
        return convolve(A1(e, g, T, de),
        An(e, g, T, de, n-1),'same','direct')
        / np.sum(An(e, g, T, de, n-1))

import numpy as np
import math

def Sn(e, g, Q, T, M, de, n):
    WW = twoW(e, g, Q, M, T, de)
    WW = np.reshape(WW,(len(WW),1))
    A_res = An(e, g, T, de, n)[-len(e):]
    A = np.reshape(A_res,(1,len(A_res)))
    if n==1:
        return np.exp(-WW)*WW*M*A
    else:
        S = np.exp(-WW)*(WW**n/math.factorial(n))*M*A
        return S
```

References

[1] V. F. Sears, Phys. Rev. A **7**, 340 (1973).

[2] S. Diallo, J. Lin, D. Abernathy, and R. Azuah, J. Instrum. **835**, 34 (2016).

[3] J. Y. Y. Lin, F. Islam, and M. Kresh, J. Open Source Softw. **3**, 440 (2018).

[4] Y. Shen, C. N. Saunders, C. M. Bernal, D. L. Abernathy, M. E. Manley, and B. Fultz, Phys. Rev. Lett. **125**, 085504 (2020).

Appendix E

BEST PRACTICE FOR SINGLE CRYSTAL EXPERIMENTS

In the past ten years, instrumentation for scattering measurements has improved dramatically. Advancements in instrumentation allow for increasingly complicated sample environments that allow users to achieve higher temperatures, pressures, and vacuums than ever before. With these developments, we face new challenges in data management and post-processing. This is particularly important for single crystal measurements that generate larger data file (on the order of terabytes) than powder or polycrystalline measurements. Furthermore, there is no standard or "golden rule" for collecting event-based INS measurements for single crystals.

This text attempts to set forth general recommendations of best practice for the collection and analysis of INS single crystal data.

E.1 Sample Alignment

Proper sample alignment is a vital aspect of any scattering experiment. For samples that have a specific orientation, like single crystals, it is crucial for the success of an experiment. When mounting single crystals it is important to determine proper alignment through the UB matrix and u v vectors. The sample should be aligned at the beamline before data collection begins, and it should also be done when processing the data.

When using a chopper-spectrometer like ARCS where the Fermi choppers are mounted on a motorized translation table, the user should take white beam or polychromatic beam measurements when the crystal is mounted before data collection. White beam measurements allow the user to collect data on the structure of the single crystal sample along with the dynamics. By performing just two white beam measurements, the diffraction peaks from the white beam measurments an be used to

should be performed while the crystal is mounted before experimental data collection. For many of the post-processing codes to find the appropriate

E.2 Experimental Setup and Data Post-processing

The intensities at all $\vec{Q}$ were corrected for multiphonon scattering in the incoherent approximation, using a phonon DOS from cuprite powder and appropriate values of Q and T. The single crystal data were folded using symmetry operations to bring the inelastic intensity into a single irreducible wedge in the first Brillouin zone, followed by a correction for thermal occupancy. Folding brings risk if there are nonlinearities in the transformation of the measured intensities in k-space.

We verified that the higher-order Bragg diffraction occurred at the expected positions to validate the instrument linearity. In this analysis, we found slight offsets at high values of Q. This was done independently in Python. Autoreduced *.nxspe files were read in, converted to sample space [1] and the following selection factors were used for each data point:

1. The energy value of the point is within ± 3% of the incident energy. (This accounts for the elastic resolution of ARCS.)
2. The reciprocal space range is ± 0.1 reciprocal lattice units. (In fractional coordinates, we expect points to fall on integer values.)
3. The intensity of each point is less than or equal to 1.0. (This removes anomalous high-intensity points that reflect detector artifacts rather than elastic scattering.)

Examples of these diffractions and offsets are shown in Fig. E.1. After points were read in and converted, the centers of the intensities around reciprocal lattice points were determined by k-means clustering. Through multivariate regression, we obtained a linear correction matrix. This matrix should be close to the identity matrix. For the 10 K data, the correction matrix was:

$$\begin{pmatrix} 1.004 \times 10^{0} & -9.393 \times 10^{-4} & 8.176 \times 10^{-4} \\ 6.493 \times 10^{-4} & 0.9999 \times 10^{0} & 1.296 \times 10^{-4} \\ -1.378 \times 10^{-3} & 4.128 \times 10^{-4} & 1.000 \times 10^{0} \end{pmatrix}.$$

Offsets with increasing values of $\vec{Q}$ were within the instrument resolution. These offsets also informed our selection of the data limits to be folded. Results with linearly corrected data are shown in Fig. E.2. Ultimately, no linear corrections to the data were made because of their negligible magnitude relative to the instrument resolution and our inability to separate instrument and sample artifacts. We did observe $\vec{Q}$-dependent behavior, but we could not definitely say whether the trends were due to a mosaic structure of the single crystal, misalignment in the sample mount on the instrument, misalignment of our crystal, or accuracy of the instrument resolution function. Furthermore, the elastic and inelastic data require different corrections in k-space.

Folding was done in Mantid [2]. Thermal weighting of the data was done to correct spectral weights, using the functional form:

$$\frac{-\varepsilon}{e^{\frac{-\varepsilon}{k_B T}} - 1} \times S(\vec{Q}, \varepsilon) = S_{\text{weighted}}(\vec{Q}, \varepsilon) \tag{E.1}$$

where $\varepsilon = \hbar\omega$. For visualization, spectral intensities were corrected for thermal weights after folding. This correction increased intensity in high-energy optical modes.

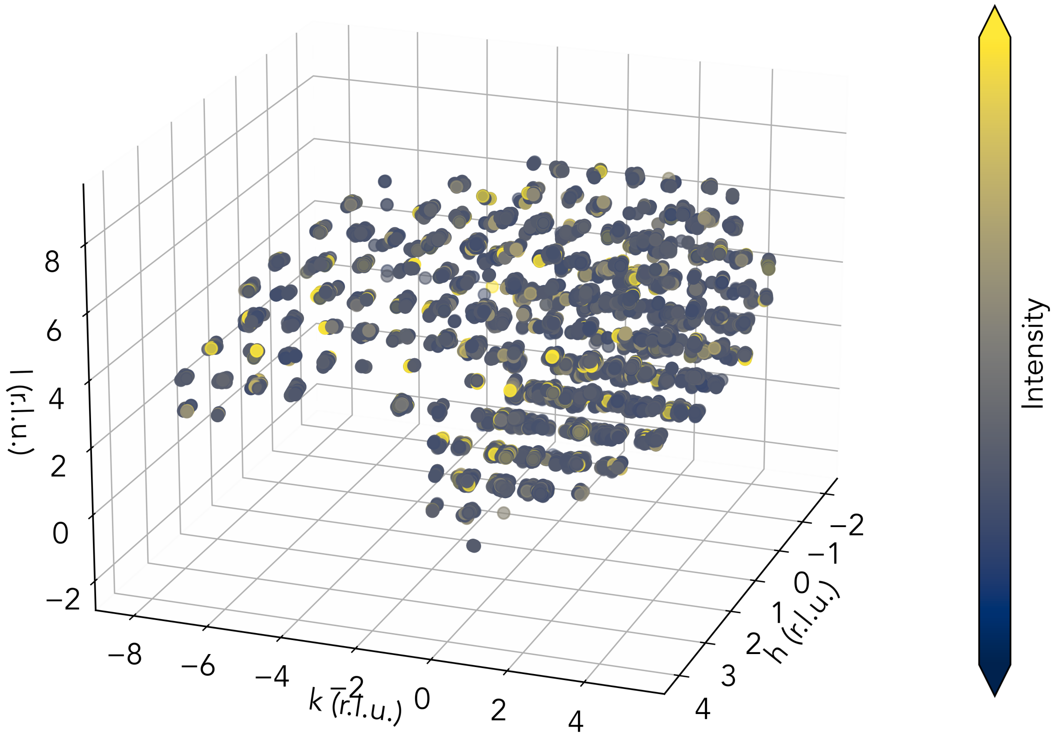

Figure E.1: Diffraction pattern from 10 K data. These points were obtained by considering selection factors.

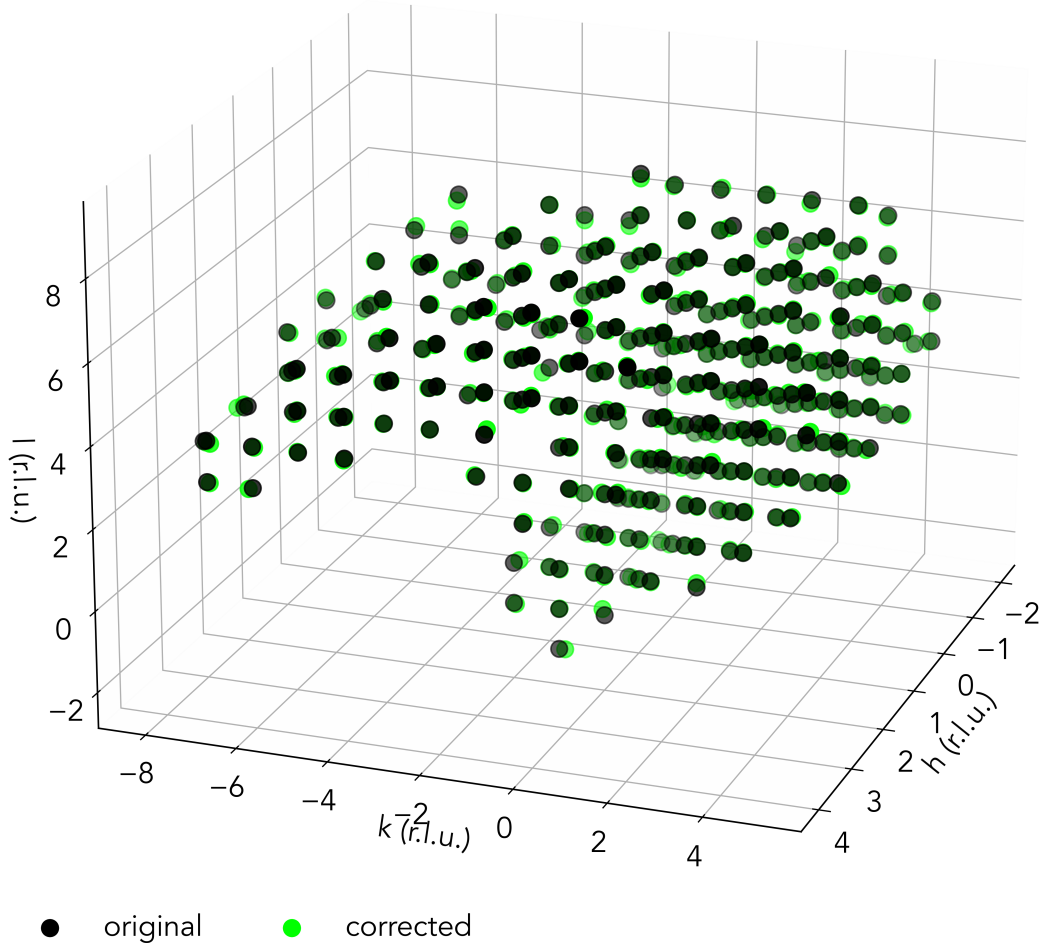

Figure E.2: Comparison of central point of diffraction points for 10 K data before (black) and after (green) matrix correction.

References

[1] M. D. Lumsden, J. L. Robertson, and M. Yethiraj, J. Appl. Crystallogr. **38**, 405 (2005).

[2] O. Arnold, J. Bilheux, J. Borreguero, A. Buts, S. Campbell, L. Chapon, M. Doucet, N. Draper, R. Ferraz Leal, M. Gigg, V. Lynch, A. Markvardsen, D. Mikkelson, R. Mikkelson, R. Miller, K. Palmen, P. Parker, G. Passos, T. Perring, P. Peterson, S. Ren, M. Reuter, A. Savici, J. Taylor, R. Taylor, R. Tolchenov, W. Zhou, and J. Zikovsky, Nucl. Instrum. Meth. A **764**, 156 (2014).

Appendix F

CALCULATING VELOCITY AUTO-CORRELATION FUNCTIONS

To properly calculate the vibrational dynamics from large MD simulations, one needs an efficient and accurate velocity auto-correlation analysis. Several packages exist to calculate the correlation function from MD trajectories including but not limited to pwtools, QuantumATK, and DYNASOR. For all velocity auto-correlation calculations mentioned, we used our own code VVCORE. VVCORE is a parallelized Central Processing Unit (CPU) and Graphics Processing Unit (GPU) enabled package that addresses the Input/Output bottleneck issues faced by other packages.

VVCORE calculates the mode-projected velocity

$$\mathbf{j}^{A}(\mathbf{q},t) = \sum_{i}^{N_A} \mathbf{v}_i(t) e^{i\mathbf{q}\mathbf{r}_i(t)} \tag{F.1}$$

which is a form of current density. In the above equation $\mathbf{q}$ is the wave-vector, $\mathbf{r}_i(t), \mathbf{v}_i(t)$ are the positions and velocities of individual atoms at time t, respectively. The index A denotes the partial contribution of type A to the total current, and N_A is the number of atoms of the corresponding type. $\mathbf{j}^{A}(\mathbf{q},t)$ can be broken down into the perpendicular and parallel wavevector components. The perpendicular or transverse element can be written as

$$\mathbf{j}_T^{A}(\mathbf{q},t) = \sum_{i}^{N_A} \left[\mathbf{v}_i(t) - \hat{\mathbf{q}}(\mathbf{v}_i(t)\cdot\hat{\mathbf{q}})\right] e^{i\mathbf{q}\mathbf{r}_i(t)} \tag{F.2}$$

and the parallel or longitudinal

$$\mathbf{j}_L^{A}(\mathbf{q},t) = \hat{\mathbf{q}} \sum_{i}^{N_A} (\mathbf{v}_i(t)\cdot\hat{\mathbf{q}}) e^{i\mathbf{q}\mathbf{r}_i(t)} \tag{F.3}$$

. To get the transverse and longitudinal DOSs at a specific point in the BZ, we take the Fourier transforms of Eqs. F.2 and F.2

$$g_k^{AB}(\omega,\mathbf{q}) = \int_0^\infty \left\langle \mathbf{j}_k^{A}(t,\mathbf{q})\mathbf{j}_k^{B}(0,-\mathbf{q}) \right\rangle e^{-i\omega t} dt, \tag{F.4}$$

where the subscript k denotes the point of interest along the transverse or longitudinal direction. To obtain the total density at a wavevector $\mathbf{q}$, we add the individual DOSs and weight them with their masses.

$$g(\omega, \mathbf{q}) = \sum_{A,B} \sqrt{M_A M_B} \left(g_T^{AB} + g_L^{AB} \right) \tag{F.5}$$

After the summation, we can obtain the vibrational density of states by taking the Fourier transform

$$\Phi(t) = \frac{1}{N} \sum_{i}^{N} \frac{\left\langle \mathbf{v}_i(t)\mathbf{v}_i(0) \right\rangle}{\left\langle \mathbf{v}_i(0)\mathbf{v}_i(0) \right\rangle}, \tag{F.6}$$

which can be used to obtain a phonon density of state

$$g(\omega) = \int_0^\infty \Phi(t) \cos(\omega t) dt. \tag{F.7}$$

To get the dynamical structure factor, one needs to relate the longitudinal correlations:

$$\omega^2 S(\mathbf{Q}, E) = q^2 \tag{F.8}$$